Chapter 4

The Diffusion Tensor

The primary aims of this chapter are to introduce, motivate, and characterize the mean free path expressions employed in the present study, as well as the approach followed in modeling the effects of turbulence on cosmic-ray drifts. As such, it shall commence with a brief discussion as to how the diffusion tensor fits into the broader picture of cosmic-ray modulation studies, from the perspective of the Parker transport equation. Observations and numerical simulations of mean free paths will be considered to motivate the choices of scattering theories here employed in the derivation of suitable mean free path expressions. The parallel mean free paths so derived will then be discussed in detail, and characterized using as inputs the results yielded by the two-component turbulence transport model of *Oughton et al.* [2011] discussed in the previous chapter. The onset of the dissipation range will be modelled using the results of *Leamon et al.* [2000].

Subsequently, the perpendicular diffusion and drift coefficients will be introduced and motivated. Perpendicular mean free paths are here derived from the enhanced nonlinear guiding center theory (ENLGC) of *Shalchi* [2006], and characterized as functions of rigidity and heliocentric spatial coordinates throughout the heliosphere for various assumed values and spatial dependences of the 2D outerscale. As this is a quantity for which currently no observations exist, it needs to be modelled in an *ad hoc* manner. Inputs for the various turbulence quantities these mean free paths depend upon follow from the *Oughton et al.* [2011] two-component turbulence transport model.

The results of numerical simulations concerning the reduction of drifts due to the action of turbulence will be discussed, as will be the models for wavy current sheet drift and for the turbulence-reduced drift coefficient. This drift coefficient, and the 2D ultrascale of which it is a function, will also be characterized using as inputs the results of the abovementioned turbulence transport model, again assuming various *ad hoc* values and spatial dependences for the 2D outerscale. This chapter, then, will serve to introduce an *ab initio* diffusion tensor, combining one of the latest models for the transport of turbulence throughout the heliosphere with mean free path expressions derived from particle scattering theories. It will conclude with a summary of the presented results.

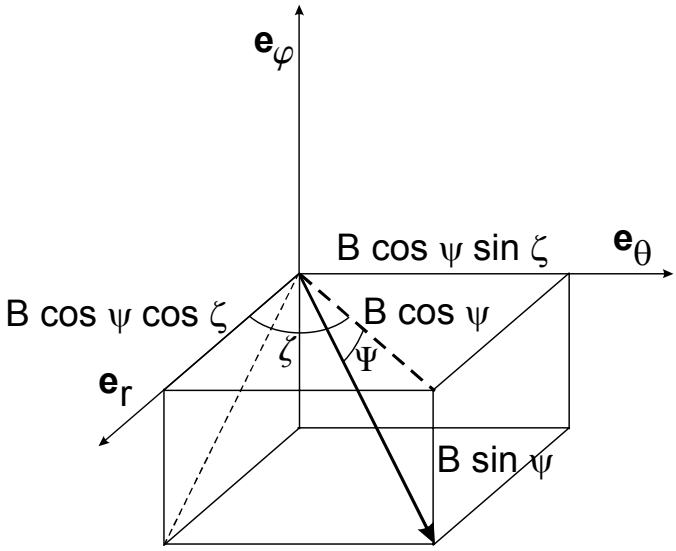

Figure 4.1: Components of the magnetic field in terms of ψ and ζ [*Burger et al.*, 2008].

4.1 Introduction

The effects of diffusion, and of drifts due to gradients and curvatures in the heliospheric magnetic field on the modulation of cosmic-rays, as well as those of the adiabatic cooling and outward convection of cosmic-rays due to the action of the solar wind, are all ensconced in the *Parker* [1965a] cosmic-ray transport equation discussed in the next chapter. The diffusion tensor **K** that appears in that equation can be written in spherical coordinates as

$$\mathbf{K} = \begin{bmatrix} \kappa_{rr} & \kappa_{r\theta} & \kappa_{r\phi} \\ \kappa_{\theta r} & \kappa_{\theta\theta} & \kappa_{\theta\phi} \\ \kappa_{\phi r} & \kappa_{\phi\theta} & \kappa_{\phi\phi} \end{bmatrix} \tag{4.1}$$

whereas in a field-aligned coordinate system the diffusion tensor becomes

$$\mathbf{K}' = \begin{bmatrix} \kappa_{\parallel} & 0 & 0 \\ 0 & \kappa_{\perp,2} & \kappa_A \\ 0 & -\kappa_A & \kappa_{\perp,3} \end{bmatrix}. \tag{4.2}$$

Here $\kappa_{\perp,2}$ and $\kappa_{\perp,3}$ describe diffusion in directions perpendicular to the heliospheric magnetic field, $\kappa_{\parallel}$ describes diffusion parallel to the field, and the anisotropic terms κ_A denote the drift coefficient. The coefficients in the field-aligned tensor can be related to those of the tensor in

heliocentric spherical coordinates by [*Burger et al.*, 2008]

$$\begin{aligned}
\kappa_{rr} &= (\kappa_{\parallel}\cos^2\psi + \kappa_{\perp,3}\sin^2\psi)\cos^2\zeta + \kappa_{\perp,2}\sin^2\zeta \\
\kappa_{r\theta} &= (\kappa_{\parallel}\cos^2\psi + \kappa_{\perp,3}\sin^2\psi - \kappa_{\perp,2})\sin\zeta\cos\zeta - \kappa_A\sin\psi \\
\kappa_{r\phi} &= (-\kappa_{\parallel} + \kappa_{\perp,3})\sin\psi\cos\psi\cos\zeta - \kappa_A\cos\psi\sin\zeta \\
\kappa_{\theta r} &= (\kappa_{\parallel}\cos^2\psi + \kappa_{\perp,3}\sin^2\psi - \kappa_{\perp,2})\sin\zeta\cos\zeta + \kappa_A\sin\psi \\
\kappa_{\theta\theta} &= (\kappa_{\parallel}\cos^2\psi + \kappa_{\perp,3}\sin^2\psi)\sin^2\zeta + \kappa_{\perp,2}\cos^2\zeta \\
\kappa_{\theta\phi} &= (-\kappa_{\parallel} + \kappa_{\perp,3})\sin\psi\cos\psi\sin\zeta + \kappa_A\cos\psi\cos\zeta \\
\kappa_{\phi r} &= (-\kappa_{\parallel} + \kappa_{\perp,3})\sin\psi\cos\psi\cos\zeta + \kappa_A\cos\psi\sin\zeta \\
\kappa_{\phi\theta} &= (-\kappa_{\parallel} + \kappa_{\perp,3})\sin\psi\cos\psi\sin\zeta - \kappa_A\cos\psi\cos\zeta \\
\kappa_{\phi\phi} &= \kappa_{\parallel}\sin^2\psi + \kappa_{\perp,3}\cos^2\psi
\end{aligned} \tag{4.3}$$

with angles ψ and ζ, from Fig. 4.1, defined as

$$\begin{aligned}
\sin\psi &= -\frac{B_\phi}{B};\ \cos\psi = \frac{\sqrt{B_r^2 + B_\theta^2}}{B} \\
\sin\zeta &= \frac{B_\theta}{\sqrt{B_r^2 + B_\theta^2}};\ \cos\zeta = \frac{B_r}{\sqrt{B_r^2 + B_\theta^2}},
\end{aligned} \tag{4.4}$$

which implies that

$$\tan\psi = -\frac{B_\phi}{\sqrt{B_r^2 + B_\theta^2}}. \tag{4.5}$$

Note that the above transformation assumes a heliospheric magnetic field model with a finite meridional component. Should a Parker field be employed, with its zero meridional component, Equations 4.3 and 4.5 will reduce to the results of *Alania and Dzhapiashvili* [1979], *Kobylinski* [2001] and *Alania* [2002]. A generalized expression for the diffusion tensor, also applicable when non-axisymmetric perpendicular diffusion is assumed (see *Weinhorst et al.* [2008]), can be found in *Effenberger et al.* [2012].

The diffusion coefficients to be found in Eq. 4.2 can be written in terms of mean free paths parallel and perpendicular to the mean HMF, such that

$$\begin{aligned}
\kappa_{\parallel} &= \frac{v}{3}\lambda_{\parallel}, \\
\kappa_{\perp} &= \frac{v}{3}\lambda_{\perp},
\end{aligned} \tag{4.6}$$

with v the particle speed.

4.2 Mean free paths: observations and simulations

This section aims to discuss the various observations and simulations for both the parallel and perpendicular mean free paths currently extant in the literature, in part to motivate the choices of scattering theories from which the mean free paths used in this study are derived, and to ascertain whether these modelled mean free paths are indeed realistic. Many different scattering theories are mentioned in this section, but not all are discussed in detail. Such discussions can, however, be found in *Shalchi* [2009] and *Dosch et al.* [2009], and in the references cited below.

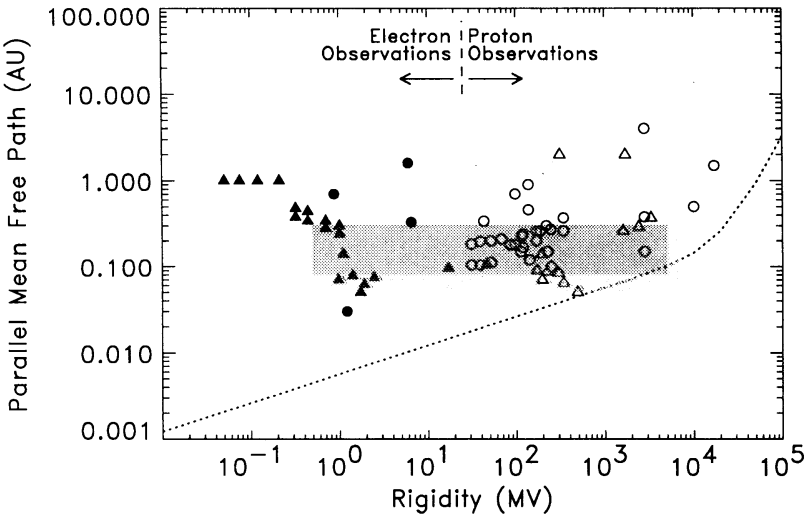

Figure 4.2: *Palmer* [1982] consensus range (shaded box) for the cosmic-ray parallel mean free path, and various observed values, from *Bieber et al.* [1994]. Dotted line represents the parallel mean free path predicted by magnetostatic slab quasi-linear theory.

4.2.1 Observations

Mean free paths are not quantities that lend themselves readily to direct observation. Therefore reported observations of mean free paths are usually calculated from modelled fits to secondary phenomena such as observed solar energetic particle intensity profiles (*e.g. Dröge* [2000]), diurnal variations of particle intensities at Earth (*e.g. Bieber and Pomerantz* [1983]), or neutron monitor data (*e.g. Chen and Bieber* [1993]). Thus these mean free paths are actually calculated, but in what is to follow they will be treated as observations, in part to ensure no confusion when they are compared to results calculated from scattering theories.

Parallel mean free path

For many years, the consensus values reported by *Palmer* [1982] for the cosmic-ray mean free paths at Earth, illustrated in Fig. 4.2, have been the standard of comparison for the results yielded by any proposed cosmic-ray scattering theory. This consensus draws together the results acquired by *Bieber et al.* [1980], *Chenette* [1980], *Ford et al.* [1977], *Hamilton* [1977], *Lin* [1970], *Lin* [1974], *McCarthy and O'Gallagher* [1976], *Ma Sung and Earl* [1978], *Palmer et al.* [1975], *Palmer et al.* [1978], *Schulze et al.* [1977], *Zwickl and Webber* [1977], and *Zwickl and Webber* [1978] over the decades preceding its publication. These authors, by fitting intensity (and in some cases anisotropy) profiles observed for proton and electron energetic particle events through numerical simulations, report values for the diffusion coefficients that serve to best replicate observations. Note, however, that most studies that make use of solar energetic particles to calculate a mean free path neglect the effects of perpendicular diffusion [*Kelly et al.*, 2012]. These effects have been incorporated into such calculations only relatively recently [see, *e.g.*, *Dalla et al.*, 2003; *Zhang et al.*, 2009; *Dröge et al.*, 2010; *Kelly et al.*, 2012].

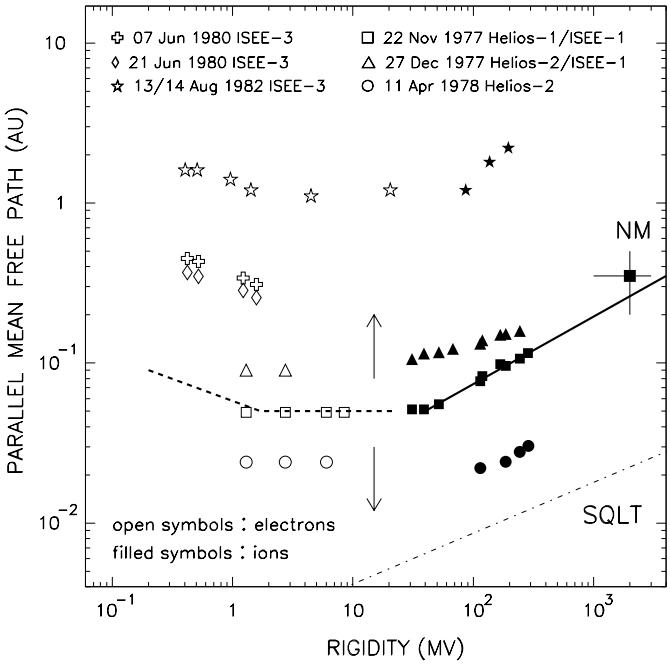

Figure 4.3: Observed rigidity dependences of proton and electron parallel mean free paths, reported for several solar energetic particle events by *Dröge* [2000].

Palmer [1982] reports that the various observations of $\lambda_{\parallel}$ ranged over two orders of magnitude, attributing this to the different transport models used to calculate them. Some models (*e.g. Lin* [1974]) assumed diffusion through a spherically symmetric medium with a uniform diffusion coefficient, ignoring convection, while others included convective and adiabatic effects, and assumed diffusion to be anisotropic (*e.g. Zwickl and Webber* [1977]). Some of the fits also neglected the possible effects of extended particle injection at the Sun, an omission likely to underestimate the value of the parallel diffusion coefficient [*Palmer*, 1982]. Taking these model-related factors into account, and neglecting results based on scatter-free events (solar particle events of relatively short duration that yield parallel mean free paths greater than 1 AU at Earth), *Palmer* [1982] find a consensus range of values which places the parallel mean free paths in a range of $0.08 - 0.3$ AU for rigidities extending from $0.0005 - 5$ GV.

Palmer [1982] compares the observed parallel mean free paths with those predicted by the magnetostatic slab quasi-linear theory (QLT) of *Jokipii* [1966] and find two major discrepancies. Firstly, the observed mean free paths can be up to an order of magnitude larger than those predicted by that particular theory, and secondly, that the observed mean free paths appear to be relatively rigidity-independent, reporting that, even though observations indicate a possible minimum for $\lambda_{\parallel}$ as a function of rigidity, more data would be required to make any positive conclusions on the matter.

A possible factor to affect the mean free paths not fully considered by *Palmer* [1982] is the effect the solar activity cycle would have on them. This would be somewhat masked in the observations of which the consensus is composed, as most solar particle events considered

occurred during periods of ascending to high solar activity. *Chen and Bieber* [1993] do find that larger mean free paths are associated with solar minima, and smaller mean free paths with solar maxima, and report a mean free path dependence on solar magnetic polarity. These authors, from an analysis of cosmic-ray anisotropies and gradients as observed by means of neutron monitors, find the high energy parallel mean free path is $\sim 40\%$ larger during $A < 0$ and at solar minimum. This then would imply that the Palmer consensus values may be a lower estimate for the parallel mean free path.

Bieber et al. [1994] revisit the various observations of which the Palmer consensus is comprised, dividing them into observations for electrons and protons separately, as is shown in Fig. 4.2, and also incorporate observations subsequent to the publication of Palmer's results reported by *Beeck et al.* [1987], *Bieber and Pomerantz* [1983], *Bieber et al.* [1986], *Chen and Bieber* [1993], *Dröge et al.* [1990], *Kane et al.* [1985], *Lin* [1985], and *Ruffolo* [1991]. Although some of these studies (*e.g. Chen and Bieber* [1993]) employ alternative methods to calculate cosmic-ray mean free paths, many of these studies continue to fit solar energetic particle events, but with increasingly complex models (*e.g. Ruffolo* [1991]).

Comparison of proton and electron results led *Bieber et al.* [1994] to conclude that below 25 MV the Palmer consensus pertains to electrons, and to protons above that rigidity. Furthermore, they find significant variations in magnitude of the observed mean free paths on an event-by-event basis, arguing that this would possibly obscure the rigidity dependence of a consensus range as reported by *Palmer* [1982]. When individual events are considered, *Bieber et al.* [1994] find that, at least for protons, the rigidity dependence of the magnetostatic slab quasi-linear theoretical result appears to be accurate, although the theoretical mean free paths remain well below all observed values. The electron mean free paths, however, appeared to behave in a fundamentally different manner at low rigidities. *Bieber et al.* [1994] report that the electron mean free paths at ~ 1.4 MV are essentially the same as those for protons at ~ 187 MV, but display a flat rigidity dependence at low rigidities, also reported by *Dröge* [1994] for $1 - 10$ MV electrons. *Dröge* [2000], and *Dröge* [2003], in subsequent studies of electron and proton mean free paths using fits of solar energetic particle events, and using a focused transport model, report detailed observations of the rigidity dependences of these mean free paths, illustrated in Fig. 4.3. These findings essentially agree with those of *Bieber et al.* [1994], displaying a low-energy electron mean free path fundamentally different to that of the protons. The agreement also extends to the large variations in magnitude observed for mean free paths, depending on the event considered. It is interesting to note, however, that although the magnitude of the mean free path changes with different events, the rigidity dependences remain essentially the same.

Bieber et al. [1994] resolved to the discrepancies between theory and observation illustrated in Fig. 4.2 by considering the effects of composite slab/2D turbulence (see Subsection 2.2.3) as opposed to purely slab turbulence. They argue that 2D fluctuations contribute little to parallel scattering, and in addition employed models of dynamical turbulence (see Subsection 2.2.6), as

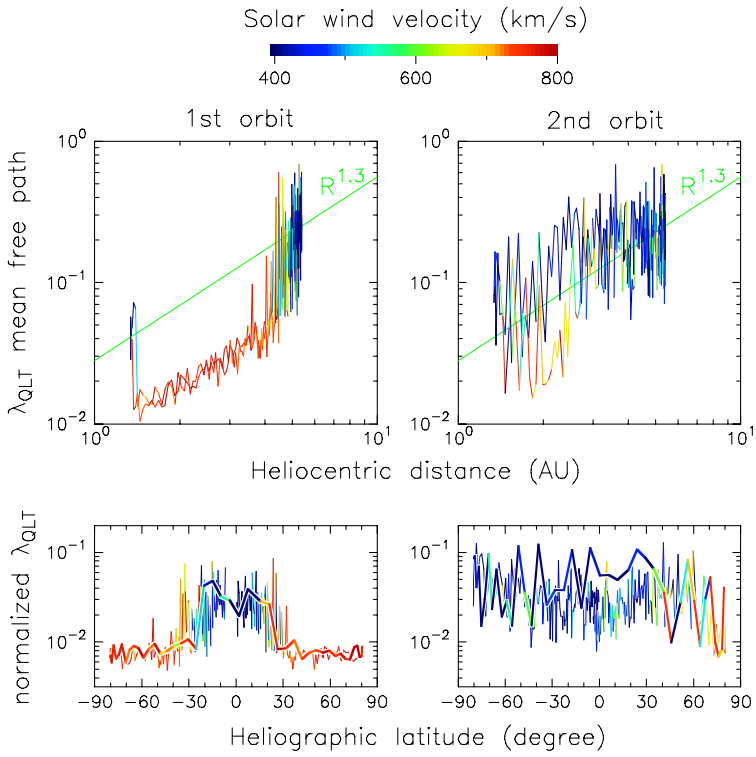

Figure 4.4: Parallel mean free path for 1 MeV protons (in AU) as calculated by *Erdös and Balogh* [2005] from HMF fluctuation spectra observed by *Ulysses* during its first and second fast latitude scans, using standard quasi-linear theory. Colour of line indicates solar wind speed, in that red denotes a high speed, and blue a low speed.

opposed to purely magnetostatic turbulence, to calculate the theoretical mean free paths using quasi-linear theory. The assumption of composite turbulence yielded larger theoretical mean free paths for both species, well within the Palmer consensus range, due in part to the smaller slab variance used as input for the theoretical spectrum. The use of the random sweeping and damping models of dynamical turbulence yielded a rigidity dependence for the electron mean free path in agreement with observations.

Detailed, piecewise analytical expressions for mean free paths based on dynamical turbulence have been calculated by *Teufel and Schlickeiser* [2002, 2003]. One should keep in mind, however, that *Dröge and Kartavykh* [2009] find a strong disagreement between observed electron pitch angle distributions and those predicted by the dynamical quasi-linear theory employed by *Bieber et al.* [1994] and subsequent authors. *Shalchi* [2007] argues that the problem of too-small QLT parallel mean free paths can alternatively be solved by assuming a form for the turbulence power spectrum different to that used by *Bieber et al.* [1994], and hence without the assumption that only the slab modes affect parallel particle scattering.

Lastly, it is of interest to consider any possible latitudinal dependences of observed mean free paths. *Erdös and Balogh* [2005] employ observed *Ulysses* magnetic field fluctuation spectra and use standard quasi-linear theory to calculate parallel mean free paths along that spacecraft's trajectory, during solar minimum and during solar maximum conditions, shown in Fig. 4.4.

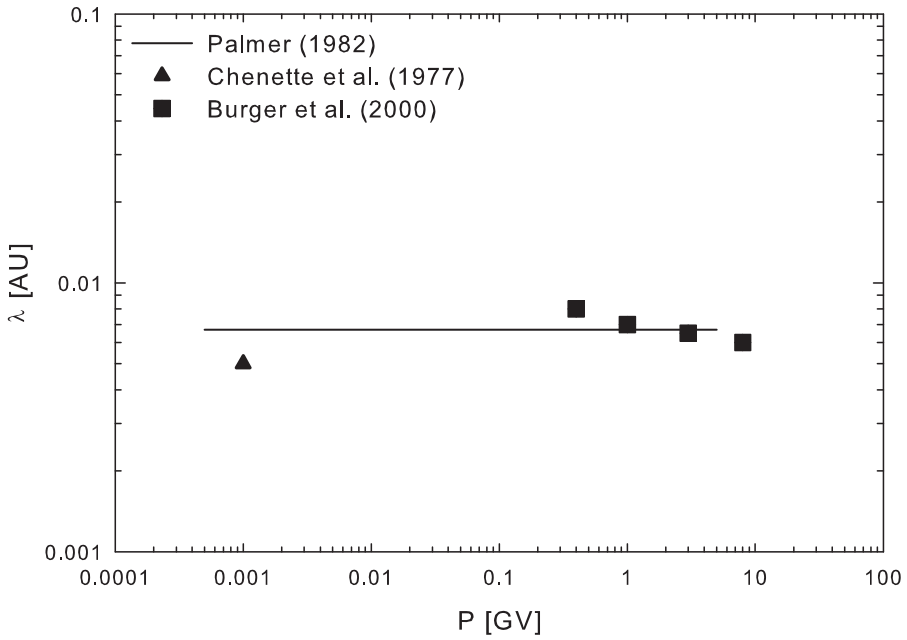

Figure 4.5: Perpendicular mean free paths observed by *Chenette et al.* [1977] and calculated by *Burger et al.* [2000], with *Palmer* [1982] consensus values.

The values in the lower two panels are normalised using an approximate $\sim r^{1.3}$ radial dependence indicated in the top two panels, due to the complicated spacecraft trajectory (see Fig. 3.16). Although the assumption that quasi-linear theory accurately portrays the particle mean free path is explicit, this result is nevertheless an indication of a possible latitudinal variation of this quantity. The bottom left panel of Fig. 4.4 shows a mean free path that varies considerably as a function of solar wind speed during the first solar minimum orbit, with significantly greater values in the streamer belt with its slower solar wind speed, as opposed to ~ 40 % lower values at higher latitudes, where the fast solar wind is predominant. The lower right panel of the same figure shows mean free paths calculated during the second solar maximum orbit. These show considerably less large-scale latitudinal variation, and in value resemble what was calculated for the first orbit in the ecliptic plane.

The perpendicular mean free path

The perpendicular mean free path is even more difficult to pin down observationally than the parallel mean free path. *Palmer* [1982] reports a consensus value of $\lambda_\perp \approx 0.0067$ AU over the same rigidity range of 0.0005 to 5 GV as that for the parallel mean free path, by considering results acquired by various techniques. These methods include the study of the cross-field diffusion of energetic particles like Jovian electrons [see, *e.g.*, *Chenette et al.*, 1977] and solar flare protons [see, *e.g.*, *Lupton and Stone*, 1973]; the study of magnetic diffusion at the Sun itself and fluctuations in the heliospheric magnetic field [see, *e.g.*, *Jokipii and Parker*, 1969; *Hedgecock*, 1975]; and the investigation of misalignments of the HMF and observed cosmic-ray anisotropies [see,

e.g., *Palmer and Jokipii*, 1982]. A full discussion of these techniques can be found in *Palmer* [1982]. The first of these methods, especially in the case where Jovian electrons are considered, is rendered difficult by the need to extrapolate values for the mean free path to 1 AU, in that this requires fits to be made for the radial dependences of the variances associated with the various components of the heliospheric magnetic field [*Palmer*, 1982]. It should be noted that *Palmer* [1982] reports a large spread of observed values about the reported consensus value for the perpendicular mean free path.

Burger et al. [2000] approached the problem somewhat differently, in that these authors report values for $\lambda_\perp$ at Earth required to fit galactic proton latitude gradients and are shown along with the Palmer consensus and the findings of *Chenette et al.* [1977] in Fig. 4.5. These values, however, have to be taken in the context of the assumptions made for various parameters in the cosmic-ray modulation code used, such as the assumed forms and dependences of the diffusion coefficients. That being said, the observations presented in Fig. 4.5 all seem to consistently imply that the perpendicular mean free path is relatively independent of rigidity at the energies concerned.

4.2.2 Numerical simulations

An alternative route to gathering information as to the possible behaviour of mean free paths, both parallel and perpendicular, is by means of direct numerical simulation. Various methods to do so are employed, but the most general approach involves solving the Lorentz equation for many particles in a simulated box, within which a magnetic field with a uniform and a fluctuating component is specified. The fluctuating component is constructed by assuming various turbulence geometries, the assumption of which being usually motivated by spacecraft observations. A detailed account of an example of the implementation and application of such a model to calculate diffusion coefficients numerically, with the accompanying intricacies involved, which is also used by *e.g. Mace et al.* [2000], *Qin et al.* [2002a], *Qin et al.* [2002b] and *Minnie et al.* [2007a], can be found in *Qin* [2002].

The parallel mean free path

The picture given by the various numerical simulations as to the validity of the QLT treatment of parallel scattering is somewhat mixed. *Michałek and Ostrowsky* [1996] consider parallel mean free paths as functions of the magnetic field fluctuation amplitudes δB and find excellent agreement for low-amplitude (small $\delta B/B$) turbulence of the predictions of QLT with their simulations. They report that at higher assumed fluctuation levels the simulated parallel diffusion coefficient does not decrease with increasing δB as does the theoretical coefficient, although the discrepancy is not large. In an extensive study, considering three-dimensional turbulence models, *Giacalone* [1999a] find that the energy dependence of the simulated parallel diffusion coefficient is well described by QLT. When considering simulated parallel mean free

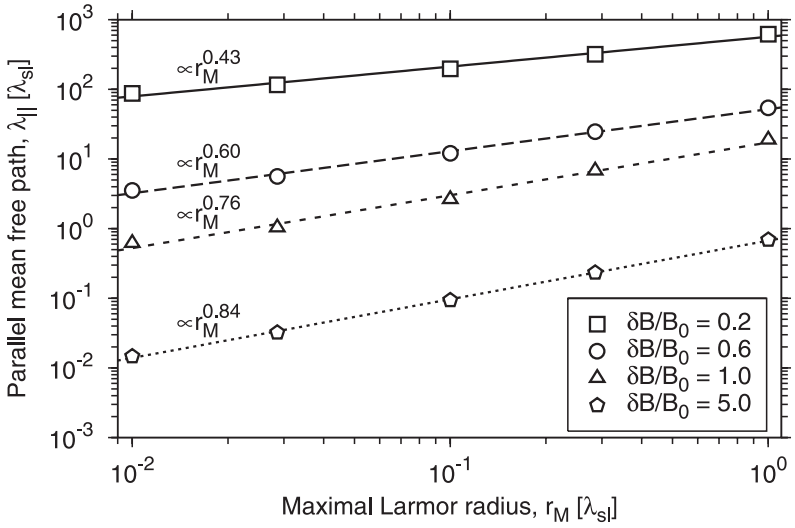

Figure 4.6: Parallel mean free paths numerically simulated, for various levels of turbulence, by *Minnie et al.* [2007a]. Note that mean free path values are normalised to those assumed for the slab turnover scale by these authors.

paths for the compound turbulence model, as compared to those acquired assuming isotropic turbulence, the prediction of QLT better agrees with the isotropic turbulence simulations. Also, these authors report that the use of composite turbulence leads to a simulated parallel mean free path two to three times larger than that acquired assuming isotropic 3D turbulence. They argue that, given their assumption that only 20 % of the turbulent fluctuation power resides in the slab fluctuations, the expected difference from QLT would be a factor of 5. *Giacalone* [1999a] attribute this difference to the omission of higher-order terms in the derivation of QLT, which would affect how this theory describes the scattering of particles with pitch angles approaching $90°$. For more information on this particular shortcoming of QLT, the reader is invited to consult *Shalchi* [2009] for a general discussion, and *Tautz et al.* [2008] for a proposed solution. *Casse et al.* [2002] find excellent agreement with the QLT-predicted $P^{1/3}$ rigidity dependence at lower rigidities, even at the highest of the broad range of turbulence levels these authors consider in their simulations. This finding is confirmed by the simulations of *Candia and Roulet* [2004] for various inertial range spectral wavenumber dependences. These results are, however, somewhat surprising, as QLT is based on the assumption of small magnetic field fluctuation amplitudes, and relatively small cumulative modifications to a particle's unperturbed orbit [*Jokipii*, 1966], and would be expected to only be applicable at the highest rigidities, and lowest fluctuation amplitudes [see, *e.g.*, *Dröge*, 2003, 2005; *Minnie et al.*, 2007a].

Figure 4.6 shows the parallel mean free paths simulated for various levels of turbulence by *Minnie et al.* [2007a], following an approach outlined in *Minnie* [2006] and *Qin* [2002], as functions of the Larmor radius. These simulations were performed assuming values for turbulence parameters appropriate at Earth, with an 80/20 2D/slab anisotropy, and a slab turnover scale equal to one-tenth of the value of the 2D turnover scale. Fig. 4.6 also shows various fitted Larmor radii (and hence rigidity) dependences for the parallel mean free path at the differ-

ent turbulence levels considered. Two points of interest are readily seen. Firstly, the rigidity dependence of the simulated parallel mean free path appears to depend on the level of the turbulence, becoming progressively more steep as the turbulence level increases. Secondly, that the rigidity dependences are never the same as that predicted by QLT, coming close to a $P^{1/3}$ dependence only at the lowest levels of turbulence. *Minnie et al.* [2007a] also directly compare the theoretical predictions of QLT (based on expressions employed by *Zank et al.* [1998]) and those of the weakly non-linear theory (WNLT) of *Shalchi et al.* [2004b], finding that the WNLT yields results closer to the simulated values for higher levels of turbulence than does QLT. QLT agrees best with simulations for the lowest turbulence level considered, but the agreement becomes significantly worse for all subsequently increased turbulence levels. Both scattering theories considered for the parallel mean free path by *Minnie et al.* [2007a] fail to reproduce the turbulence level-dependent change in rigidity dependence seen for the numerically simulated parallel mean free paths. *Matthaeus et al.* [2003] also find that for low levels of turbulence the result predicted by QLT agrees well with their simulations concerning the parallel diffusion coefficient at high rigidities, but deviates at the lowest rigidities considered. The simulations of *Qin et al.* [2006], however, paint a somewhat more complicated picture of parallel diffusion. These authors report that parallel diffusion can be affected by large levels of 2D turbulence. This would imply that the standard QLT approach, where only slab modes are assumed to affect parallel diffusion, is an oversimplification.

Simulations performed by *Qin and Shalchi* [2012] show that their simulated parallel mean free path is not greatly affected by the low-wavenumber behaviour of the slab turbulence power spectrum. Here again, the theoretical mean free paths yielded by QLT agree well with the high-rigidity simulated parallel mean free paths, but considerably less so at low to intermediate rigidities. The theoretical values predicted by WNLT are also shown by these authors to be relatively insensitive to the low wavenumber behaviour of the spectrum, and are also found to be in much better agreement, for a broad range of rigidities, with simulations. This, *Qin and Shalchi* [2012] argue, is due to this theory's description of the resonance broadening due to the effects of perpendicular diffusion.

The perpendicular mean free path

Jokipii et al. [1993] showed analytically that when a spatial coordinate is ignorable in the turbulence model considered, *e.g.* assuming purely slab turbulence, the perpendicular transport of particles is inhibited, which then becomes limited to that due to the random meandering of field lines perpendicular to the mean field direction. This kind of perpendicular transport, known as field-line random walk (FLRW), was first considered by *Jokipii* [1966] and *Forman et al.* [1974]. Numerical particle simulations by *Giacalone and Jokipii* [1999], *Mace et al.* [2000], *Matthaeus et al.* [2003] and *Minnie et al.* [2007a] find that this theory does not accurately describe their simulated transverse diffusion coefficients. This is illustrated in Fig. 4.7, which shows the results acquired by *Matthaeus et al.* [2003] (solid line), who assume composite turbulence and

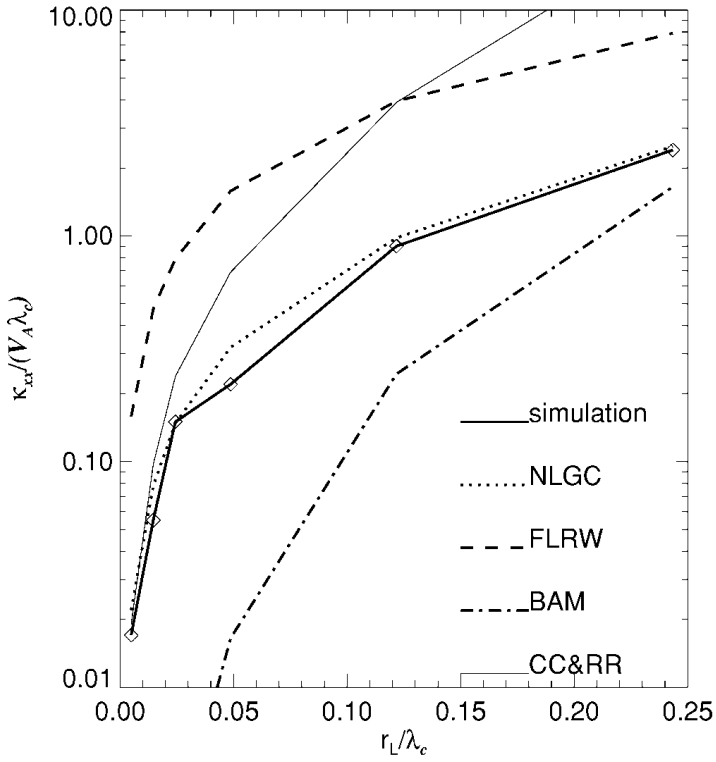

Figure 4.7: Comparison of perpendicular diffusion coefficients as function of the ratio of the maximal Larmor radius R_L to assumed slab correlation length (here denoted by λ_c) predicted by various theories, with the results of numerical particle simulations, for 20% slab and 80% 2D turbulence [*Matthaeus et al.*, 2003]. Relevant line types are discussed in the text.

choose turbulence parameters comparable to those observed at Earth. These results indicate a clear overestimation, at all rigidities considered, of the perpendicular diffusion coefficient by FLRW (dashed line). *Matthaeus et al.* [2003], in agreement with *Mace et al.* [2000], do find that the theory of perpendicular diffusion presented by *Bieber and Matthaeus* [1997] (dashed-dotted line) is in better agreement with their simulations than the predictions of the FLRW theory, although this agreement is far from perfect. *Candia and Roulet* [2004] note, however, that this theory is derived with the assumption that particles only experience small deviations from essentially helical trajectories, implying that the *Bieber and Matthaeus* [1997] theory would only be accurate for low levels of turbulence. From Fig. 4.7 it can be seen that the theoretical values yielded by the non-linear guiding center (NLGC) theory proposed by *Matthaeus et al.* [2003] (dotted line) agree very well with simulations (solid line).

Figure 4.8 shows perpendicular mean free paths simulated by *Minnie et al.* [2007a] for several turbulence levels, as functions of maximal gyroradius. Clearly, the rigidity dependence of these mean free paths becomes steeper at higher levels of turbulence. These authors compare their simulated results with the theoretical predictions of FLRW, the weakly non-linear theory (WNLT) proposed by *Shalchi et al.* [2004b], and NLGC theory. *Minnie et al.* [2007a] find the agreement between the simulations and the theoretical perpendicular mean free paths yielded by the WNLT is considerably better, especially at intermediate fluctuation amplitudes,

than with those provided by the FLRW theory, although at the smallest fluctuation amplitudes FLRW is closer to the simulations. The perpendicular mean free paths yielded by NLGC are found to agree very well with numerical simulations at low and intermediate turbulence levels, although here again the agreement breaks down for larger fluctuation amplitudes, although to a lesser extent for this theory than for WNLT or FLRW.

Simulations performed by *Kóta and Jokipii* [2000] comparing the effects of three-dimensional and 2D turbulence on the transport of particles perpendicular to the magnetic field, also suggest that any consideration of reduced-dimension turbulence inhibits the transverse diffusion of particles. This finding is confirmed by *Qin et al.* [2002b], who report that perpendicular transport becomes subdiffusive when reduced-dimension turbulence, in particular magnetostatic slab turbulence, is assumed. *Qin et al.* [2002a], however, show with their simulations that diffusive behaviour is effectively recovered if sufficient levels of transverse turbulence are assumed. In light of the above findings, a problem arises with the NLGC theory, which assumes that slab modes contribute to perpendicular diffusion. Hence, for the case of purely magnetostatic slab turbulence, this theory would still yield a finite perpendicular diffusion coefficient, in contradiction to the results of *Kóta and Jokipii* [2000] and *Qin et al.* [2002a]. *Shalchi* [2006] proposed an extended non-linear guiding center theory (ENLGC) which improves on the treatment of the slab contribution to perpendicular scattering. He finds that the slab contribution is essentially subdiffusive and effectively resolves the discrepancy between theory and simulation. *Shalchi* [2006] showed by means of numerical simulations, utilizing the code used by *Mace et al.* [2000] and *Qin et al.* [2002b], that the ENLGC theory provides results in much better agreement with simulations than those yielded by the NLGC theory, for purely slab, slab-dominated composite, and 2D dominated composite turbulence. The ENLGC theory, however, is only applicable when the assumption of two-component slab/2D turbulence is made [*Tautz and Shalchi*, 2011], as is done in the present study. This limitation was resolved by an improved, or unified, NLGC (UNLGC) presented by *Shalchi* [2010a], based on the Fokker-Planck equation. This approach also yields zero perpendicular diffusion coefficients for the case of magnetostatic slab turbulence, reducing to the FLRW theory, and to a theory very closely resembling ENLGC, in the appropriate limits.

Assuming a magnetostatic 2D/slab composite turbulence model in their numerical particle simulations, *Tautz and Shalchi* [2011] compare theoretical results yielded by the standard NLGC and the UNLGC theories with simulations. Both theories agree reasonably well with simulations at lower levels of slab turbulence, but at higher levels *Tautz and Shalchi* [2011] report a better agreement with simulations for the UNLGC theory. They argue that this is due to the assumption in this theory, held in common with ENLGC, that only the 2D fluctuations play a role in perpendicular diffusion. It must be noted, however, that these authors assume in their simulations that the 2D and slab turnover scales are equal, an assumption inconsistent with spacecraft observations [see, e.g. *Weygand et al.*, 2011]. *Qin and Shalchi* [2012] consider various forms for the low-wavenumber, energy range of the 2D turbulence power spectrum

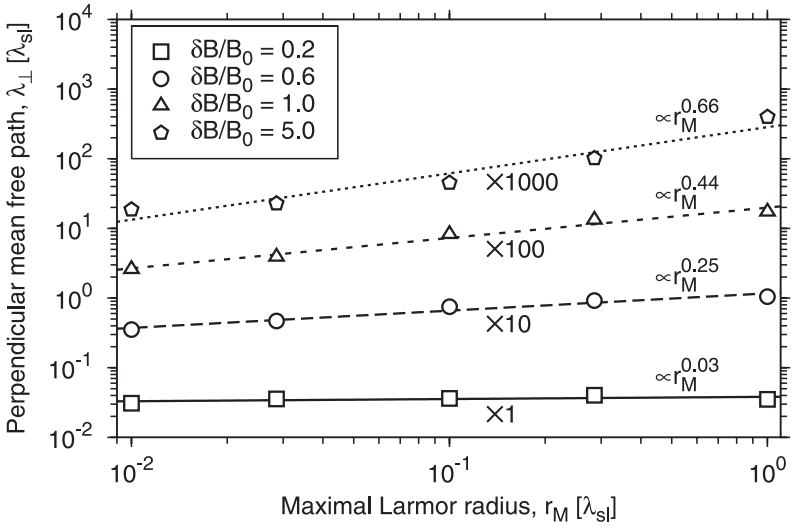

Figure 4.8: Perpendicular mean free paths numerically simulated for various levels of turbulence by *Minnie et al.* [2007a]. Note that mean free path values are normalised to the slab turn-over scale by these authors.

employed in their numerical simulations, reporting simulated perpendicular mean free paths to be highly sensitive to this wavenumber dependence. Furthermore, the NLGC and ENLGC theoretical results derived for the various spectral forms considered agree very well with the simulation results. It is interesting to note that, for the turbulence conditions assumed, the NLGC and ENLGC theories provide very similar values for the perpendicular mean free path. This is because 2D turbulence has been assumed to be dominant, and thus one of the main distinctions between the theories, *viz.* that the ENLGC theory assumes that slab modes do not affect the perpendicular diffusion of particle, while the NLGC theory does, is less significant. Hence, *Qin and Shalchi* [2012] conclude that in scenarios where 2D turbulence may not be dominant, the two theories will yield different results.

4.2.3 Motivating the choice of scattering theories utilized

The choice of scattering theory to be used is crucial to any study of cosmic-ray modulation. This task, however, is rendered extremely difficult by the fact that one must somehow discriminate amongst a plethora of theories, based on observations and test particle simulations applicable almost exclusively to conditions prevalent at Earth. Figure 4.9 illustrates the turbulence levels yielded by the *Oughton et al.* [2011] turbulence transport model at various colatitudes as functions of radial distance and shows quite clearly that a large range can occur within the heliosphere. Simulations [see, e.g. *Minnie et al.*, 2007a] show that the accuracy of different theories depends on the level of turbulence and imply that there does not appear to be a 'one size fits all' scattering theory. The green lines in the top panel of Fig. 4.9 indicate the turbulence levels considered by *Minnie et al.* [2007a].

In the present study, the QLT of *Jokipii* [1966] is used to model parallel diffusion in composite

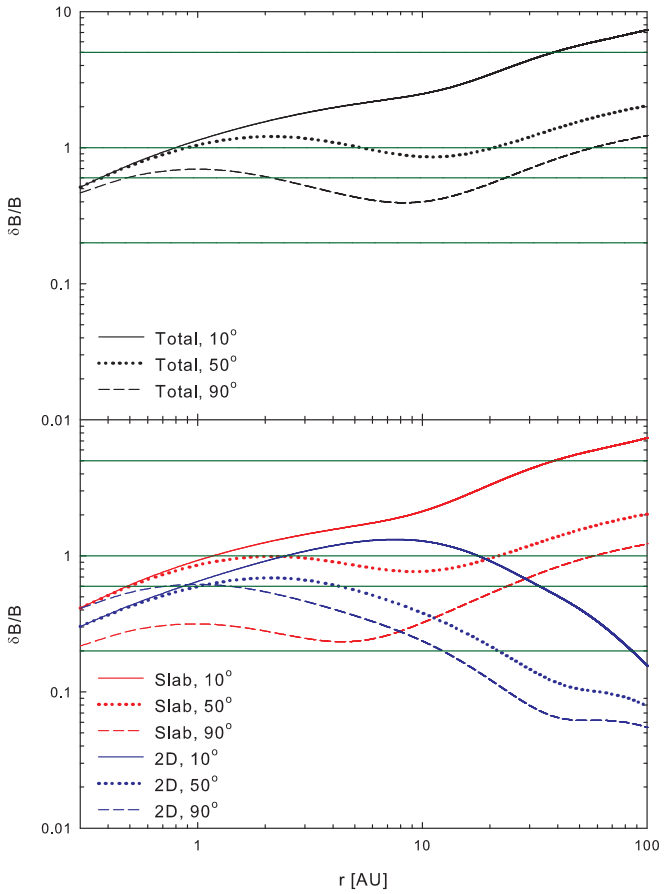

Figure 4.9: Turbulence levels yielded by the *Oughton et al.* [2011] turbulence transport model as functions of heliocentric radial distances at various colatitudes. Top panel represents the total turbulence level, while the bottom panel represents the slab and 2D turbulence levels individually. Note that the heliospheric magnetic field magnitude here used is that of the Parker model. Green lines indicate levels of turbulence considered by *Minnie et al.* [2007a].

turbulence [*Bieber et al.*, 1994], employing expressions for the parallel mean free path based on the results of *Teufel and Schlickeiser* [2003]. This decision is motivated by the fair agreement of the resulting parallel mean free paths with observations, as well as the reasonable agreement obtained for simulations with relatively low levels of turbulence. For the perpendicular mean free path, the ENLGC theory of *Shalchi* [2006], similar to the NLGC theory of *Matthaeus et al.* [2003], is employed, following to some degree the approach of *Shalchi et al.* [2004a]. Not only do the predictions of this theory agree well with numerical simulations over a broad range of rigidities and turbulence levels, but it also successfully reproduces the relatively flat rigidity dependences observed for the perpendicular mean free path at 1 AU. Furthermore, the good agreement of ENLGC results with those of numerical simulations performed for slab-dominated composite turbulence as opposed to the results of the standard NLGC formulation reported by *Shalchi* [2006], given the slab-dominated scenario yielded by the *Oughton et al.* [2011] model used in the present study to model various turbulence quantities, motivates the choice of this theory to describe perpendicular diffusion in the present study.

Other recent theories of perpendicular diffusion, such as the unified/improved non-linear theory presented by *Shalchi* [2010a] and the extension to NLGC proposed by *le Roux et al.* [2010], as well as the findings of *Ruffolo et al.* [2012], are not considered here. Lastly, as the effects of intermittency are also not considered in the present study, due in part to the assumption of homogeneous turbulence implicit to the use of the *Oughton et al.* [2011] model, the results of *le Roux* [2011] cannot presently be taken into consideration.

4.3 The parallel mean free path

Teufel and Schlickeiser [2002, 2003] derive analytical expressions for the parallel mean free paths of cosmic rays, for both the damping and random sweeping models of dynamical turbulence (discussed in Subsection 2.2.6), by employing the quasi-linear theory (QLT) of *Jokipii* [1966]. As a point of departure, the particle mean free path parallel to the assumed background magnetic field can be expressed by [see, *e.g.*, *Jokipii*, 1966; *Bieber et al.*, 1994]

$$\lambda_{\parallel} = \frac{3v}{8} \int_{-1}^{1} d\mu \frac{(1-\mu^2)^2}{D_{\mu\mu}(\mu)}, \tag{4.7}$$

with v the particle speed, μ the cosine of the particle's pitch angle, and $D_{\mu\mu}(\mu)$ the pitch angle Fokker-Planck coefficient. This latter quantity is calculated by *Teufel and Schlickeiser* [2002] from ensemble-averaged first-order corrections to particle orbits in a weakly turbulent magnetic field for both the random sweeping (RS) and damping (DT) models of dynamical turbulence in terms of the wavenumber $k_{\parallel}$ parallel to the uniform background field B_o, such that

$$D_{\mu\mu}(RS) = \frac{2\pi\Omega_{ci}^2(1-\mu^2)}{B_o^2} \int_0^{\infty} dk_{\parallel} G^{slab}(k_{\parallel}) q_D \left[\frac{1}{1+q_D^2(k_{\parallel}v_{\parallel}-\Omega_{ci})^2} + \frac{1}{1+q_D^2(k_{\parallel}v_{\parallel}+\Omega_{ci})^2} \right], \tag{4.8}$$

with $v_{\parallel}$ the component of the particle's velocity parallel to B_o, Ω_{ci} denoting the proton gyrofrequency, and

$$D_{\mu\mu}(DT) = \frac{\pi^{3/2}\Omega_{ci}^2(1-\mu^2)}{B_o^2} \int_0^{\infty} dk_{\parallel} G^{slab}(k_{\parallel}) q_D f(k_{\parallel}), \tag{4.9}$$

with

$$f(k_{\parallel}) = \exp\left(-q_D^2(k_{\parallel}v_{\parallel}-\Omega_{ci})^2/4\right) + \exp\left(-q_D^2(k_{\parallel}v_{\parallel}+\Omega_{ci})^2/4\right). \tag{4.10}$$

In keeping with the notation employed by *Teufel and Schlickeiser* [2002, 2003], $q_D = (\alpha_d V_A \left|k_{\parallel}\right|)^{-1}$ with $\alpha_d \in [0,1]$ a parameter that adjusts dynamical effects, such that a value of zero corresponds to the magnetostatic limit, while a value of unity assumes that the underlying turbulence is strongly dynamical [*Bieber et al.*, 1994].

The slab omnidirectional turbulence power spectrum used by *Teufel and Schlickeiser* [2003], discussed and illustrated in Subsection 2.4.2, is repeated here for ease of reference:

$$G^{slab}(k_{\parallel}) = \begin{cases} g_o k_{min}^{-s} & \text{for } |k_{\parallel}| \leq k_{min}; \\ g_o |k_{\parallel}|^{-s} & \text{for } k_{min} \leq |k_{\parallel}| \leq k_d; \\ g_1 |k_{\parallel}|^{-p} & \text{for } |k_{\parallel}| \geq k_d. \end{cases} \tag{4.11}$$

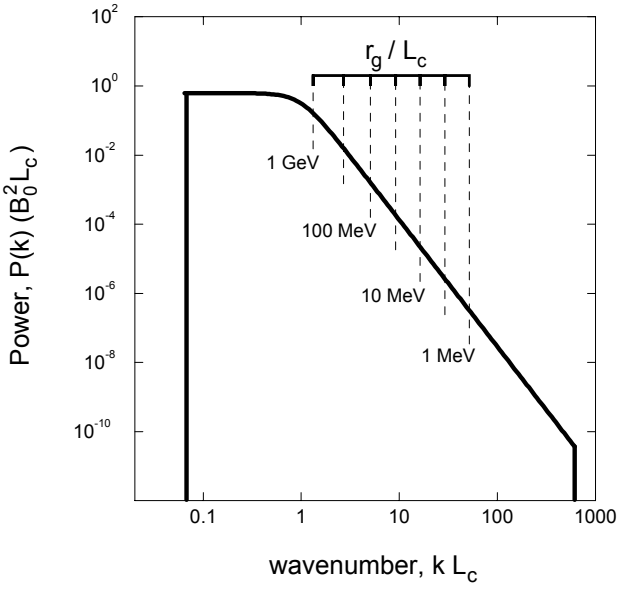

Figure 4.10: Power spectrum used in the numerical particle simulations of *Giacalone and Jokipii* [1999]. Wavenumbers at which protons of various energies resonate with the power spectrum are indicated, as function of proton gyroradius. Note that in this figure L_c denotes a spectral turnover scale from the energy to the inertial range.

Here $g_1 = g_0 k_d^{p-s}$, where $k_{min} = 1/\lambda_s$ and $k_d = 1/\lambda_d$ denote respectively the wavenumbers associated with the onset of the inertial and dissipation ranges, and

$$g_o = \frac{\delta B_{slab}^2 k_{min}^{s-1}(s-1)}{8\pi}\left[s + \frac{s-p}{p-1}\left(\frac{k_{min}}{k_d}\right)^{s-1}\right]^{-1}, \tag{4.12}$$

with s and p the spectral indices (in absolute value) of the inertial and dissipation ranges, respectively, and are subjected to the conditions that $p > 2$ and $1 < s < 2$.

Utilizing the above expression for the slab spectrum, *Teufel and Schlickeiser* [2003] derive expressions for the parallel mean free path for the case of random sweeping dynamical turbulence, given by

$$\lambda_{\parallel}(RS) = \frac{B_o^2}{\delta B_{slab}^2}\frac{3s}{\sqrt{\pi}(s-1)}\frac{R^2}{k_{min}b}K_{RS} \tag{4.13}$$

and for the damping model of dynamical turbulence,

$$\lambda_{\parallel}(DT) = \frac{B_o^2}{\delta B_{slab}^2}\frac{3s}{(s-1)}\frac{R^2}{k_{min}a}K_{DT} \tag{4.14}$$

where

$$\begin{aligned} a &= \frac{v}{\alpha_d V_A}, \\ b &= a/2, \\ R &= R_L k_{min}, \\ Q &= R_L k_d, \end{aligned} \tag{4.15}$$

with $R_L = P/B_o$ denoting the maximal Larmor radius, and $P = pc/|q|$ the particle rigidity. $K_{RS,DT}$ pertain to an analytical solution most appropriate to a certain range of the parameters listed in Eq. 4.15. These analytical solutions are listed in Table 4.1 for the RS model, and in Table 4.2 for the DT model, where

$$\begin{aligned} f_1 &= \frac{2}{p-2} + \frac{2}{2-s}, \\ f_2 &= \frac{\pi}{\sin(\pi s/2)}. \end{aligned} \tag{4.16}$$

The analytical solutions presented by *Teufel and Schlickeiser* [2003] are piecewise continuous, and hence are not ideal for the purposes of incorporation into a cosmic-ray modulation code. *Engelbrecht* [2008] considered the various solutions for the random sweeping model, listed in Table 4.1, and found that the solutions numbered 1, 7 and 9, corresponding as they do to realistic heliospheric conditions, can readily be used to construct a tractable, continuous expression for the electron (and also positron) parallel mean free path, given by

$$\begin{aligned} \lambda_{\parallel} &= \frac{3s}{\sqrt{\pi}(s-1)} \frac{R^2}{k_{min} b} \left(\frac{B_o}{\delta B_{slab}} \right)^2 \\ &\cdot \left[\frac{b}{4\sqrt{\pi}} + \left(\frac{1}{\Gamma(p/2)} + \frac{1}{\sqrt{\pi}(p-2)} \right) \frac{b^{p-1}}{Q^{p-s} R^s} + \frac{2}{\sqrt{\pi}(2-s)(4-s)} \frac{b}{R^s} \right]. \end{aligned} \tag{4.17}$$

Solution 1 corresponds to the contribution to particle scattering from the energy range of the slab power spectrum, solution 9 to that from the inertial range, and solution 7 to that of the dissipation range. It is assumed in QLT that particle scattering by magnetic field fluctuations occurs due to changes in a particle's pitch angle [see, *e.g.*, *Dröge*, 2003], this resonance occurring where fluctuations are of the order of the gyroradius [*Candia and Roulet*, 2004]. Therefore particles of the highest energy/rigidity, which have correspondingly large gyroradii, would only sample the largest of fluctuations, corresponding to the lower wavenumber parts of the spectrum. Hence, in Fig. 4.10, protons of the highest energy shown resonate with the smallest wavenumbers and *vice versa*. In reality, the above is not entirely true, as turbulence causes particles to experience a broadening of resonance. At 90° pitch, one can no longer even say that most pitch angle scattering is due to wavenumbers satisfying the condition that $k_{\parallel} = (\mu R_L)^{-1}$ [see, *e.g.*, *Qin and Shalchi*, 2012, and references therein].

Taking into account the fact that protons are not sensitive to the fluctuations in the dissipation range at the rigidities that concern the study of galactic cosmic-ray protons, *Engelbrecht* [2008] also construct, in a manner similar to that employed to acquire Eg. 4.17, a tractable and continuous expression for the proton parallel mean free path from solutions 1 and 9, such that

$$\lambda_{\parallel} = \frac{3s}{\sqrt{\pi}(s-1)} \frac{R^2}{k_{min} b} \left(\frac{B_o}{\delta B_{slab}} \right)^2 \left[\frac{b}{4\sqrt{\pi}} + \frac{2}{\sqrt{\pi}(2-s)(4-s)} \frac{b}{R^s} \right]. \tag{4.18}$$

The above two mean free path expressions have been utilized in this form in several cosmic-ray modulation studies [see, *e.g.*, *Burger et al.*, 2008; *Engelbrecht and Burger*, 2010; *Burger and Visser*, 2010; *Sternal et al.*, 2011].

Case no.	Case	K_{RS}
1	$1 \ll b \ll R \ll Q$	$\frac{b}{4\sqrt{\pi}}$
2	$1 \ll R \ll Q \ll b$	$\frac{b}{4\sqrt{\pi}} + [\frac{1}{\Gamma(p/2)} + \frac{1}{\sqrt{\pi}(p-2)}]\frac{b^{p-1}}{Q^{p-s}R^s}$
3	$1 \ll R \ll b \ll Q$	$\frac{b}{4\sqrt{\pi}}$
4	$b \ll 1 \ll R \ll Q$	$\frac{2}{3}\frac{s}{2-\gamma s-2s\ln b/R}$
5	$b \ll R \ll Q \ll 1$	$\frac{2}{3}\frac{s}{2-\gamma s-2s\ln b/R}$
6	$b \ll R \ll 1 \ll Q$	$\frac{2}{3}\frac{s}{2-\gamma s-2s\ln b/R}$
7	$R \ll Q \ll 1 \ll b$	$[\frac{1}{\Gamma(p/2)} + \frac{1}{\sqrt{\pi}(p-2)}]\frac{b^{p-1}}{Q^{p-s}R^s}$
8	$R \ll Q \ll b \ll 1$	$\frac{2}{3\Gamma(p/2)}\frac{b^p}{Q^{p-s}R^s}$
9	$R \ll 1 \ll b \ll Q$	$\frac{2}{\sqrt{\pi}(2-s)(4-s)}\frac{b}{R^s}$
10	$R \ll 1 \ll Q \ll b$	$[\frac{1}{\Gamma(p/2)} + \frac{1}{\sqrt{\pi}(p-2)}]\frac{b^{p-1}}{Q^{p-s}R^s} + \frac{2}{\sqrt{\pi}(2-s)(4-s)}\frac{b}{R^s}$
11	$R \ll b \ll 1 \ll Q$	$\frac{2}{3\Gamma(s/2)}\frac{b^s}{R^s}$
12	$R \ll b \ll Q \ll 1$	$\frac{2}{3\Gamma(s/2)}\frac{b^s}{R^s}$

Table 4.1: Analytical expressions for K_{RS} for the random sweeping model, from *Teufel and Schlickeiser* [2003].

Case no.	Case	K_{DT}
1	$1 \ll a \ll R \ll Q$	$\frac{a}{4\pi}$
2	$1 \ll R \ll Q \ll a$	$\frac{a}{4\pi} + \frac{a^2}{f_1 R^s Q^{p-s}}{}_2F_1\left(1, \frac{1}{p-1}, \frac{p}{p-1}; -\frac{\pi a}{f_1 Q}\right)$
3	$1 \ll R \ll a \ll Q$	$\frac{a}{4\pi}$
4	$a \ll 1 \ll R \ll Q$	$\frac{s}{3-3s\ln a/R}$
5	$a \ll R \ll Q \ll 1$	$\frac{s}{3-3s\ln a/R}$
6	$a \ll R \ll 1 \ll Q$	$\frac{s}{3-3s\ln a/R}$
7	$R \ll Q \ll 1 \ll a$	$\frac{a^2}{f_1 R^s Q^{2-s}}[{}_2F_1\left(1, \frac{1}{p-1}, \frac{p}{p-1}; -\frac{\pi a}{f_1}Q^{p-2}\right) - \frac{1}{3}{}_2F_1\left(1, \frac{3}{p-1}, \frac{p+2}{p-1}; -\frac{\pi a}{f_1}Q^{p-2}\right)]$
8	$R \ll Q \ll a \ll 1$	$\frac{2}{3f_1}\frac{a^2}{R^s Q^{p-s}}$
9	$R \ll 1 \ll a \ll Q$	$\frac{2}{\pi(2-s)(4-s)}\frac{a}{R^s}$
10	$R \ll 1 \ll Q \ll a$	$\frac{2}{\pi(2-s)(4-s)}\frac{a}{R^s} + \frac{a^2}{f_1 R^s Q^{p-s}}{}_2F_1\left(1, \frac{1}{p-1}, \frac{p}{p-1}; -\frac{\pi a}{f_1 Q}\right)$
11	$R \ll a \ll 1 \ll Q$	$\frac{2}{3f_2}\frac{a^s}{R^s}$
12	$R \ll a \ll Q \ll 1$	$\frac{2}{3f_2}\frac{a^s}{R^s}$

Table 4.2: Analytical expressions for K_{DT} for the damping turbulence model, from *Teufel and Schlickeiser* [2003]. Note that f_1 and f_2 are defined in Eq. 4.16.

Constructing similar expressions for the electron and proton parallel mean free paths for the damping turbulence piecewise analytical solutions of *Teufel and Schlickeiser* [2003] is relatively straightforward. This yields an electron/positron parallel mean free path given by

$$\begin{aligned}\lambda_{\parallel} &= \frac{3s}{(s-1)}\frac{R^2}{k_{min}a}\left(\frac{B_o}{\delta B_{slab}}\right)^2 \\ &\cdot \left[\frac{a}{4\pi} + {}_2F_1\left(1, \frac{1}{p-1}, \frac{p}{p-1}; -\frac{\pi a}{f_1}Q^{p-2}\right)\frac{a^2}{f_1 R^s Q^{p-s}} + \frac{2}{\pi(2-s)(4-s)}\frac{a}{R^s}\right], \quad (4.19)\end{aligned}$$

where terms corresponding to the contributions of the energy and inertial ranges are very similar to those in Eq. 4.17, with the parameter a here used instead of b. The hypergeometric function in the term corresponding to the dissipation range, however, makes the application of this model to cosmic-ray modulation studies somewhat more complicated than when the solutions corresponding to the random sweeping model are considered. Ostensibly, this hypergeometric function appears divergent, in that, for a hypergeometric function of the form

Variable	Energy Range	Inertial Range	Dissipation Range
k_{min}	$\sim k_{min} \equiv \lambda_s^{-1}$	$\sim k_{min}^{1-s} \equiv \lambda_s^{s-1}$	$\sim k_{min}^{1-s} \equiv \lambda_s^{s-1}$
k_D	-	-	$\sim k_D^{s-p}$
δB_{slab}	$\sim (\delta B_{slab})^{-2}$	$\sim (\delta B_{slab})^{-2}$	$\sim (\delta B_{slab})^{-2}$
V_A	-	-	$\sim V_A^{2-p}$
B_o	-	$\sim B_o^s$	$\sim B_o^p$
P	$\sim P^2$	$\sim P^{2-s}$	$\sim P^{2-p}$

Table 4.3: Various dependences of the random sweeping parallel mean free path for electrons (Equation 4.17), and for both the random sweeping and damping turbulence proton mean free path expressions (Equations 4.18 and 4.21), where only the energy and inertial range columns are applicable, adapted from *Engelbrecht* [2008]. A dash implies no explicit dependence on a quantity. Note that the dissipation range column does not apply to the damping turbulence expression for the electron parallel mean free path (Equation 4.19).

${}_2F_1(\alpha, \beta, \gamma; z)$ to converge on the unit circle defined by $|z| < 1$, the condition $\mathrm{Re}(\alpha + \beta - \gamma) < 0$ must hold [see, *e.g.*, *Gradshteyn and Ryzhik*, 2007]. This is clearly not the case for Eq. 4.19. Such a difficulty is, however, easily overcome. If both $\gamma - (\alpha + \beta)$ and $\alpha - \beta$ are not integers, γ is not a natural number, and $\arg(-z) < \pi$ for $|z| \geq 1$, then the errant hypergeometric function can be written as [*Gradshteyn and Ryzhik*, 2007]

$$ {}_2F_1(\alpha, \beta, \gamma; z) = {}_2 F_1(\alpha, \gamma - \beta, \gamma; z/(z-1))(1-z)^{-\alpha}. \tag{4.20} $$

The hypergeometric function in Eq. 4.19 satisfies these conditions, although the use of Eq. 4.20 requires that some caution needs be taken when the value of the spectral index in the dissipation range is chosen. The range of values reported by *Smith et al.* [2006] are, however, used in the present study, and satisfy the conditions implicit to the use of Eq. 4.20. The damping turbulence proton mean free path follows in much the same way, *viz*.

$$ \lambda_{\parallel} = \frac{3s}{(s-1)} \frac{R^2}{k_{min} a} \left(\frac{B_o}{\delta B_{slab}} \right)^2 \left[\frac{a}{4\pi} + \frac{2}{\pi(2-s)(4-s)} \frac{a}{R^s} \right], \tag{4.21} $$

where here, as in Eq. 4.18, it is assumed that the protons at rigidities relevant to this study are only scattered by inertial and energy range fluctuations. The dependences of the mean free path expressions given above at all rigidities are listed in Table 4.3. Note, however, that the low-rigidity dependences of the damping turbulence electron mean free path are omitted due to the more complicated form of this expression, depending as it does on a hypergeometric series. The assumption of either the random sweeping or the damping model of dynamical turbulence yields identical mean free paths at higher rigidities, as at these rigidities dynamical effects are less important. At lower rigidities, for protons, the picture is much the same. However, for electrons, the choice of a parallel mean free path derived using the assumption of the random sweeping or damping models of dynamical turbulence can have a considerable effect.

Figures 4.11 and 4.12 illustrate this in terms of the rigidity dependences. Note that in the present study the lowest rigidity considered is above 1 MV, and that the behaviour of the mean free path below this rigidity is therefore not discussed in what follows. Both figures represent

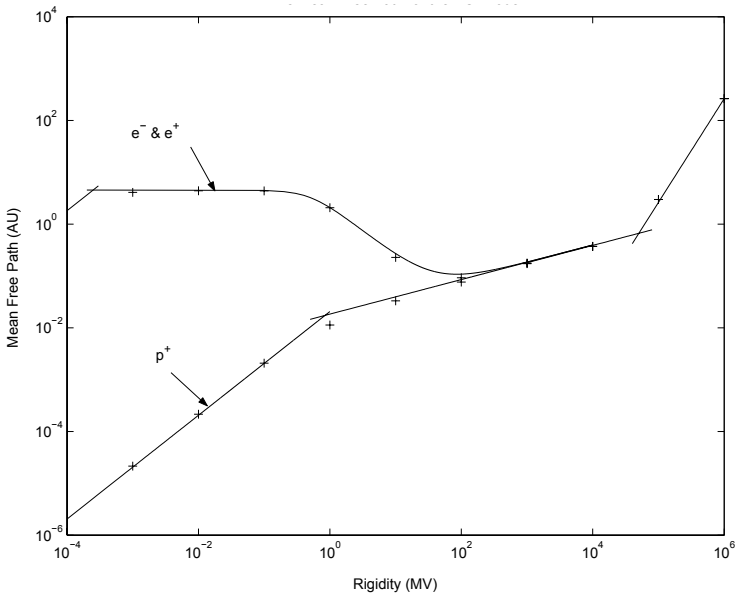

Figure 4.11: Random sweeping parallel mean free paths for protons and electrons/positrons, as functions of rigidity [*Teufel and Schlickeiser*, 2003]. Crosses indicate numerical solutions, solid lines approximate analytical solutions.

comparisons made by *Teufel and Schlickeiser* [2003] of the piecewise analytical solutions at Earth with the results of numerical integrations of Eq. 4.7 for both models, assuming the following set of parameters to hold at 1 AU:

$$\begin{aligned} k_{min} &= 10^{-10}\ \mathrm{m}^{-1} \\ k_D &= 2 \times 10^{-5}\ \mathrm{m}^{-1} \\ B_e &= 4.12\ \mathrm{nT} \\ V_A &= 33.5\ \mathrm{km/s} \\ \alpha_d &= 1 \\ s &= 5/3 \\ p &= 3. \end{aligned}$$

At high ($> 10^4$ MV) and intermediate ($\sim 100\mathrm{M}V < P < 10^4$ MV) rigidities both sets of parallel mean free paths display the respective P^2 and $P^{1/3}$ dependences expected from Table 4.3. However, as rigidities decrease, the electron mean free path acquired by assuming a random sweeping model of dynamical turbulence increases rapidly to significantly larger values than its damping turbulence counterpart. Lastly, it is worth noting how well the piecewise analytical solutions in Figures 4.11 and 4.12 agree with the numerical results.

The following subsection will characterize the spatial and rigidity dependences of the mean free paths of Equations 4.17, 4.18, 4.19 and 4.21, using as input for the slab variance and turnover scale the results yielded by the two-component turbulence transport model of *Oughton et al.* [2011] discussed in the previous chapter.

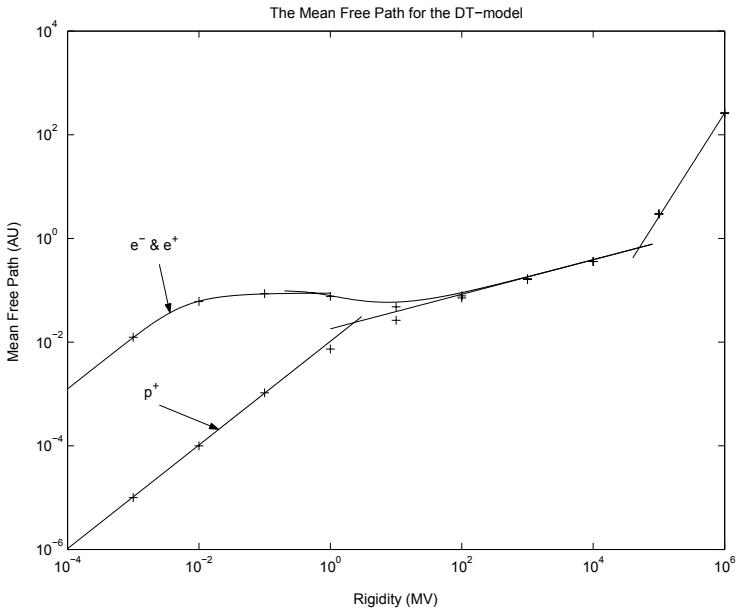

Figure 4.12: Damping turbulence parallel mean free paths for protons and electrons/positrons, as functions of rigidity [*Teufel and Schlickeiser*, 2003]. Crosses indicate numerical solutions, solid lines approximate analytical solutions.

4.4 Characterizing the parallel mean free path: general dependences

The present subsection aims to briefly consider the various dependences of the parallel mean free paths for both the random sweeping and damping models of dynamical turbulence discussed above. Note that for the mean free paths considered here, turbulence quantities such as the variance and correlation scale yielded by the two-component *Oughton et al.* [2011] turbulence transport model for solar minimum conditions have been employed. The use of this turbulence transport model leads to considerably more complicated spatial dependences for these quantities than for those considered in most previous studies of this nature. The parallel mean free paths for protons/antiprotons and for electrons/positrons are initially considered together in this section for the purposes of a general comparison. The dependences of the low-energy electron mean free paths on quantities that do not affect the proton mean free paths will be considered separately in the next subsection. The electron mean free paths to be considered alongside the proton mean free paths in this section are acquired assuming a fit through origin proton gyrofrequency model for the dissipation range onset wavenumber k_D, while for both proton and electron parallel mean free paths a Kolmogorov value is here assumed for the spectral index of the inertial range s. Throughout what follows, the *Parker* [1958] model for the heliospheric magnetic field is used, as is a latitude-dependent solar wind speed, with all large-scale heliospheric quantities being treated as described in Subsection 3.3.1.

Figures 4.13 and 4.14 illustrate the rigidity dependences of the proton and electron/positron parallel mean free paths, for both the random sweeping and damping models of dynamical turbulence at 1 AU and 100 AU in the ecliptic plane and at 50° colatitude respectively, includ-

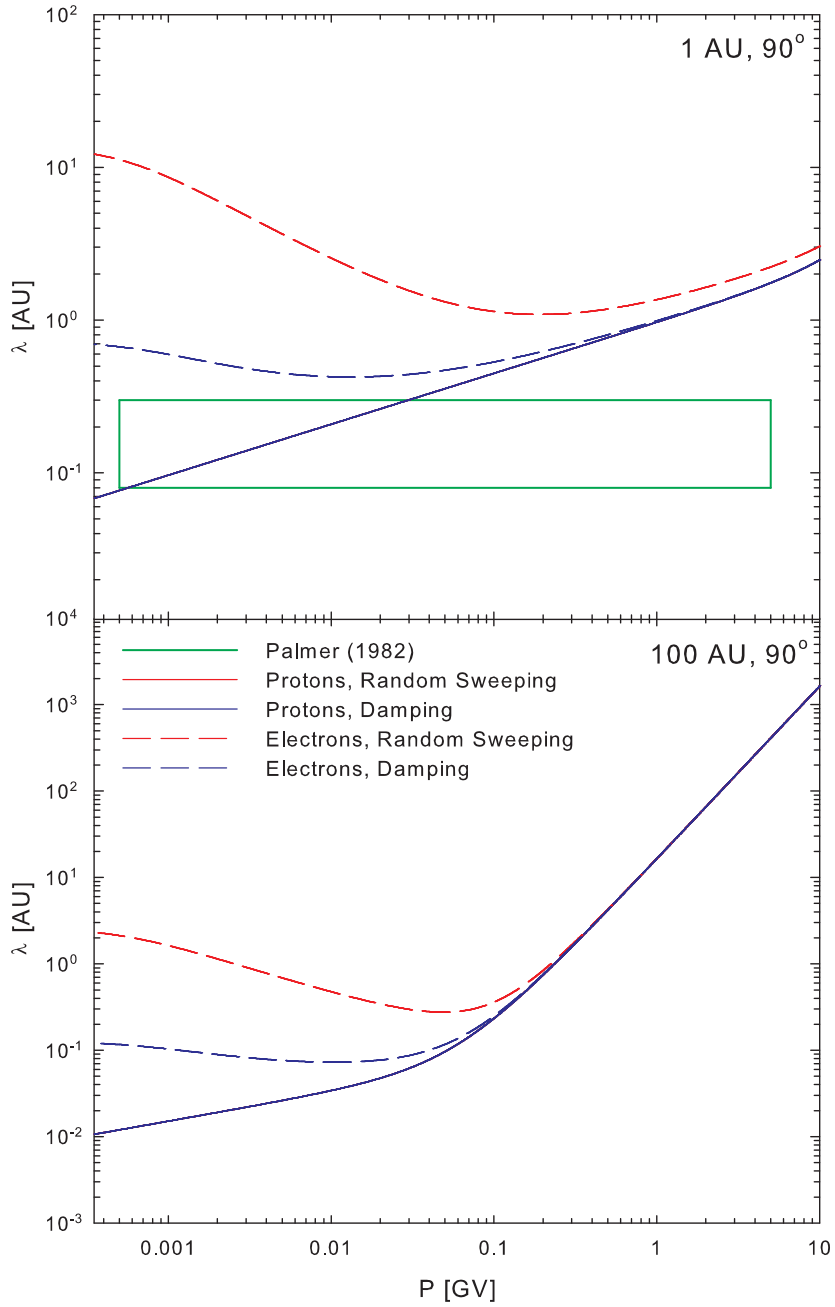

Figure 4.13: Random sweeping and damping turbulence parallel mean free paths for protons/antiprotons and electrons/positrons used in the present study, as functions of rigidity at 1 AU (top panel) and 100 AU (bottom panel) in the ecliptic plane, with the *Palmer* [1982] consensus range.

ing where applicable the *Palmer* [1982] consensus range. At Earth, the proton mean free paths for both the random sweeping and damping turbulence models are identical, with both showing a clear $P^{1/3}$ rigidity dependence. For the electron parallel mean free paths, the differences at low rigidities between those yielded by the assumption of damping *versus* random sweeping turbulence is quite remarkable, and reflect the results of *Teufel and Schlickeiser* [2003] shown in Figures 4.11 and 4.12 where the damping electron mean free path is considerably smaller than that yielded by the random sweeping model. Both electron mean free paths overshoot

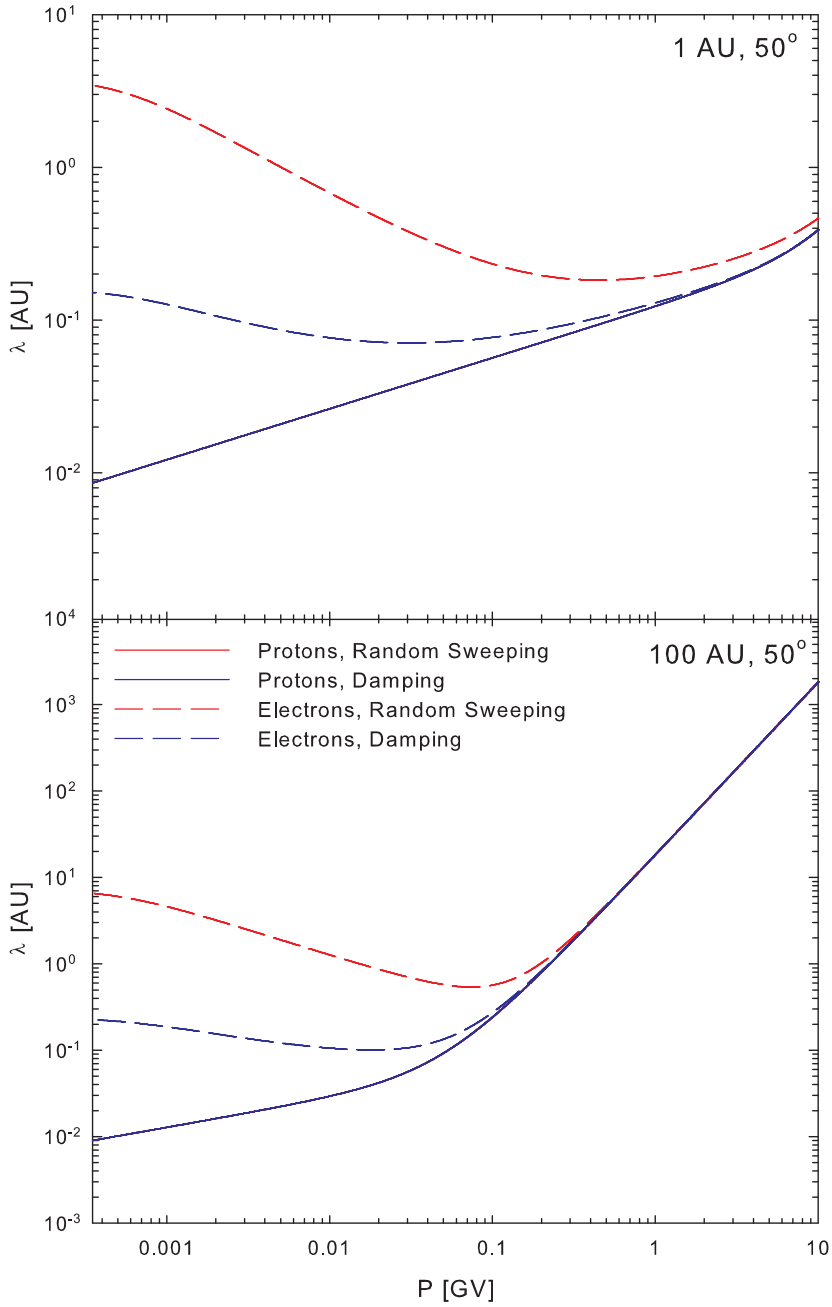

Figure 4.14: Random sweeping and damping turbulence parallel mean free paths for protons/antiprotons and electrons/positrons used in the present study, as functions of rigidity at 1 AU (top panel) and 100 AU (bottom panel) at 50° colatitude.

the Palmer consensus range at all rigidities considered. Note though that the lowest rigidity considered here is such that the flattening in rigidity dependence evident from Figs. 4.11 and 4.12 is not yet seen. The electron parallel mean free paths for both models agree exactly at higher rigidities with the corresponding proton mean free paths, as would be expected. The proton mean free paths at Earth fall reasonably within the Palmer consensus range, but the parallel mean free paths tend to be, especially in the case of the random sweeping electron mean free path, somewhat too large. This is simply a consequence of the choice of solar minimum

turbulence quantities made in the present study.

The bottom panel of Fig. 4.13 illustrates the various parallel mean free paths as functions of rigidity, but at 100 AU in the ecliptic plane. For both proton mean free paths considered, the $P^{1/3}$ dependence that dominated at Earth still persists, but only at the lowest rigidities. Above about 1 GV, both random sweeping and damping turbulence proton and electron mean free paths display a P^2 rigidity dependence, increasing to very large values. This behaviour is a consequence, in part, of the fact that a particle of a given energy would have a correspondingly larger gyroradius here in the outer heliosphere than it would at Earth. Subsequently, particles over a larger range of rigidities would resonate with the energy range fluctuations of the slab power spectrum, leading to the P^2 dependence at even relatively modest rigidities. As at Earth, at higher rigidities the electron mean free paths correspond exactly to the proton mean free paths. At the lowest rigidities the damping turbulence result for electrons is again smaller that that for the random sweeping result.

Figure 4.14 follows similarly to Fig. 4.13, but mean free paths are considered here at 50° colatitude. The rigidity dependences at both 1 and 100 AU are the same as in the ecliptic, for the same reasons. The electron and proton parallel mean free paths at 1 AU, shown in the top panel of Fig. 4.14, are generally smaller at these higher latitudes than those at 1 AU in the ecliptic. This is not surprising given the variance dependence of all these mean free path expressions (Table 4.3), as the slab variance increases with decreasing colatitude. The decrease in parallel mean free path with increased latitude is, however, moderated by the increase in slab correlation scale. This behaviour is in qualitative agreement with the *Erdös and Balogh* [2005] parallel mean free paths calculated from magnetic fluctuations observed by Ulysses, and will be discussed below. At 100 AU the mean free paths at 50° colatitude are larger than those in the ecliptic at this radial distance, although these differences are not very large at the lowest rigidities considered. Again this is due to the behaviour of the turbulence quantities yielded by the *Oughton et al.* [2011] model: from the figures in Subsection 3.4.1 it can be seen that the slab variance yielded by the above model at higher latitudes and at 100 AU is somewhat smaller than that yielded at this radial distance in the ecliptic.

The random sweeping and damping turbulence parallel mean free paths are illustrated as functions of colatitude in Fig. 4.15 at 1 AU and 100 AU, where black lines denote proton mean free paths, and the red line the electron mean free path. It should be noted that at higher rigidities, from Figures 4.13 and 4.14, the proton and electron mean free paths are very similar. Hence the 1 GV line for protons can be treated as that for electrons as well. From Figs. 4.13 and 4.14, however, the 0.1 GV proton mean free path is quite different to that for the electrons. However, in this figure the focus for electrons is on the very low rigidity behaviour of the parallel mean free path. At 1 AU, random sweeping and damping turbulence proton mean free paths are in reasonable qualitative agreement with the solar minimum results of *Erdös and Balogh* [2005] (Fig. 4.4). The damping turbulence proton mean free paths are the same as those yielded by the random sweeping model at 100 AU for all colatitudes. For electrons, at 1 AU the damping

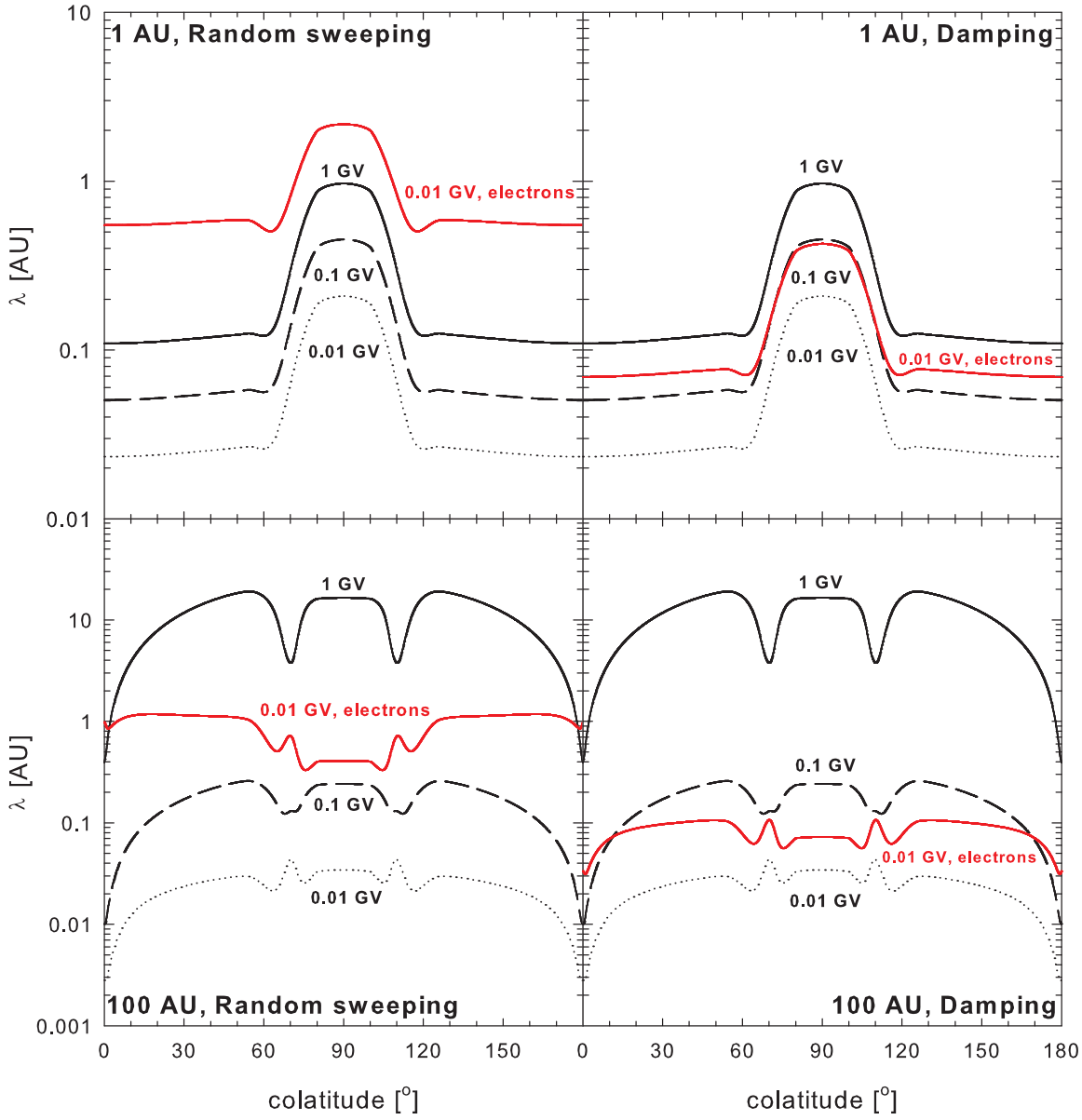

Figure 4.15: Random sweeping and damping turbulence parallel mean free paths for protons/antiprotons and electrons/positrons used in the present study as functions of colatitude at 1 AU (top panels) and 100 AU (bottom panels) for various rigidities. Black lines denote proton, and red lines electron parallel mean free paths.

turbulence mean free path at 0.01 GV is consistently smaller than the random sweeping mean free path at all colatitudes, whilst both electron mean free paths remain consistently larger than their proton counterparts at this rigidity. At 100 AU, the random sweeping model consistently yields a larger parallel mean free path for electrons. The 0.01 GV electron parallel mean free paths for both models of dynamical turbulence are consistently larger than their 0.01 GV proton counterparts.

As functions of colatitude, all parallel mean free paths shown here are quite sensitive to the colatitudinal behaviour of the turbulence quantities yielded by the *Oughton et al.* [2011] model

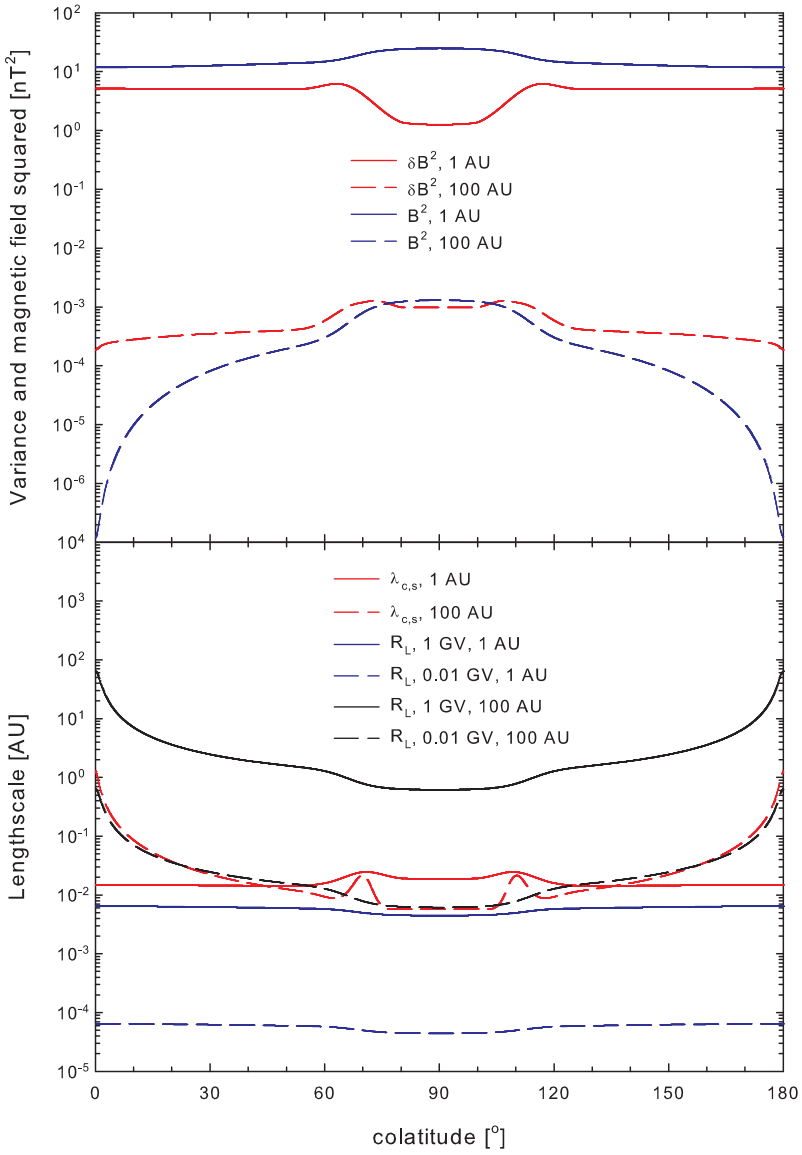

Figure 4.16: Various quantities, as functions of colatitude at 1 AU and 100 AU, that enter into the expressions for the parallel mean free path here used. Note that only slab variances are shown.

(see Subsection 3.4.2), those pertinent to this section being illustrated in Fig. 4.16. All mean free paths shown at 1 AU are larger in the ecliptic plane, with its lower variance values, than toward the poles, displaying slight 'dips' at colatitudes corresponding to the larger variances associated with regions of greater modelled shear effects. At colatitudes smaller (or larger depending on which hemisphere is considered) than these regions, the proton parallel mean free paths for both dynamical turbulence models become almost constant as functions of colatitude, reflecting the behaviour of the slab variance and correlation scales which at this radial distance remain relatively constant as functions of colatitude. The great sensitivity of these mean free path expressions to the behaviour of the variances in particular is simply due to their stronger dependence on this quantity as listed in Table 4.3. The 0.01 GV electron mean free paths at

1 AU over the poles behave in a fashion similar to that of their proton counterparts at this rigidity. The 0.01 GV electron mean free paths at 100 AU, the damping turbulence expressions in particular, show a slight decrease toward the poles. This is due to the fact that the dominant terms at this rigidity are also functions of the dissipation range breakpoint wavenumber k_D, which decreases towards the poles.

In the outer heliosphere the parallel mean free paths tend to be quite large. This is a consequence as noted above of larger particle gyroradii at these distances (shown also in Fig. 4.16), even though the slab variances yielded by the *Oughton et al.* [2011] model are large, which is a consequence of the formation of pickup ions from neutral hydrogen. The decrease in all mean free paths at 100 AU as the polar colatitudes are approached, reflect a steep decrease toward the poles of the Parker HMF magnitude, which effectively counteracts the increase of the slab correlation scale, and hence of the slab turnover scale, toward the poles. At 100 AU only the higher rigidity mean free paths display the 'dips' at intermediate colatitudes corresponding to regions with increased stream-shear effects, while the 0.01 GV mean free paths yielded by both models for protons and electrons display an increase at these colatitudes. This increase reflects the relatively large increase in the slab correlation scale, seen in the solutions of the *Oughton et al.* [2011] model at these colatitudes in the bottom panel of Fig. 4.16. The question naturally arises as to why this increase is not seen for higher rigidity mean free paths, or for the 0.01 GV mean free paths at 1 AU. The answer to this lies in the behaviour of the gyroradius. Fig. 4.16 illustrates how the proton gyroradius, at 100 AU for a rigidity of 1 GV, is significantly larger than the slab correlation scale at all colatitudes. This, however, is not the case for the 0.01 GV gyroradius at colatitudes corresponding to regions of enhanced stream-shear effects. Therefore, at these colatitudes and at lower rigidities, the parallel mean free paths are dominated rather by the behaviour of the correlation scale, as opposed to the usual situation where the effects of this quantity are moderated by the much larger particle gyroradius.

The radial dependences of these mean free paths, illustrated in Fig. 4.17, is also rather more complicated than those considered in previous studies (*e.g. Burger et al.* [2008]), due to the use of the *Oughton et al.* [2011] model as opposed to more *ad hoc* expressions for the spatial variation of turbulence quantities. The ecliptic parallel mean free paths for protons, shown along with those for electrons in the top panels of Fig. 4.17, resemble roughly those reported by *Pei et al.* [2010a] for the pickup-ion driven, single-component *Breech et al.* [2008] turbulence transport model. The ecliptic random sweeping and damping turbulence parallel mean free paths increase steadily with increasing radial distance until $\sim 5 - 6$ AU, reflecting the steady decrease of the slab variance and increase of the slab correlation scale shown in Subsection 3.4.1 (Fig. 3.9). For a few astronomical units beyond this distance, which corresponds roughly to the ionization cavity lengthscale here used, the ecliptic parallel mean free paths decrease somewhat due to the increased variance and decreased correlation scales caused by the ionization of interstellar neutral hydrogen. This downturn, not seen in the results of *Pei et al.* [2010a], is quite brief for the 1 GV parallel mean free paths, but quite significant for the mean free paths

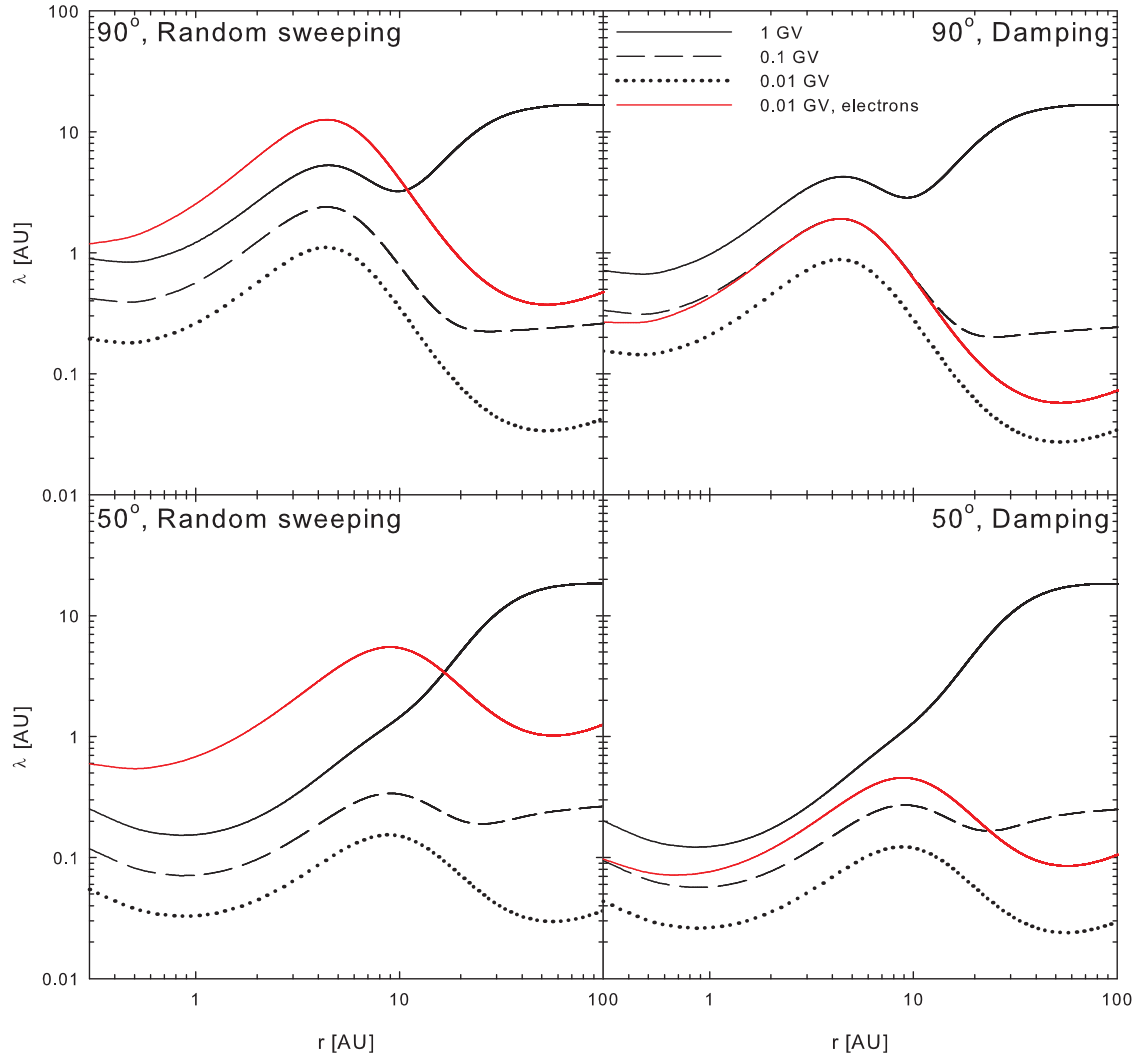

Figure 4.17: Random sweeping and damping turbulence parallel mean free paths for protons/antiprotons and electrons/positrons used in the present study as functions of heliocentric radial distance in the ecliptic plane (top panels) and at 50° colatitude (bottom panels) for various rigidities. Black lines denote proton parallel mean free paths, red lines electron parallel mean free paths.

at the other rigidities shown. After the previously mentioned downturn, all parallel mean free paths again increase with radial distance, as the slab variance remains at a relatively large value, while the correlation scale here becomes dominated by the radially increasing resonant lengthscale λ_{res} at which energy due to the formation of pickup ions enters the slab fluctuation spectrum. At the largest radial distances the parallel mean free paths flatten out, reflecting the radial behaviour of the slab variance.

In the ecliptic, the random sweeping proton parallel mean free paths are the same as those yielded by assuming the damping model of dynamical turbulence, as expected. Damping turbulence electron mean free paths at low rigidities remain consistently smaller than the random sweeping electron mean free paths. The bottom panels of Fig. 4.17 show the various parallel

mean free paths here considered at 50° colatitude as functions of heliocentric radial distance. At lower rigidities the proton and electron parallel mean free paths behave in much the same way as in the ecliptic plane, for the same reasons. At the smallest radial distances (below 1 AU), the steep radial decrease seen for the parallel mean free path employed by *Pei et al.* [2010a] at lower colatitudes is considerably more moderate for both the random sweeping and damping proton parallel mean free paths shown here, a difference that cannot entirely be associated with the different colatitudes considered by *Pei et al.* [2010a] and those shown in Fig. 4.17. Beyond ~ 1 AU, the highest rigidity proton mean free paths at 50° colatitude show an approx. $\sim r^{+1}$ radial dependence, subsequently flattening out, as in the ecliptic plane at the largest radial distances shown. These mean free paths show nothing of the 'dip' in $\lambda_{\parallel}$ seen in the ecliptic results at intermediate radial distances. Both the 1 GV proton mean free paths shown here closely resemble the 0.445 GV proton parallel mean free paths of *Pei et al.* [2010a] at 30° colatitude at intermediate radial distances, differing only at higher radial distances where the *Pei et al.* [2010a] mean free paths continue increasing with radial distance. The lower-rigidity parallel mean free paths illustrated in Fig. 4.17, however, bear little resemblance to the expressions reported by *Pei et al.* [2010a], no doubt due to the differences in turbulence transport models employed. At both colatitudes shown in Fig. 4.17, the 0.01 GV electron mean free paths are quite large, a reflection of the rigidity dependences illustrated earlier, with random sweeping electron mean free paths consistently yielding larger values than their damping turbulence counterparts.

4.5 Characterizing the parallel mean free path: low-rigidity electron mean free paths

This section considers the effects of various models for the dissipation range onset wavenumber k_D proposed by *Leamon et al.* [2000] on the electron mean free paths presented in this study (for more detail on this quantity, see Subsection 2.3.5). The effects of varying the dissipation range spectral index within the observed range of values at Earth reported by *Smith et al.* [2006] are also discussed. The extrapolations throughout the heliosphere of the dissipation range onset wavenumbers k_D yielded by the various *Leamon et al.* [2000] models will be characterized in the next subsection. Note that all other factors, such as the HMF model used, are held to be the same as for the results presented in the previous section.

4.5.1 Dissipation range breakpoint wavenumber

The present study, like those of *Engelbrecht* [2008] and *Engelbrecht and Burger* [2010], aims to model the global behaviour of k_D throughout the heliosphere, utilizing the expressions proposed by *Leamon et al.* [2000] for conditions at Earth, given by Equations 2.40 and 2.41. These,

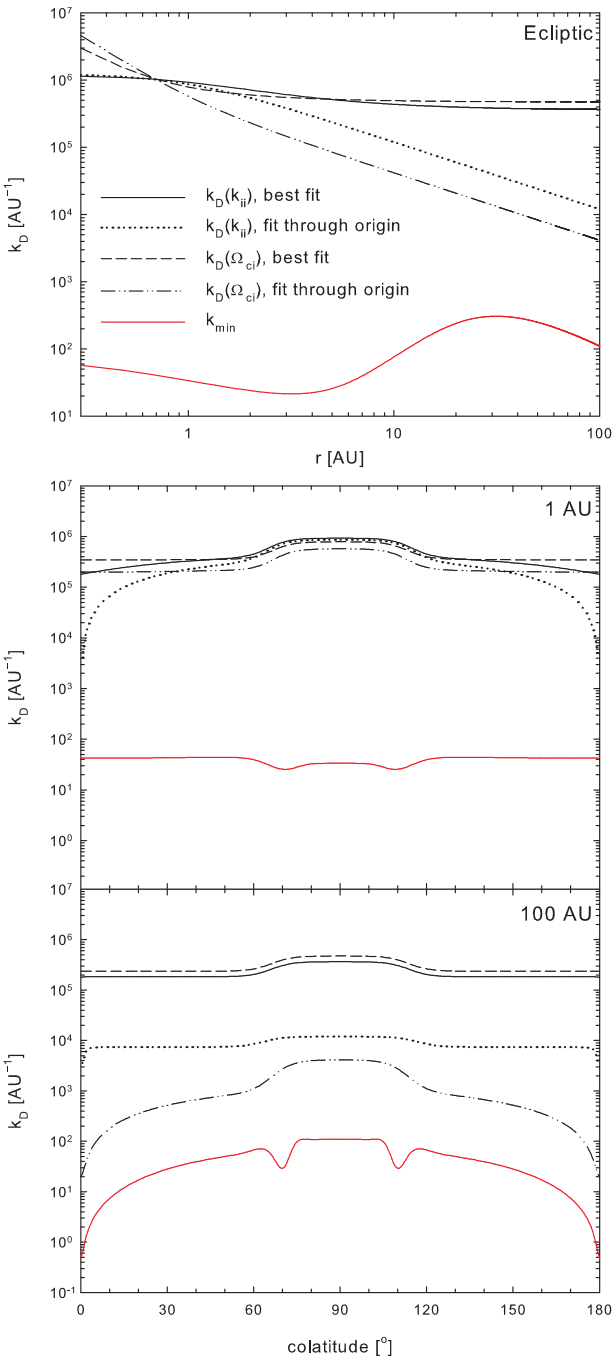

Figure 4.18: Various 1 AU *Leamon et al.* [2000] models used in the present study for the dissipation range onset wavenumber k_D, extrapolated as functions of radial distance in the ecliptic plane (top panel), and as functions of colatitude at 1 AU (middle panel) and 100 AU (bottom panel). The inertial range onset wavenumber k_{min}, calculated using Eq. 2.55 from results yielded by the two-component turbulence transport model of *Oughton et al.* [2011], is also shown. See text for details.

for ease of reference, are again listed here:

$$k_D = \frac{2\pi}{V_{sw}}(a + b\Omega_{ci}), \tag{4.22}$$

where Ω_{ci} denotes the proton gyrofrequency, and

$$k_D = \frac{2\pi}{V_{sw}}(a + \frac{b}{2\pi}k_{ii}V_{sw}), \tag{4.23}$$

with

$$k_{ii} = \frac{2\pi \sin\Psi}{\rho_{ii}} = \frac{2\pi\Omega_{ci}\sin\Psi}{V_A}, \tag{4.24}$$

and Ψ denoting the heliospheric magnetic field's winding angle. The regression constants a and b are listed in Table 2.2. In what follows, the phrase 'fit through origin' denotes the models where a is zero, and 'best fit' those where it is not.

This extrapolation of models reported for conditions at Earth is potentially a risky endeavour in that for widely varying conditions throughout the heliosphere, turbulent and otherwise, such an extrapolation may lead to unphysical modelled spectra, which may in turn lead to trouble with regards to mean free paths derived from it. The present subsection aims to characterize the models for k_D discussed in Subsection 2.3.5 at various regions in the heliosphere, chosen so as to both highlight the spatial dependences of the various models for this quantity as well as to point out potentially unphysical scenarios arising from this extrapolation.

Figure 4.18 illustrates the values yielded by the *Leamon et al.* [2000] best fit and fit through origin ion inertial scale and proton gyrofrequency models for the dissipation range breakpoint wavenumber as functions of radial distance in the ecliptic plane, and as functions of colatitude at 1 AU and 100 AU acquired by assuming a 100 AU heliosphere. Note that a *Parker* [1958] heliospheric magnetic field and a radially constant solar wind speed profile that varies from 400 km/s to 800 km/s from ecliptic to polar latitudes (see Subsection 3.3.1 for more detail and motivation) are assumed. Also shown in Fig. 4.18 are values of the inertial range breakpoint wavenumber k_{min} used in the present study, calculated from the slab turnover scales, using Eq. 2.55, produced by the *Oughton et al.* [2011] two-component turbulence transport model. This is done so as to demonstrate that k_{min} remains smaller than k_D throughout the heliosphere, a condition that ensures a well-defined inertial range on the modelled slab spectrum. If this condition were not met it can lead to problematic scenarios involving the parallel mean free paths used in the present study, as these were derived assuming a well-defined inertial range.

The top panel of Fig. 4.18 shows a clear difference between the best fit and fit through origin models for k_D, with the fit through origin values for both the ion inertial and proton gyrofrequency models decreasing monotonically with increased radial distance throughout most of the heliosphere. This is in contrast to the relatively constant radial profiles displayed by the best fit models. This is simply due to the additional constant factor present in the best fit equations, where parameter a is set to zero. Furthermore, both best fit models yield very similar results in the outer heliosphere, with the ion inertial scale fit through origin model yielding results higher than those of the proton gyrofrequency fit through origin model. When compared to k_{min}, all models yield results well above this quantity, thereby satisfying the condition that $k_D > k_{min}$, at least in the ecliptic plane.

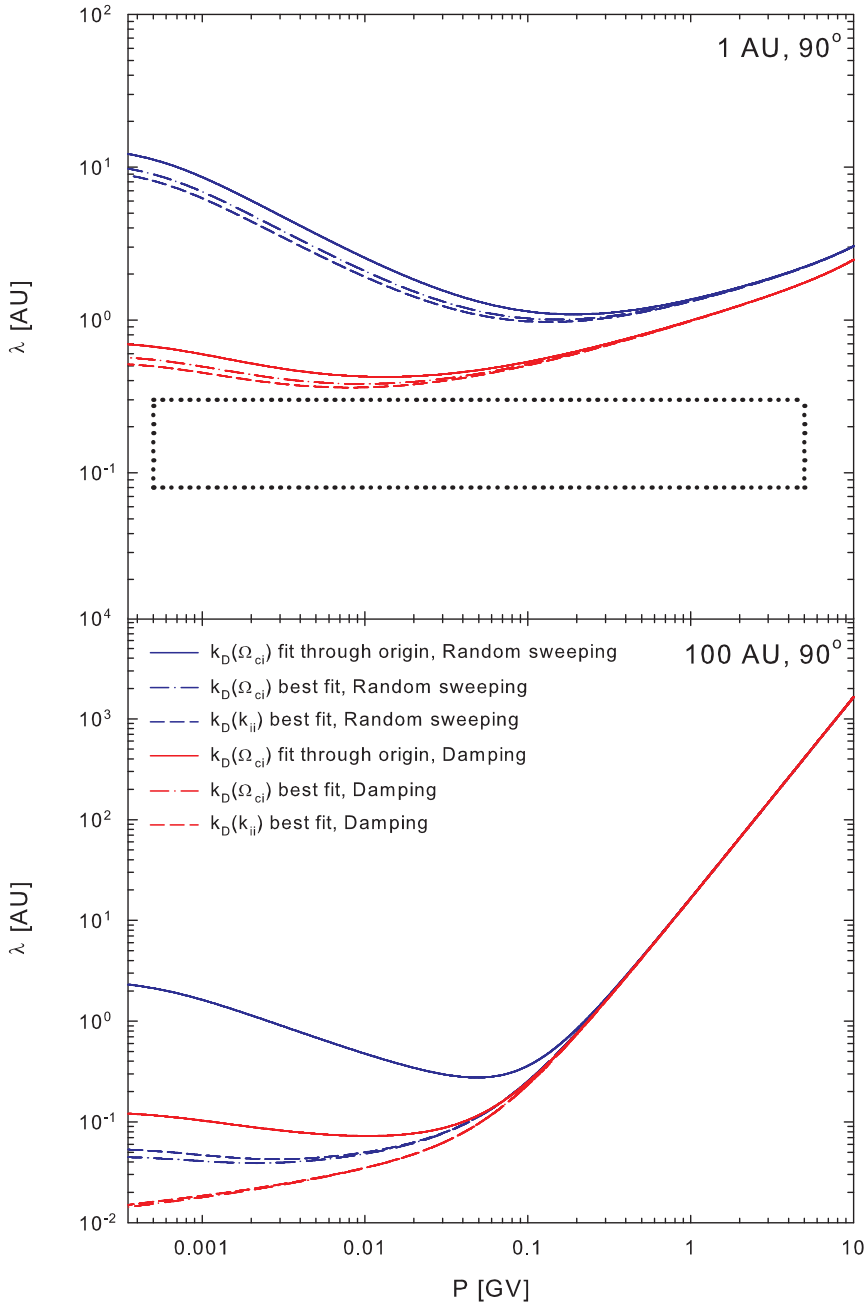

Figure 4.19: Random sweeping (blue lines) and damping turbulence (red lines) electron parallel mean free paths used in the present study as functions of rigidity at 1 AU (top panel) and 100 AU (bottom panel) in the ecliptic plane for various models for the dissipation range breakpoint wavenumber proposed by *Leamon et al.* [2000]. The quantities Ω_{ci} and k_{ii} in brackets denote dissipation breakpoint wavenumbers based on the proton gyrofrequency and ion inertial scale, respectively. Also shown is the *Palmer* [1982] consensus range.

When considered as functions of colatitude in the bottom panels of Fig. 4.18, all models yield results larger in magnitude in the ecliptic than over the poles as expected from Equations 2.40 and 2.41. The best fit models again yield similar results, and for a large range of colatitudes about the ecliptic plane the ordering of values for k_D yielded by these models remains the same as that displayed in the top panel of Fig. 4.18. Over the poles, however, things become

more complicated for both radial distances considered. In this region, the proton gyrofrequency becomes quite small, and directly over the poles, the sine of the heliospheric winding angle becomes zero. The best fit values remain relatively unaffected by this, due again to the constant factor a in Equations 2.40 and 2.41 having a non-zero value. The fit through origin gyrofrequency model, however, yields very small values for k_D, and although this is not clear due to the logarithmic scale of the figure, the fit through origin ion inertial scale model yields a zero result for this quantity directly over the poles. Even though the fit through origin proton gyrofrequency model yields very small values for k_D over the poles, these values remain larger than the illustrated inertial range breakpoint wavenumber, as do those yielded by both best fit models. Due to the fit through origin ion inertial scale model yielding zero values for k_D over the poles, this model will not be considered in subsequent modulation studies here presented, although the use of an alternative model for the heliospheric magnetic field, in conjunction with an alternative definition of the winding angle, can be used to avoid this issue [see, *e.g.*, *Burger et al.*, 2008; *Engelbrecht and Burger*, 2010].

4.5.2 Effect of various models for the dissipation range onset wavenumber and spectral index

The low-energy electron/positron mean free paths, as described by Equations 4.17 and 4.19 for the random sweeping and damping models of dynamical turbulence, are shown as functions of rigidity at 1 AU and 100 AU for the various *Leamon et al.* [2000] models for k_D. At lower rigidities, the random sweeping model yields parallel mean free paths consistently larger than those acquired assuming the damping model of dynamical turbulence, none of which fall within the Palmer consensus range at 1 AU. The random sweeping parallel mean free paths for larger values of k_D are lower at small rigidities (see Fig. 4.18), reflecting the k_D^{s-p} dependence listed in Table 4.3. This behaviour can also be seen in the damping turbulence mean free paths, although the dependence on the magnitude of k_D is not as strong as in the random sweeping case. Mean free paths acquired using the best fit ion inertial and proton gyrofrequency models for k_D tend to be very similar, due to these models yielding very similar values for this quantity, as can be seen in Fig. 4.18. Overall, k_D has a relatively moderate effect on the electron parallel mean free paths at 1 AU, in contrast to their behaviour at 100 AU, where the parallel mean free paths acquired using both best fit models for the dissipation range breakpoint theory are considerably smaller than those acquired assuming the fit through origin gyrofrequency model. This is a consequence of the large decrease in HMF magnitude with increased heliocentric radial distance having a strong, lowering effect on the fit through origin gyrofrequency model. This is an effect that is masked in the best fit models due to the non-zero values of the constant a in Equations 4.22 and 4.22. While the larger random sweeping parallel mean free paths for the best fit k_D models flatten out at the lowest rigidities shown, the lower damping turbulence mean free paths for these models seem not to show the effects of a dissipation range at all, displaying only the $P^{1/3}$ and P^2 rigidity dependences one would expect of proton parallel

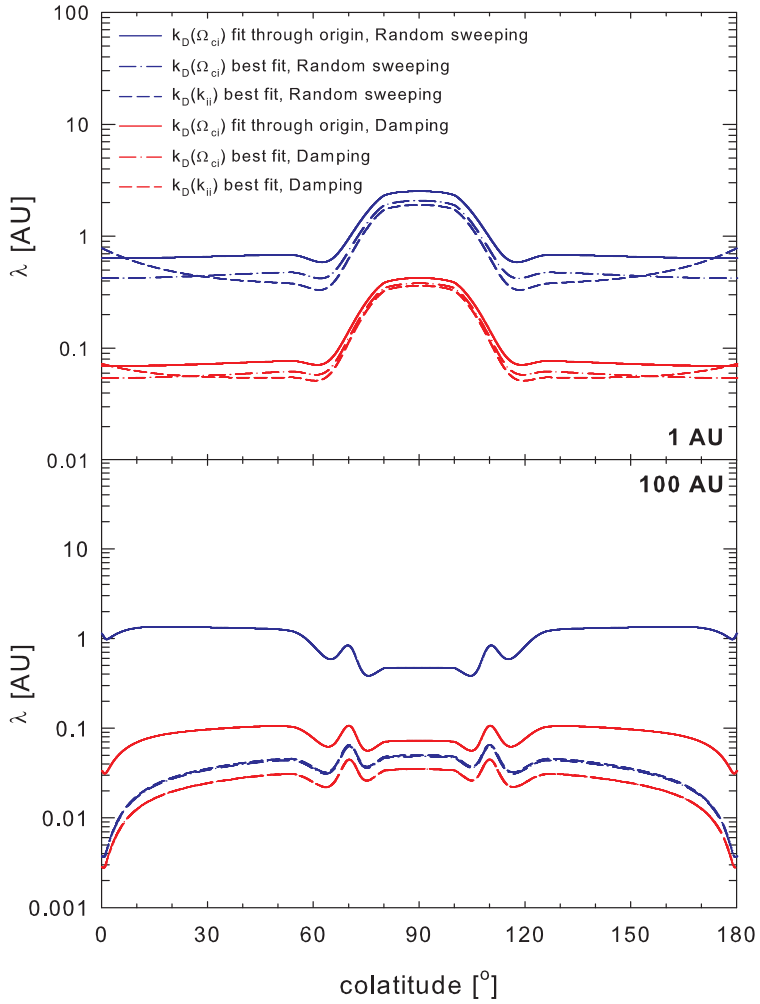

Figure 4.20: Random sweeping (blue lines) and damping turbulence (red lines) 0.01 GV electron parallel mean free paths used in the present study as functions of colatitude at 1 AU (top panels) and 100 AU (bottom panels) for various models for the dissipation range breakpoint wavenumber proposed by *Leamon et al.* [2000]. The quantities Ω_{ci} and k_{ii} in brackets denote dissipation breakpoint wavenumbers based on the proton gyrofrequency and ion inertial scale, respectively.

mean free paths. This again remains a consequence of the larger values for k_D yielded by these models, which act so as to reduce the significance of the dissipation range on the slab spectrum, thereby reducing the action of the dissipation range-dependent terms in Equations 4.17 and 4.19 for the mean free paths acquired from both models of dynamical turbulence.

As functions of colatitude, shown in Fig. 4.20, the 0.01 GV electron mean free paths display the same order of increase with smaller corresponding values for k_D as discussed above, for the same reasons. The general features of these mean free paths as functions of colatitude are discussed in the previous section. Again, the damping turbulence mean free paths are consistently smaller than their random sweeping equivalents, at both 1 AU and 100 AU. The mean free paths yielded by the best fit models for the dissipation range breakpoint wavenumber are very similar over most colatitudes, due to the similarity of the values of k_D yielded by these models. Approaching the heliospheric poles at 1 AU, however, the best fit ion inertial scale

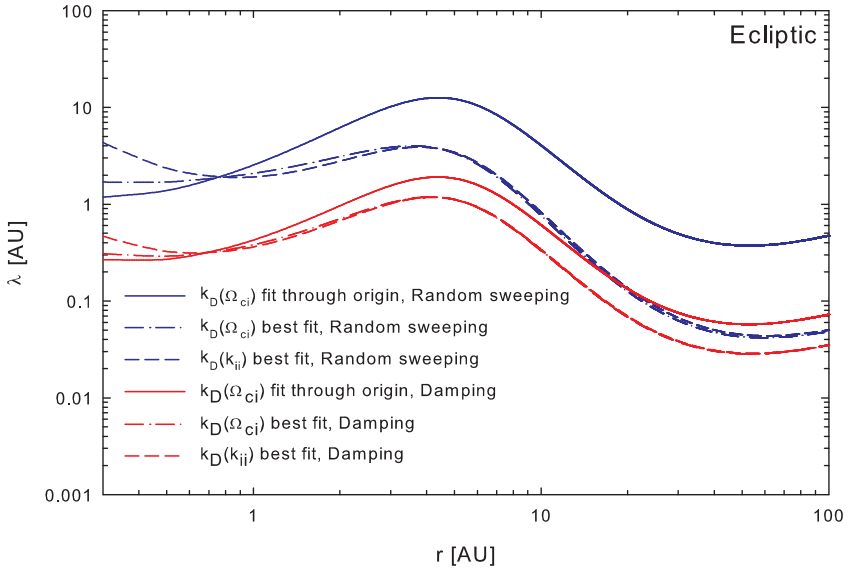

Figure 4.21: Random sweeping (blue lines) and damping turbulence (red lines) 0.01 GV electron parallel mean free paths used in the present study as functions of radial distance in the ecliptic plane for various models for the dissipation range breakpoint wavenumber proposed by *Leamon et al.* [2000].

model mean free path increases somewhat. This is due to the smaller values for k_D that this model yields in this region, shown in Fig. 4.18, as a consequence of the increased Alfvén speed over the poles. At 100 AU, the mean free paths for all models for k_D show a marked decrease towards the poles, with the steepest decrease corresponding to the largest values for k_D. For completeness, the radial dependences of these mean free paths are also shown in Fig. 4.21. The choice of k_D affects the magnitude of the electron mean free paths, for both random sweeping and damping models of dynamical turbulence, in exactly the same way as in the previous cases, with larger values of k_D yielding smaller parallel mean free paths. The best fit models yield very similar radial dependences, which comes as no surprise, as these quantities are both approximately constant in the outer heliosphere, from Fig. 4.18, and yield values very close to one another for the dissipation range breakpoint wavenumber. In the outer heliosphere the markedly different radial dependence seen in Fig. 4.18 of the fit through origin proton gyrofrequency model for k_D does not translate to a vastly different radial dependence for the parallel mean free path acquired from it, when compared to those of the best fit models. Only in the very inner heliosphere, within 1 AU, do these models appear to have a significant effect on the radial dependence of these low-energy electron parallel mean free paths. In Fig. 4.21, it can again clearly be seen that the damping turbulence mean free paths are not as strongly dependent on k_D as are the random sweeping mean free paths, as the difference between the best fit and fit through origin damping turbulence mean free paths is considerably less than for the random sweeping mean free paths.

Smith et al. [2006] reported a value of 2.61 ± 0.96 for the dissipation range spectral index p. Low-energy electron parallel mean free paths are expected to increase in magnitude due to

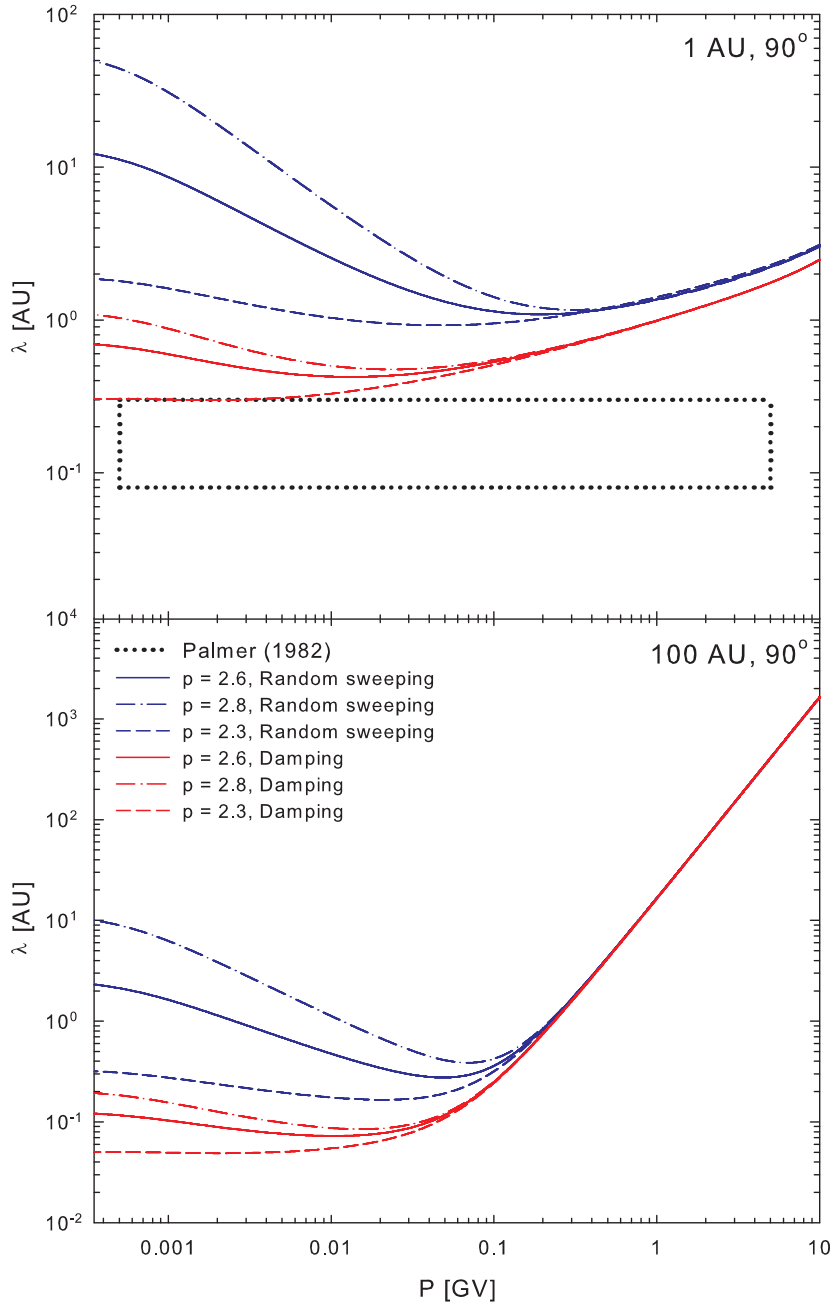

Figure 4.22: Random sweeping (blue lines) and damping turbulence (red lines) electron parallel mean free paths used in the present study, as functions of rigidity at 1 AU (top panel) and 100 AU (bottom panel) in the ecliptic plane, with the *Palmer* [1982] consensus range, for various values of the dissipation range spectral index within the range of values reported by *Smith et al.* [2006]. Note that the mean free paths shown are acquired using the fit through origin proton gyrofrequency model for the dissipation range breakpoint wavenumber.

an increase in this quantity, due to the associated decrease in the level of turbulence at high wavenumbers. That this is indeed the case can be seen in Fig. 4.22, where electron mean free paths, for both the damping and random sweeping models of dynamical turbulence, are shown for various values of p, at 1 AU and at 100 AU in the ecliptic. Note that for these mean free paths the fit through origin proton gyrofrequency model for k_D was employed. Both ran-

dom sweeping and damping electron mean free paths increase when p is increased, and *vice versa*. For the values of p here considered, the damping turbulence mean free paths come close to the Palmer consensus range at 1 AU, with the $p = 2.3$ case actually touching on the upper part of this range, but still remain mostly above it. The random sweeping mean free paths remain much larger than the Palmer consensus range, even for the smallest value of p considered. As for the case of the dissipation range breakpoint wavenumber, the damping turbulence mean free paths appear less sensitive to changes in the dissipation range spectral index than the random sweeping mean free paths for both radial distances shown. Varying p appears only to alter the magnitude of the low-energy electron parallel mean free paths throughout the heliosphere, without affecting their spatial dependences.

4.6 Perpendicular mean free path

The ENLGC theory proposed by *Shalchi* [2006], based on the NLGC formalism of *Matthaeus et al.* [2003], is chosen to describe the perpendicular diffusion coefficients used in the present study, following broadly the approach of *Shalchi et al.* [2004a]. Assuming axisymmetric turbulence, such that $\kappa_\perp = \kappa_{xx} = \kappa_{yy}$, and a total turbulence modal spectrum $G(\mathbf{k})$ (see Section 2.1) such that

$$G(\mathbf{k}) = G^{slab}(k_\parallel)\delta(k_\perp) + G^{2D}(k_\perp)\delta(k_\parallel) \tag{4.25}$$

the perpendicular diffusion coefficient can be expressed as [*Shalchi et al.*, 2004a]

$$\kappa_\perp = \frac{a^2 v^2}{3B_0^2}\int dk_x dk_y dk_z \frac{G(\mathbf{k})}{v/\lambda_\parallel + k_\perp^2\kappa_\perp + k_\parallel^2\kappa_\parallel + \gamma(\mathbf{k})}, \tag{4.26}$$

where v denotes particle velocity, and $\gamma(\mathbf{k})$ a damping function. Magnetostatic 2D turbulence is here assumed, as in *Shalchi et al.* [2004a], and hence the damping function is taken to be zero. This assumption is made so as to acquire relatively tractable solutions requiring relatively little computation. For cases where the assumption of magnetostatic turbulence is not made, consult *Shalchi et al.* [2004c, 2006]. The parameter a^2 is a constant, reported by *Matthaeus et al.* [2003] to have a value of $1/3$, a value motivated by fitting the results yielded by NLGC to numerically simulated perpendicular diffusion coefficients. *Shalchi and Dosch* [2008], however, derive NLGC using the Newton-Lorentz equation without this parameter, and in a comparison of their results with those of *Matthaeus et al.* [2003] suggest that $1 < a^2 < 2$, where $a^2 = 1$ at low to intermediate energies.

In the present study, the 2D modal spectrum discussed in Subsection 2.4.1 is used, repeated here for ease of reference:

$$G_0^{2D}(k_\perp) = \frac{1}{2\pi k_\perp} C_o \lambda_{2D}\delta B_{2D}^2 \begin{cases} (\lambda_{out}k_\perp)^q & \text{for } |k_\perp| < 1/\lambda_{out}; \\ 1 & \text{for } 1/\lambda_{out} \leq |k_\perp| < 1/\lambda_{2D}; \\ (\lambda_{2D}k_\perp)^{-\nu} & \text{for } |k_\perp| \geq 1/\lambda_{2D}, \end{cases} \tag{4.27}$$

where

$$C_0 = \left[\left(1 + \frac{\lambda_{2D}}{\lambda_{out}}\left(\frac{1}{1+q} - 1\right) + \frac{1}{\nu - 1}\right)\right]^{-1}. \tag{4.28}$$

This spectrum displays a turnover below some scale λ_{out} at very low wavenumbers, similar to the 2D spectra proposed by *Matthaeus et al.* [2007], with a flat energy range, and a Kolmogorov ($\nu = 5/3$) inertial range commencing beyond the 2D turnover scale. Taking Equations 4.25 and 4.27 into account, Equation 4.26 becomes

$$\kappa_\perp = \frac{2a^2v^2}{3B_0^2}\left[\int_0^\infty dk \frac{G^{2D}(k)}{v/\lambda_\parallel + k^2\kappa_\perp}\right], \tag{4.29}$$

following the ENLGC approach of *Shalchi* [2006]. Note that although the above integration does not include the slab spectrum, the resulting perpendicular mean free path expression will be affected by the choice of $G^{slab}(k_\parallel)$, by way of its dependence on the parallel mean free path. The above relation can be somewhat simplified, following in part the approach of *Shalchi et al.* [2004a], by taking into account that $\kappa_\perp = v\lambda_\perp/3$. This, after some minor factorization, allows one to eliminate the particle speed v from Eq. 4.29, such that

$$\lambda_\perp = \frac{2a^2}{B_0^2}\left[\lambda_\parallel \int_0^\infty dk_\perp 2\pi k_\perp \frac{G^{2D}(k_\perp)}{1 + \lambda_\parallel\lambda_\perp k_\perp^2/3}\right]. \tag{4.30}$$

Note that the form of the above expression differs somewhat in appearance from the result of *Shalchi et al.* [2004a] due to the present need to keep this expression in terms of general power spectra. Integration of the above expressions yields an equation of the form

$$\lambda_\perp = h_\perp(C_0, \delta B_{2D}^2, \lambda_{out}, \lambda_{2D}, q, \nu, \lambda_\parallel, \lambda_\perp), \tag{4.31}$$

where

$$h_\perp = \frac{2a^2C_0\lambda_{2D}\delta B_{2D}^2}{\lambda_\perp B_o^2}\left[h_{\perp,1} + h_{\perp,2} + h_{\perp,3}\right], \tag{4.32}$$

with

$$h_{\perp,1} = \frac{\lambda_\parallel\lambda_\perp}{(1+q)\lambda_{out}} {}_2F_1(1, \frac{1+q}{2}, \frac{3+q}{2}; \frac{-\lambda_\parallel\lambda_\perp}{3\lambda_{out}^2}), \tag{4.33}$$

$$h_{\perp,2} = \sqrt{3\lambda_\parallel\lambda_\perp}\left[\arctan\left(\frac{\sqrt{3}\lambda_{out}}{\sqrt{\lambda_\parallel\lambda_\perp}}\right) - \arctan\left(\frac{\sqrt{3}\lambda_{2D}}{\sqrt{\lambda_\parallel\lambda_\perp}}\right)\right], \tag{4.34}$$

and

$$h_{\perp,3} = \frac{3\lambda_{2D}}{(1+\nu)} {}_2F_1(1, \frac{1+\nu}{2}, \frac{3+\nu}{2}; \frac{-3\lambda_{2D}^2}{\lambda_\parallel\lambda_\perp}). \tag{4.35}$$

The various hypergeometric equations in the above formulae can be evaluated as discussed in Section 4.3, utilizing Eq. 4.20. For clarity as to the meanings of the multitude of symbols here employed, the reader is referred to Subsections 2.4.1 and 2.4.2.

Shalchi et al. [2010b] derive expressions, using an improved NLGC theory presented by *Shalchi and Dosch* [2008], for the perpendicular mean free path for various energy range wavenumber dependences. These authors, however, do not consider the case where G^{2D} scales as $k_\perp^{-1}$ in the

energy range. Following the approach of *Matthaeus et al.* [2007], such a 2D modal spectrum can be defined as (see Subsection 2.4.1)

$$G_{-1}^{2D}(k_\perp) = \frac{1}{2\pi k_\perp} C_{-1}\lambda_{2D}\delta B_{2D}^2 \begin{cases} \frac{\lambda_{out}}{\lambda_{2D}}(\lambda_{out}k_\perp)^q & \text{for } |k_\perp| < 1/\lambda_{out}; \\ (\lambda_{2D}k_\perp)^{-1} & \text{for } 1/\lambda_{out} \leq |k_\perp| < 1/\lambda_{2D}; \\ (\lambda_{2D}k_\perp)^{-\nu} & \text{for } |k_\perp| \geq 1/\lambda_{2D}. \end{cases}, \quad (4.36)$$

where

$$C_{-1} = \left[\left(\ln\left(\frac{\lambda_{out}}{\lambda_{2D}}\right) + \frac{1}{1+q} + \frac{1}{\nu-1}\right)\right]^{-1}. \quad (4.37)$$

Using this expression in Eq. 4.30 yields

$$\lambda_{\perp,-1} = h_{\perp,-1}(C_{-1}, \delta B_{2D}^2, \lambda_{out}, \lambda_{2D}, q, \nu, \lambda_\parallel, \lambda_\perp), \quad (4.38)$$

where

$$h_{\perp,-1} = \frac{C_{-1}\lambda_{2D}\delta B_{2D}^2}{\lambda_\perp}\left[h_{\perp,-1,1} + h_{\perp,-1,2} + h_{\perp,-1,3}\right], \quad (4.39)$$

with

$$h_{\perp,-1,1} = \frac{\lambda_\parallel\lambda_\perp}{(1+q)\lambda_{2D}} {}_2F_1(1, \frac{1+q}{2}, \frac{3+q}{2}; \frac{-\lambda_\parallel\lambda_\perp}{3\lambda_{out}^2}), \quad (4.40)$$

$$h_{\perp,-1,2} = \frac{1}{2}\lambda_\parallel\lambda_\perp \ln\left[\frac{3\lambda_{out}^2 + \lambda_\parallel\lambda_\perp}{3\lambda_{2D}^2 + \lambda_\parallel\lambda_\perp}\right], \quad (4.41)$$

and

$$h_{\perp,-1,3} = \frac{3\lambda_{2D}}{(1+\nu)} {}_2F_1(1, \frac{1+\nu}{2}, \frac{3+\nu}{2}; \frac{-3\lambda_{2D}^2}{\lambda_\parallel\lambda_\perp}). \quad (4.42)$$

This latter mean free path is included in this study for the sake of general interest only, and its effects on cosmic-ray modulation will not be considered in the chapters to follow.

The perpendicular mean free path described by Eq. 4.31 is a highly non-linear expression, and will be solved using an iterative numerical technique. In the present study, the approximate analytical solution derived by *Shalchi et al.* [2004a], as presented by *Burger et al.* [2008] for a general ratio of slab to 2D variance, is used to provide seed values for such an evaluation. This expression, given by

$$\lambda_\perp \approx \left[\frac{2\nu-1}{4\nu} a^2 F_2(\nu)\lambda_{2D}\sqrt{3}\frac{\delta B_{2D}^2}{B_o^2}\right]^{2/3} \lambda_\parallel^{1/3}, \quad (4.43)$$

with $F_2(\nu) = 2\pi C(\nu)F_1(\nu)$, $F_1(\nu) = 2\nu/(2\nu-1)$ and $C(\nu) = (1/2\sqrt{\pi})[\Gamma(\nu)/\Gamma(\nu-1/2)]$, is a valid approximation under the ENLGC formalism [*Shalchi*, 2006]. The following section will characterize Eq. 4.31 throughout the heliosphere, as has been done for the parallel mean free paths, using the results yielded by the *Oughton et al.* [2011] turbulence transport model for the various turbulence quantities it depends upon.

4.7 Characterizing the perpendicular mean free path

The ENLGC perpendicular mean free path described by Eq. 4.31 contains one important, essentially free parameter, the 2D outerscale λ_{out}, for which no direct observations exist. This

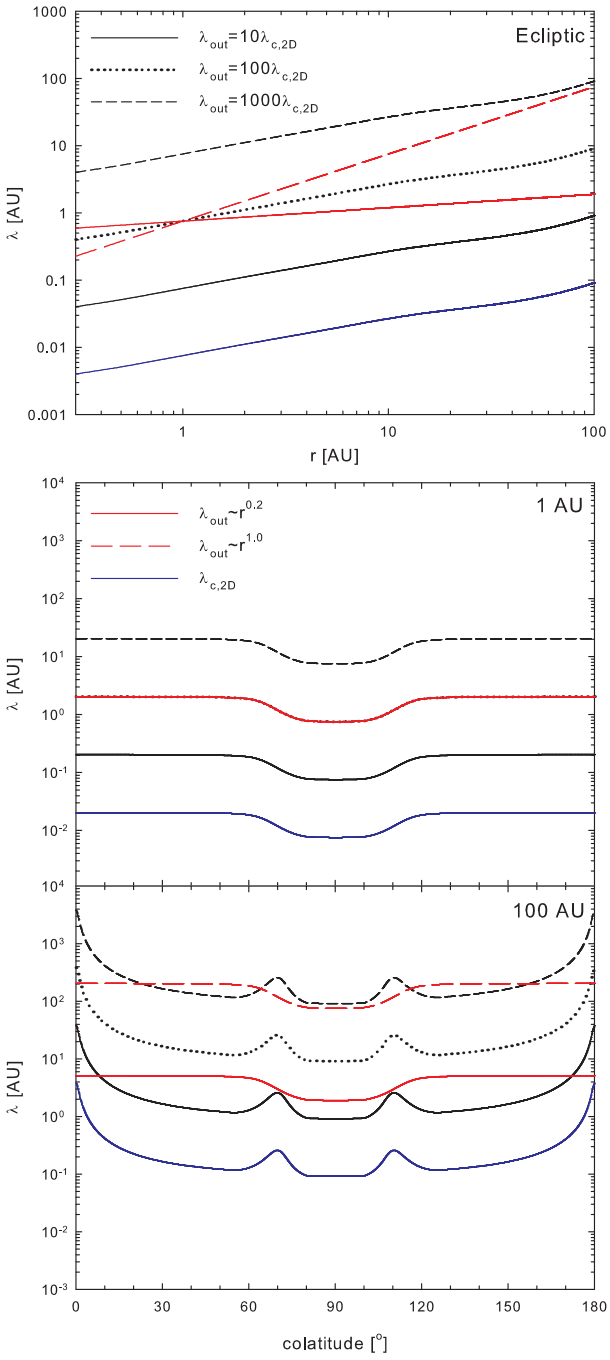

Figure 4.23: Various *ad hoc* expressions used in the present study for the 2D outer scale λ_{out}, as functions of radial distance in the ecliptic plane (top panel), and as functions of colatitude at 1 AU (middle panel) and 100 AU (bottom panel). The 2D correlation scales yielded by the *Oughton et al.* [2011] turbulence transport model used in the calculation of these outerscales is also shown.

being the case, in the present section the perpendicular mean free path will be characterized on the basis of very simple spatial dependences for this quantity, such that

$$\lambda_{out} = k\lambda_{c,2D} \tag{4.44}$$

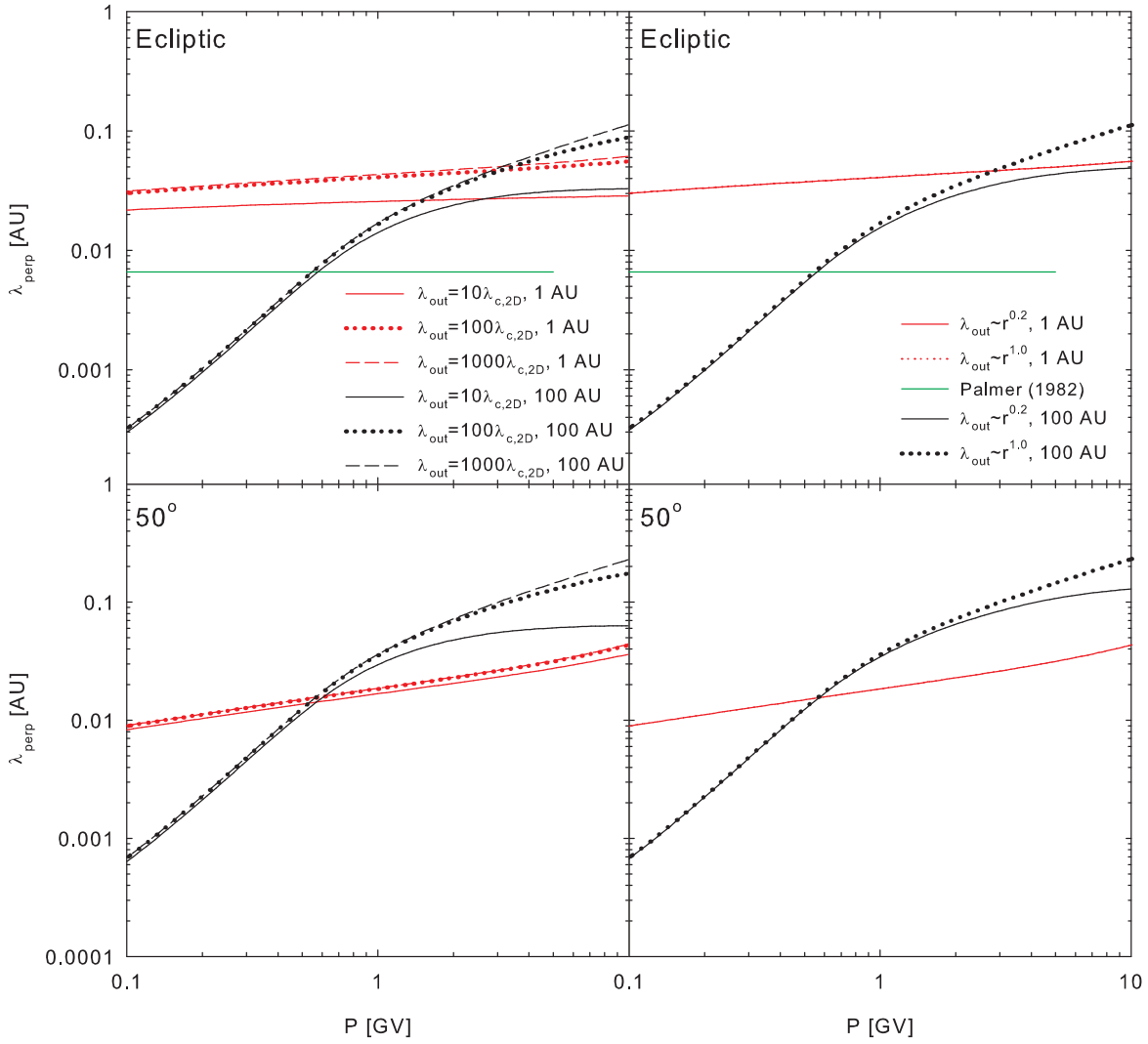

Figure 4.24: Proton ENLGC perpendicular mean free paths as functions of rigidity in the ecliptic plane and at $50°$ colatitude, for 2D outer scales as described by Equations 4.44 (left panels) and 4.45 (right panels) at Earth (red lines) and at 100 AU (black lines). Note that the perpendicular mean free paths shown are acquired using proton parallel mean free paths derived using the random sweeping model of dynamical turbulence. The *Palmer* [1982] consensus range is denoted by the green lines, where relevant.

where $\lambda_{c,2D}$ is the 2D correlation scale, and k is a constant taken to assume values of 10, 100, and 1000, so as to accentuate the effect the magnitude of this quantity may have on the perpendicular mean free path expressions presented in the previous section. To investigate the effects of other radial dependences of λ_{out} on the perpendicular mean free paths, expressions of the form

$$\lambda_{out} = 100\lambda_{c,2D}(1\text{ AU}, \theta)\left(\frac{r}{r_e}\right)^{\varrho} \tag{4.45}$$

with ϱ chosen to be 0.2 and 1.0, are used. The value of Eq. 4.45 at 1 AU is chosen so that the outerscale never assumes values less than or equal to the 2D turnover scale for the radial dependences considered, ensuring a well-defined energy range on the 2D power spectrum

implicit to the use of the *Oughton et al.* [2011] model. These various expressions for the 2D outerscale are shown along with the 2D correlation scale in Fig. 4.23, as functions of radial distance in the ecliptic plane, and as functions of colatitude at 1 AU and 100 AU. From this figure it is clear that all forms chosen for the 2D outerscale remain well above the 2D correlation scale. At 100 AU in the polar regions, the forms $\lambda_{out} = 100\lambda_{c,2D}$ and $\lambda_{out} = 1000\lambda_{c,2D}$ yield results considerably larger than the 100 AU heliosphere assumed in this study. These large values may constitute unphysical choices for λ_{out}, but are nevertheless considered in this study so as to provide some indication of the effect extreme choices for this quantity may have on, *e.g.*, the perpendicular mean free path. Both the $\sim r^{0.2}$ and $\sim r^{1.0}$ models yield the same latitudinal profiles at 1 AU, due to the method of normalisation employed in Eq. 4.45, and remain bounded by the $\lambda_{out} = 10\lambda_{c,2D}$ and $\lambda_{out} = 1000\lambda_{c,2D}$ outerscales as functions of radial distance.

The turbulence quantities that enter into Eq. 4.31 have all been modelled using the two-component turbulence transport model of *Oughton et al.* [2011] described in the previous chapter, assuming a Kolmogorov inertial range spectral index. The parallel mean free paths that enter into this perpendicular mean free path expression are the random sweeping QLT mean free paths of *Teufel and Schlickeiser* [2003], discussed in Sections 4.3 and 4.4. The damping turbulence mean free paths are here omitted, as for protons they are not greatly different to the random sweeping results. The large-scale heliospheric quantities, such as the solar wind profile, have been modelled exactly as described in Subsection 3.3.1. All results are acquired using a Parker heliospheric magnetic field model. Furthermore, electron perpendicular mean free paths are acquired assuming parallel mean free paths where the *Leamon et al.* [2000] fit through origin proton gyrofrequency model for the slab spectrum dissipation range breakpoint wavenumber, and a dissipation range spectral index of $p = 2.6$ [*Smith et al.*, 2006], are employed. The quantity a^2 is here taken to assume a value of $1/3$, following *Matthaeus et al.* [2003]. As increasing/decreasing this constant only increases/decreases the perpendicular mean free path as a whole without affecting any of its dependences, $\lambda_\perp$ will not be here characterized as a function of a^2.

Figure 4.24 shows the rigidity dependences of the proton perpendicular mean free paths in the ecliptic plane and 50° colatitude, at Earth and at 100 AU. All perpendicular mean free paths at 1 AU display a relatively flat rigidity dependence which is not greatly affected by the choice of outerscale. The choice of λ_{out}, however, does affect the magnitude of the resulting perpendicular mean free path in that larger values for this quantity yield larger values for $\lambda_\perp$. This increase in $\lambda_\perp$ for larger outerscales does not continue indefinitely, as the values yielded by the choices of $\lambda_{out} = 100\lambda_{c,2D}$ and $\lambda_{out} = 1000\lambda_{c,2D}$ are almost identical, clearly approaching a limiting value. At 1 AU in the ecliptic and at 50° colatitude, the perpendicular mean free paths acquired assuming $\lambda_{out} \sim r^{\varrho}$ are identical, due to the fact that these choices for the 2D outerscale are normalised to the same values at 1 AU for all colatitudes.

All of the perpendicular mean free paths shown at Earth remain well above the *Palmer* [1982]

consensus range. The 1 AU ecliptic perpendicular mean free paths shown are very similar to those presented by *Pei et al.* [2010a], differing in magnitude partly due to the different turbulence transport model employed by those authors. The scenario presented by Fig. 4.24 becomes somewhat more complicated when perpendicular mean free paths at 100 AU are considered. At the lowest rigidities, perpendicular mean free paths are very small, due to the very small 2D variances yielded by the *Oughton et al.* [2011] model at these large radial distances, and remain relatively unaffected by the choice of outerscale. The 100 AU perpendicular mean free paths show an approximately P^2 rigidity dependence below ~ 1 GV, above which rigidity they either flatten out (for case where $\lambda_{out} = 10\lambda_{c,2D}$) or display a $\sim P^{0.7}$ rigidity dependence (for the larger choices of 2D outerscale). This can be understood in terms of the analysis *Shalchi et al.* [2004a] did of the NLGC perpendicular mean free paths they derived. These authors showed that, when $\lambda_{\perp}\lambda_{\parallel} \ll 3\lambda_{2D}^2$, their perpendicular mean free path would be proportional to the parallel mean free path. When $\lambda_{\perp}\lambda_{\parallel} \gg 3\lambda_{2D}^2$, they showed that $\lambda_{\perp} \sim \lambda_{\parallel}^{1/3}$. The parallel mean free path used in this study displays a P^2 dependence for most of the rigidities here considered at 100 AU, a rigidity dependence reflected in that of the ENLGC perpendicular mean free paths, below ~ 1 GV, shown in Fig. 4.24. The 1 AU perpendicular mean free paths shown in the same figure do not show a P^2 rigidity dependence, scaling rather as $\sim P^{0.1}$. This is simply due to the fact that, as modelled in this study, the quantity $3\lambda_{2D}^2$ is considerably smaller at 1 AU than it is at 100 AU, such that the condition $\lambda_{\perp}\lambda_{\parallel} \ll 3\lambda_{2D}^2$ is not satisfied at Earth. At 1 AU, however, and above ~ 1 GV at 100 AU, the condition $\lambda_{\perp}\lambda_{\parallel} \gg 3\lambda_{2D}^2$ is satisfied, leading to the rigidity dependences shown in Fig. 4.24, in line with a $\lambda_{\perp} \sim \lambda_{\parallel}^{1/3}$ dependency. The 100 AU solutions where $\lambda_{out} \sim r^{\varrho}$ display a similar behaviour at low rigidities, deviating from this at higher rigidities due to the reasons outlined above.

Perpendicular mean free paths with damping parallel mean free paths as inputs, although not shown here, are moderately larger at 100 AU than those acquired using random sweeping parallel mean free paths, reflecting the behaviour of these parallel mean free paths at larger radial distances discussed in Section 4.4.

The corresponding electron perpendicular mean free paths, acquired by employing the electron parallel mean free path expressions discussed in Section 4.3, are illustrated in Fig. 4.25 for a larger rigidity range than for the protons so as to clearly show the effects of the larger parallel mean free paths at these rigidities. For the purposes of brevity, only perpendicular mean free paths acquired assuming random sweeping electron parallel mean free paths will be shown, as those acquired using damping turbulence parallel mean free paths are quite similar. At higher rigidities, these perpendicular mean free paths can be seen to be equal to those for the protons shown in Fig. 4.24, and as such the discussion here will be limited to rigidities below 0.1 GV. All electron perpendicular mean free paths show a slight to moderate upturn with decreasing rigidity, due to the corresponding low-rigidity upturn in the electron parallel mean free paths, and are somewhat above the illustrated *Palmer* [1982] consensus range. Here, as for the 1 AU proton perpendicular mean free paths, the largest outerscale chosen leads to

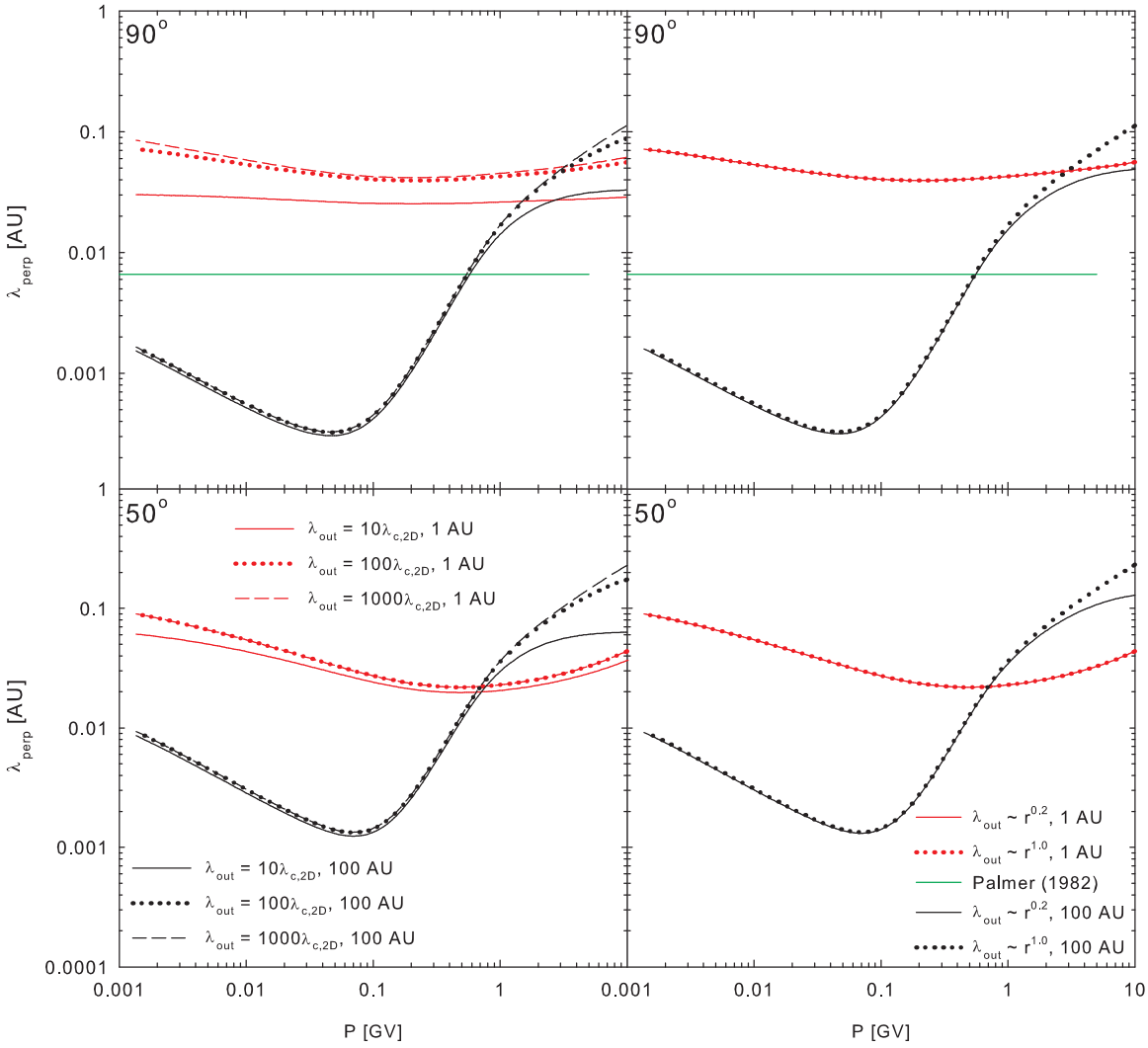

Figure 4.25: Electron ENLGC perpendicular mean free paths as functions of rigidity in the ecliptic plane and at $50°$ colatitude, for 2D outer scales as described by Equations 4.44 (left panels) and 4.45 (right panels), at Earth, and at 100 AU. Note that the perpendicular mean free paths here shown are acquired using electron parallel mean free paths derived using the random sweeping model of dynamical turbulence. The *Palmer* [1982] consensus range is denoted by the green lines, where applicable.

the largest values for $\lambda_{\perp}$, while the larger values for λ_{out} yield results at 1 AU for the perpendicular mean free path that are virtually identical. The 100 AU results increase with decreasing rigidity at the lowest rigidities for both colatitudes considered, again due to the action of the electron parallel mean free paths, and show very little dependence on the value chosen for the 2D outerscale. Varying the radial dependence of the 2D outerscale does not have an effect on the perpendicular mean free paths at the lowest rigidities.

Due to the similarity of both proton and electron perpendicular mean free paths when the 2D outerscale is assumed to be 100 and 1000 times the 2D correlation scale, when the latitude dependence of the perpendicular mean free paths is discussed only the cases where $\lambda_{out} =$

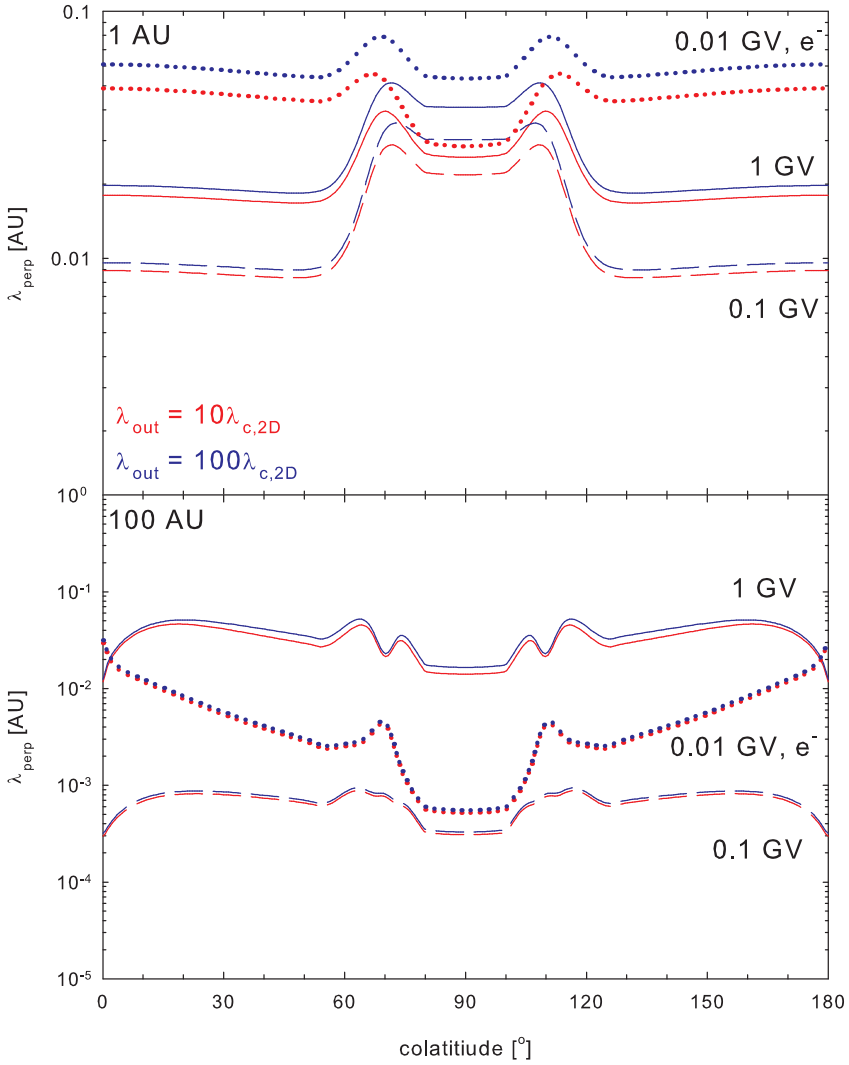

Figure 4.26: Electron/proton ENLGC perpendicular mean free paths at 1 GV (solid lines) and 0.1 GV (dashed lines), and electron perpendicular mean free paths at 0.01 GV (dotted lines) as functions of colatitude for 2D outer scales $\lambda_{out} = k\lambda_{2D}$, where k is 10 and 100, at 1 AU (top panel) and at 100 AU (bottom panel). Note that these perpendicular mean free paths are acquired using parallel mean free paths derived assuming the random sweeping model of dynamical turbulence.

$10\lambda_{c,2D}$ and $\lambda_{out} = 100\lambda_{c,2D}$ will be considered. Also, due to the similarity of the $\lambda_{out} \sim r^{\varrho}$ solutions to those corresponding to $\lambda_{out} = 100\lambda_{c,2D}$, the former perpendicular mean free paths will not be shown.

Figure 4.26 shows the proton/electron perpendicular mean free paths for rigidities of 1 GV (solid lines) and 0.1 GV (dashed lines), and the electron perpendicular mean free path at 0.01 GV (dotted lines) as functions of colatitude at 1 AU and at 100 AU, for random sweeping parallel mean free paths. At 1 AU, the electron mean free paths at higher rigidities are almost identical to the proton perpendicular mean free paths shown in Fig. 4.24, mimicking in this sense the behaviour of the corresponding parallel mean free paths illustrated in Fig. 4.15.

These perpendicular mean free paths follow the latitudinal profile of the 2D variance yielded by the *Oughton et al.* [2011] model, with larger values in the ecliptic than over the poles, and two 'bumps' corresponding to the enhanced turbulence present in regions of greater modelled stream-shear effects. Here, as seen above, larger values of the 2D outerscale lead to larger perpendicular mean free paths. The 0.01 GV electron perpendicular mean free paths also follow the latitudinal profile of the 2D variance, but increase slightly towards the poles due to the influence of the decreasing fit through origin values for the dissipation range breakpoint wavenumber at these latitudes, which acts so as to increase the electron parallel mean free paths as discussed in Section 4.5. As to be expected from the rigidity dependence of the electron perpendicular mean free paths shown in Fig. 4.26, the 0.01 GV electron perpendicular mean free paths are larger than their 0.1 GV counterparts at 1 AU.

At 100 AU, the 1 GV and 0.1 GV ecliptic perpendicular mean free paths are generally smaller than those at higher latitudes, with significant 'bumps' again due to the greater variances yielded by the *Oughton et al.* [2011] model in regions of enhanced stream-shear effects. Over the poles the 1 GV and 0.1 GV perpendicular mean free paths decrease somewhat, due to the concurrent, steep decrease at these colatitudes seen for the parallel mean free paths in Fig. 4.15, and discussed in Section 4.4. The 0.01 GV electron perpendicular mean free path is at 100 AU larger than the 0.1 GV mean free paths, again reflecting the behaviour of the electron parallel mean free paths at this radial distance.

Lastly, it must be noted that the latitudinal dependences of the perpendicular mean free paths presented here at higher radial distances bear a superficial resemblance to the perpendicular mean free path expressions employed in previous modulation studies, such as those performed by *Ferreira et al.* [2001a] and *Ferreira et al.* [2001b] in that the perpendicular mean free paths at higher latitudes are higher than those in the ecliptic. Contrary to the approach of *Ferreira et al.* [2001a] and *Ferreira et al.* [2001b], however, the latitudinal variation of the perpendicular mean free paths used in this study is the result of a self-consistent, *ab initio* application of the results yielded by the *Oughton et al.* [2011] turbulence transport model, and as such shows a marked radial and rigidity dependence not seen in the previous *ad hoc* approaches. This is illustrated in Fig. 4.26, where 1 GV perpendicular mean free paths in the ecliptic, at 1 AU, are larger than those at higher latitudes. It is encouraging, however, to observe that the use of a turbulence transport model such as that employed here can in a very natural way yield perpendicular diffusion coefficients that vary with latitude in such a way, as larger values of the perpendicular mean free path at high latitudes than in the ecliptic have been shown by some modulation studies [see, *e.g.*, *Ferreira*, 2002] to be a necessary ingredient to allow for good agreement between simulated cosmic-ray intensities and various cosmic-ray observations.

The ecliptic radial dependences of the perpendicular mean free paths are shown in Fig. 4.27. All perpendicular mean free paths show a steady increase with radial distance out to ~ 4 AU, reflecting the increase in both the 2D correlation scale and parallel mean free path within this distance. Beyond this distance, however, all perpendicular mean free paths show a decrease

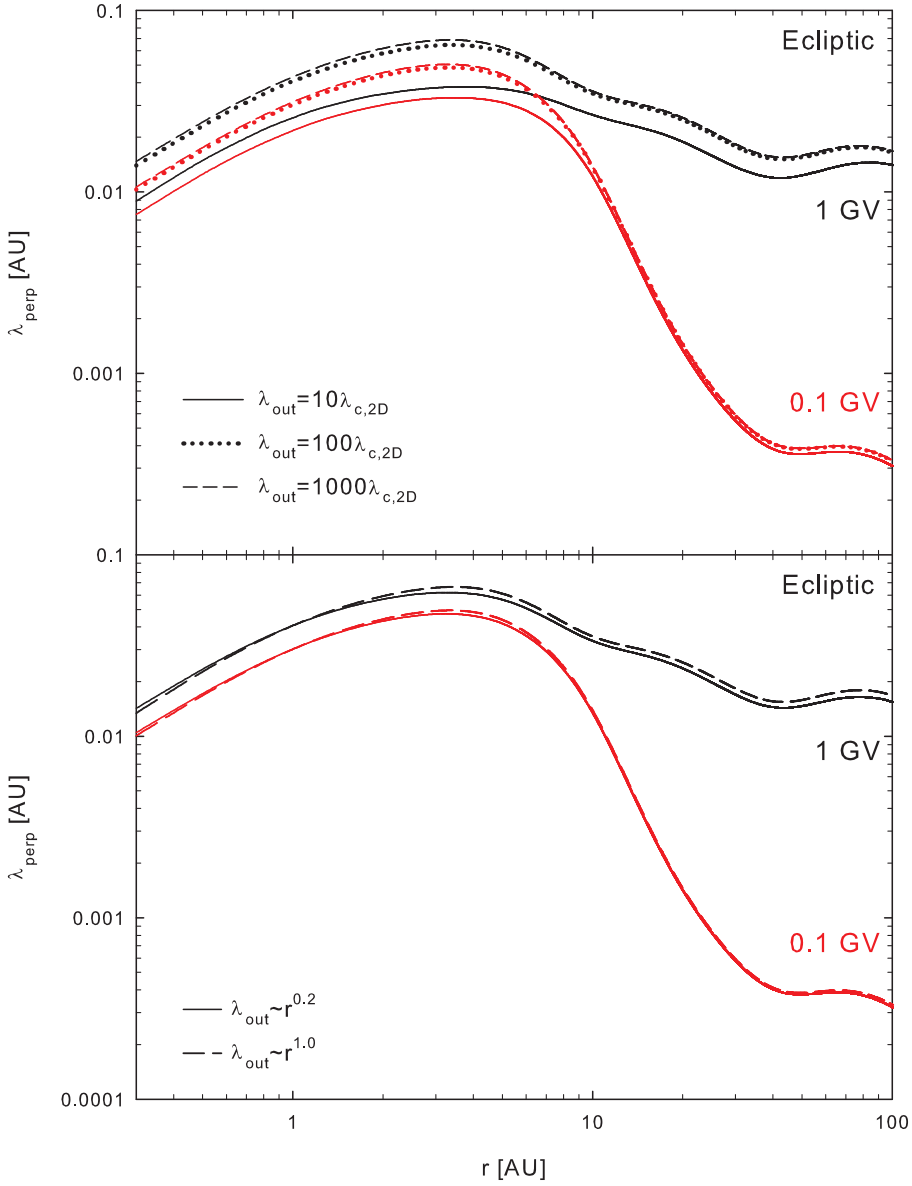

Figure 4.27: Proton ENLGC perpendicular mean free paths at 1 GV (black lines) and 0.1 GV (red lines) as functions of radial distance in the ecliptic plane for 2D outer scales that scale as $\lambda_{out} = k\lambda_{2D}$, where k is 10, 100 and 1000 (top panel) and for 2D outer scales chosen so that $\lambda_{out} \sim r^{\varrho}$, where ϱ is 1.0 and 0.2. Perpendicular mean free paths are acquired using parallel mean free paths derived assuming the random sweeping model of dynamical turbulence.

with radial distance which becomes steeper at lower rigidities, reflecting for the 0.1 GV perpendicular mean free paths, the behaviour of the 2D variances yielded by the *Oughton et al.* [2011] model. The flatter radial dependence of the 1 GV perpendicular mean free paths, however, reflects the behaviour of the larger parallel mean free paths shown in Fig. 4.17. The choice of 2D outerscale appears to have a more significant effect for solutions in the inner heliosphere, and for those corresponding to higher rigidities. The solutions shown in Fig. 4.27 are qualitatively similar to those presented by *Pei et al.* [2010a] at lower radial distances, although in the outer heliosphere the *Pei et al.* [2010a] solutions continue increasing, while the perpendicular mean

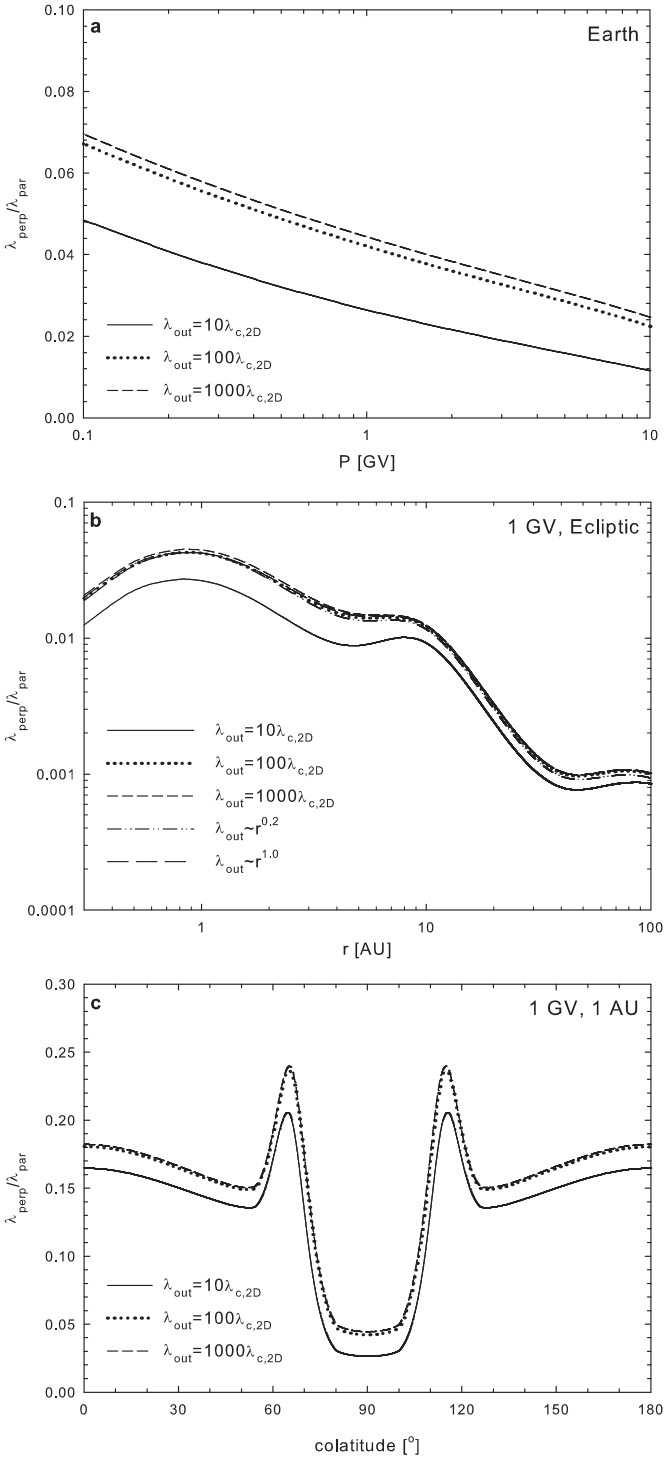

Figure 4.28: The ratios of proton ENLGC perpendicular to proton QLT parallel mean free paths presented in the previous subsections, for various forms chosen for the 2D outerscale. Top panel shows $\lambda_\perp/\lambda_\parallel$ as function of rigidity at Earth, middle panel as function of heliocentric radial distance in the ecliptic, and the bottom panel as function of colatitude at 1 AU.

free paths here shown display a rigidity-dependent decrease. This is due to the *Breech et al.* [2008] turbulence transport model employed by *Pei et al.* [2010a], where the turbulence generated by pickup-ion formation enters the 2D component, leading to 2D variances that do not

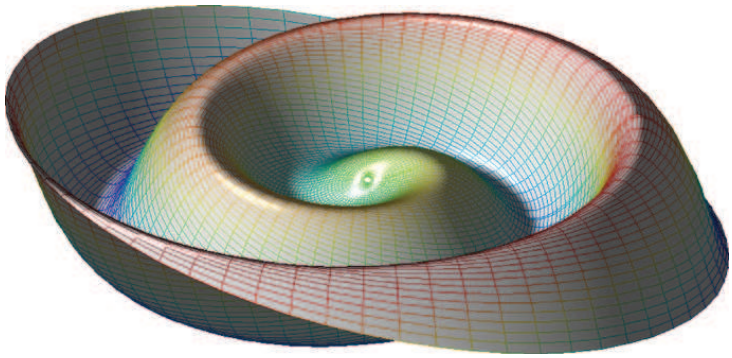

Figure 4.29: The heliospheric current sheet defined following *Kóta and Jokipii* [1983] in Eq. 4.48 within 10 AU [*Pei et al.*, 2012].

decrease as steeply with radial distance as do those yielded by the *Oughton et al.* [2011] model, which only assigns the energy due to pickup-ion formation to the slab component. When perpendicular mean free paths resulting from forms chosen for the outerscale with different radial dependences are considered, as shown in the bottom panel of Fig. 4.27, it is clear that the radial dependence of λ_{out} has very little effect on the radial dependence of $\lambda_{\perp}$. The 0.01 GV electron perpendicular mean free paths (not shown) behave similarly as functions of radial distance to the 0.1 GV proton perpendicular mean free paths but are larger in magnitude, with larger mean free paths corresponding as before to larger values of λ_{out}.

4.7.1 Ratio of the perpendicular to parallel mean free path

Panel (a) of Fig. 4.28 shows the ratio $\lambda_{\perp}/\lambda_{\parallel}$ as function of rigidity at Earth, for various forms of outerscale. Note that the results corresponding to $\lambda_{out} \sim r^{\varrho}$ are not shown, as they are at Earth equal to those for $\lambda_{out} = 100\lambda_{c,2D}$. For all rigidities shown and outerscales used, this ratio remains between 0.01 and 0.07. This range is in agreement with the observations of *Palmer* [1982], even though the individual mean free paths presented here remain well above the consensus values reported in that study. The range of values for $\lambda_{\perp}/\lambda_{\parallel}$ at Earth is also similar to those used in prior studies [see, e.g. *Jokipii et al.*, 1995; *Burger et al.*, 2000; *Ferreira et al.*, 2001a; *Manuel et al.*, 2011; *Strauss et al.*, 2011; *Della Torre et al.*, 2012], although many studies take this value to be constant throughout the heliosphere. In this study this ratio is shown to be a function of rigidity, as well as of both radial distance and latitude. Panel (b) of Fig. 4.28 shows the radial dependence of this ratio, for 1 GV mean free paths. Beyond ~ 10 AU, $\lambda_{\perp}$ assumes values less than one percent of those assumed by $\lambda_{\parallel}$, a consequence of the larger values assumed by the latter quantity in the outer heliosphere, combined with the decrease in the perpendicular mean free paths discussed in the previous subsection. Use of a smaller outerscale, leading as it does to smaller perpendicular mean free paths, yields lower values for $\lambda_{\perp}/\lambda_{\parallel}$. Changes in the radial dependence for the 2D outerscale has little to no effect on $\lambda_{\perp}/\lambda_{\parallel}$. As a function of colatitude, shown in panel (c) of Fig. 4.28 at 1 AU, the ratio $\lambda_{\perp}/\lambda_{\parallel}$ at 1 GV varies considerably, showing relatively large increases at latitudes corresponding to

large stream-shear effects. Overall, in the polar regions this ratio is considerably larger than in the ecliptic plane. A smaller choice of λ_{out} leads again to a smaller value for $\lambda_\perp/\lambda_\parallel$ at all colatitudes.

4.8 The drift coefficient

Cosmic-rays in the heliosphere experience drifts due to the gradient and curvature of the heliospheric magnetic field, as well as due to their interaction with the wavy heliospheric current sheet, a surface over which the sign of the HMF is reversed. Many studies have shown that these drifts have a significant effect on cosmic-ray modulation [see, *e.g.*, *Jokipii and Levy*, 1977; *Jokipii et al.*, 1977; *Kóta*, 1979; *Isenberg and Jokipii*, 1978; *Jokipii and Kopriva*, 1979; *Jokipii and Thomas*, 1981; *Potgieter and Moraal*, 1985; *Thomas et al.*, 1986; *Zhang*, 1997; *Lockwood and Webber*, 2005; *Webber et al.*, 2005], accounting for the 22-year cycle in cosmic-ray intensities [*Jokipii and Thomas*, 1981]. In the weak scattering limit, with little to no turbulence present, *Jokipii and Parker* [1970] and *Forman et al.* [1974] show that the Parker transport equation contains the drift coefficient

$$\kappa_A^{ws} = \frac{v}{3} R_L, \tag{4.46}$$

with R_L the maximal gyroradius. Drift effects, however, have been shown to be reduced in the presence of turbulence, both theoretically and by means of numerical simulations [see, *e.g.*, *Jokipii*, 1993; *Giacalone et al.*, 1999; *Candia and Roulet*, 2004; *Minnie et al.*, 2007b; *Tautz and Shalchi*, 2012]. Given the importance of drift in any study of cosmic-ray modulation, this reduction needs to be carefully modelled. This endeavour is rendered difficult due to a relative paucity of numerical simulations performed, relative to those done to investigate diffusion parallel and perpendicular to the mean HMF. A self-consistent theoretical approach to the problem of drift reduction due to turbulence appears to be rather complicated, and relatively few attempts to do so have been made [see, *e.g.*, *Bieber and Matthaeus*, 1997; *Stawicki*, 2005; *le Roux and Webb*, 2007; *Weinhorst et al.*, 2008; *Burger and Visser*, 2010; *Tautz and Shalchi*, 2012].

The present section aims to describe how cosmic-ray drifts and their reduction due to turbulence are dealt with in this study. Wavy current sheet drift will first be described, followed by brief discussions on numerical simulations and theoretical models pertinent to drift reduction. The turbulence-reduced drift coefficient employed in this study will be introduced, and the 2D ultrascale, as well as the drift lengthscale analogous to the diffusion mean free paths discussed above, will be introduced and characterized.

4.8.1 Wavy current sheet and drift velocity field

The heliospheric current sheet is a surface across which the heliospheric magnetic field changes its polarity, with a wavy structure as illustrated in Fig. 4.29. This structure has a strong solar cycle dependence, and the increase in the tilt angle α towards solar maximum can lead the

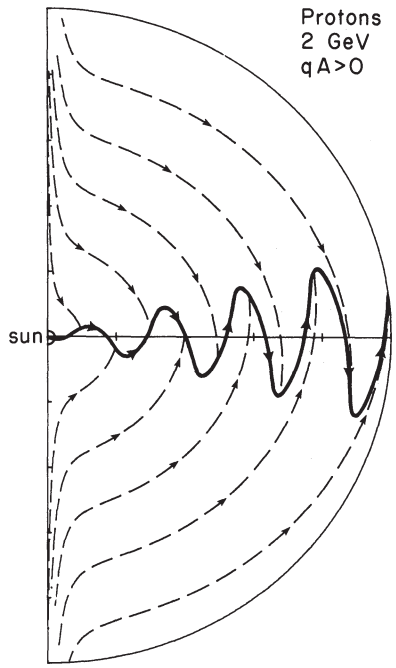

Figure 4.30: Proton drift directions during $qA > 0$, from *Jokipii and Thomas* [1981].

current sheet to behave in an extremely complex manner [*Kóta and Jokipii*, 2001]. Due to the inherent charge-sign dependent nature of drift effects, the direction in which cosmic-rays drift will depend on the solar magnetic polarity cycle. Fig. 4.30 illustrates how high energy protons will drift down from the heliospheric poles, and out along the wavy current sheet when $qA > 0$ (q denoting the charge of the particle considered and A the constant in Eq. 3.25), and in along the current sheet, exiting towards the poles, when $qA < 0$. Electrons, being of opposite charge to protons, will drift in the opposite sense to protons for a given solar magnetic polarity.

Drift of cosmic rays along the wavy current sheet is here implemented following a new drift velocity field proposed by *Burger* [2012]. See also *Burger et al.* [1985], *Burger* [1987], *Burger and Hattingh* [1995] and *Hattingh and Burger* [1995]. This wavy current sheet drift model has been benchmarked against the approach of *Kóta and Jokipii* [1983], and against the model utilized by *Pei et al.* [2012], yielding results for galactic proton intensities during the $A < 0$ solar magnetic polarity epoch in much closer agreement with the results reported by the former authors, as opposed to those of the latter. *Burger* [2012] argues that in some previous approaches for drift along the current sheet, a particle's drift velocity can under certain conditions become greater than its speed. This is an unphysical situation that can lead to instabilities when finite-grid numerical techniques (such as the ADI method employed in the present study) are used to solve the Parker transport equation.

Burger [2012] employs, as a point of departure the expression for the drift velocity of a nearly-isotropic particle distribution

$$\mathbf{v}_d = \nabla \cdot \mathbf{K}^A \equiv \nabla \times (\kappa_A \mathbf{e}_B)\,, \tag{4.47}$$

where $\mathbf{e}_B$ denotes a unit vector in the HMF direction. He considers the geometry of a wavy current sheet surface introduced by *Kóta and Jokipii* [1983]

$$\theta_{ns} = \frac{\pi}{2} - \arctan\left[\tan\alpha \sin\phi^*\right], \tag{4.48}$$

where $\phi^* = \phi + \phi_o + r\Omega/V_{sw}$, with ϕ_o governing the 'phase' of the current sheet, showing that the drift velocity $\mathbf{v}_d$ can be expressed by

$$\mathbf{v}_d = \frac{k_{ns}}{\cosh^2\left[k_{ns}(\theta_{ns} - \theta)\cos\nu\right]}\kappa_A \mathbf{e}_{ns}, \tag{4.49}$$

with $\mathbf{e}_{ns}$ a unit vector in the direction of the current sheet drift:

$$\mathbf{e}_{ns} = \sin\Psi\cos\nu\mathbf{e}_r + \sin\nu\mathbf{e}_\theta + \cos\Psi\cos\nu\mathbf{e}_\phi, \tag{4.50}$$

where Ψ denotes the winding angle of the HMF. The quantity ν denotes the angle between a vector locally normal to the current sheet, and the $-\mathbf{e}_\theta$ direction, while the parameter k_{ns} governs the modelled angular width of the current sheet. In the present study, this latter parameter is set so that

$$k_{ns} \quad = \quad \begin{cases} 20.12 & \text{for } P \leq 3.5 \text{ GV}; \\ 27.52P^{-0.25} & \text{for } P > 3.5 \text{ GV}, \end{cases} \tag{4.51}$$

following the approach of *Burger* [2012] and ensuring that the drift profile of the current sheet covers a sufficient number of grid points in the ADI numerical solver here employed.

4.8.2 Numerical simulations of the drift coefficient

Compared to the large number of numerical test particle simulations performed so as to investigate particle diffusion (see Subsection 4.2.2), the drift coefficients have received relatively little attention. *Giacalone et al.* [1999] simulate the drift coefficient in the presence of homogeneous, isotropic turbulence, assuming a spectrum consisting solely of a Kolmogorov inertial range with a correlation length of 0.01 AU and a uniform background magnetic field, following the procedure outlined by *Giacalone and Jokipii* [1999]. They find that their simulated drift coefficient is in good agreement with the weak scattering value when their simulated mean free paths were larger than the test particle gyroradii, i.e. for relatively low levels of turbulence. At higher levels of turbulence, *Giacalone et al.* [1999] find that their simulated drift coefficient assumes values lower than those yielded by the weak scattering drift coefficient. Simulations under similar isotropic turbulence conditions, and for similarly defined fluctuation power spectra, were performed by *Candia and Roulet* [2004], albeit for several different inertial range wavenumber dependences. These authors report results similar to those of *Giacalone et al.* [1999], in that increased levels of turbulence lead to reduced simulated drift coefficients.

Minnie et al. [2007b] performed simulations of the drift coefficient assuming homogeneous, composite turbulence set up so as to agree with observations presented by *Bieber et al.* [1996]. They utilize fluctuation spectra with flat energy ranges and Kolmogorov inertial ranges for

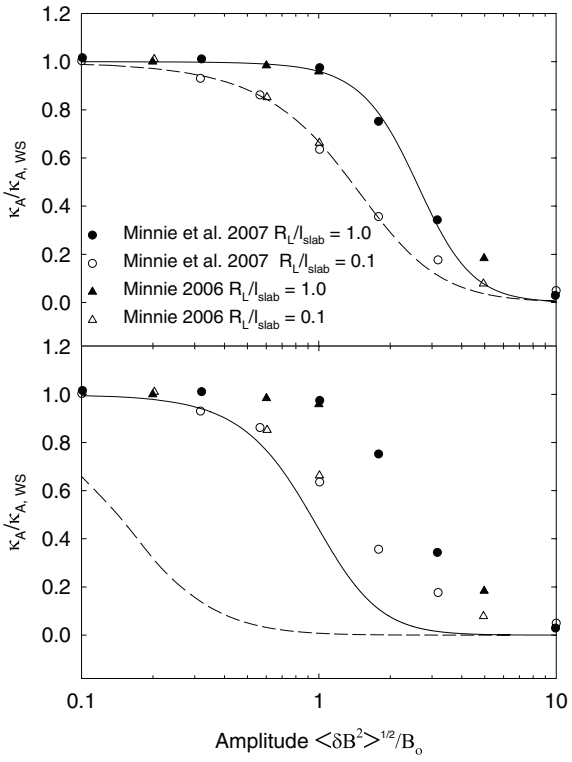

Figure 4.31: Drift coefficients simulated by *Minnie et al.* [2007b], normalised to the weak scattering coefficient, as functions of total turbulent fluctuation amplitude, from *Burger and Visser* [2010]. Lines in the top panel illustrate a parametrised drift coefficient presented by *Burger and Visser* [2010], while those in the bottom panel illustrate the drift coefficients of *Bieber and Matthaeus* [1997]. Triangular symbols are for a uniform background field and circles are for a field with a gradient, constructed to yield a uniform drift velocity field.

the slab and 2D components, taking the 2D turnover scale to be equal to one tenth the slab turnover scale. Simulations followed the general scheme presented by *Minnie et al.* [2007a], and drift coefficients were calculated following the approach of *Giacalone et al.* [1999]. The results presented by *Minnie et al.* [2007b] for their simulated drift coefficient, normalised to the equivalent weak scattering value, are illustrated in Fig. 4.31 as functions of total magnetic fluctuation amplitude for two values of maximal particle gyroradius. This is equivalent to considering the drift coefficient at a high and a low rigidity. From Fig. 4.31 it is clear that drift coefficients are suppressed by turbulence, and that this suppression is an energy-dependent phenomenon, with generally higher levels of reduction occurring at lower rigidities for a given level of turbulence. Note that the triangular symbols are for a uniform background magnetic field while the circles are for a field with a gradient, constructed to yield a uniform drift velocity field. *Minnie et al.* [2007b] also report on simulated drift speeds, shown in Fig. 4.32 in a format similar to that of Fig. 4.31. They find that higher turbulence levels also lead to a reduction in this quantity, so much so that at a sufficient level, the drift velocity may be reversed.

A study of the effects of various turbulence models on drift coefficients was performed by *Tautz and Shalchi* [2012], who consider both isotropic and composite turbulence, as well as the effects of the wavenumber dependence of the energy range of the turbulence power spectrum.

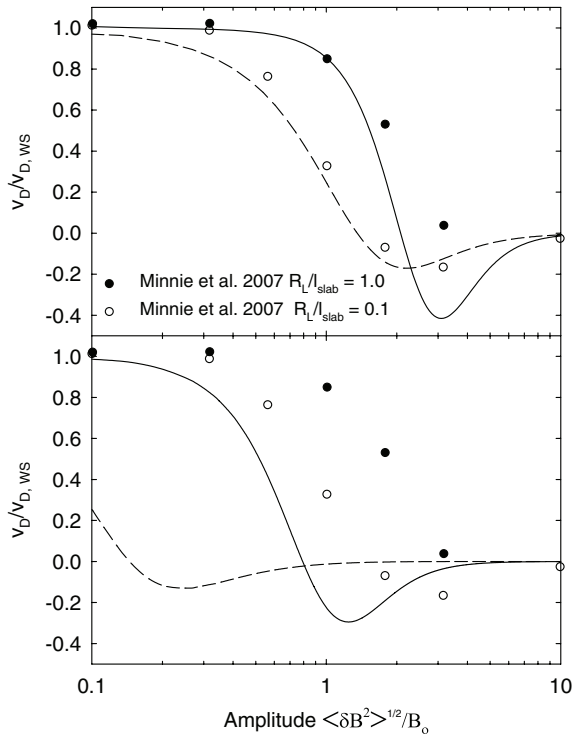

Figure 4.32: Drift speeds simulated by *Minnie et al.* [2007b], normalised to the weak scattering values, as functions of total turbulent fluctuation amplitude, from *Burger and Visser* [2010]. Lines in the top panel illustrate the drift speeds resulting from the use of the parametrized drift coefficient presented by *Burger and Visser* [2010], while those in the bottom panel illustrate the drift speeds acquired from the drift coefficients of *Bieber and Matthaeus* [1997].

They find, in agreement with the prior simulations reported by the authors cited above, that drift effects are suppressed in the presence of increasing levels of turbulence. Furthermore, the simulations of *Tautz and Shalchi* [2012] show only a very weak effect of the choice of energy range wavenumber dependence on drift suppression.

The specific results of the simulations discussed above are sensitive to the assumptions made as to both the structure of the turbulence employed, as well as the values turbulence quantities such as correlation scales are assumed to take, with all the above studies attempting to simulate turbulence conditions as observed at 1 AU. These conditions do not necessarily reflect those in other parts of the heliosphere, as indicated by the various observations discussed in Section 2.3. Therefore a certain degree of caution needs be exercised in the extrapolation of these results to other regions of the heliosphere.

4.8.3 Reduced drift coefficients

In the present study, a parametrized drift coefficient proposed by *Burger and Visser* [2010] that approaches the weak scattering coefficient in the absence of turbulence, is utilized. Although a fairly large amount of work has been done in the calculation of such a coefficient in the presence of turbulence [see, *e.g.*, *Bieber and Matthaeus*, 1997; *Stawicki*, 2005; *le Roux and Webb*, 2007;

Weinhorst et al., 2008; *Dosch et al.*, 2009; *Tautz and Shalchi*, 2012], the choice of the *Burger and Visser* [2010] drift coefficient was made due to its ability to reproduce the results of the simulations reported by *Minnie et al.* [2007b] pertaining to both the drift coefficients and velocity to a fair degree, and due to its tractability and ease of application within the framework of a cosmic-ray modulation model such as that employed here. *Burger and Visser* [2010] also demonstrate that the use of their parametrized drift coefficient can yield good agreement with observed galactic cosmic-ray intensities, at least at 1 AU, and for *ad hoc* choices of the 2D ultrascale. Other such parametrized drift coefficients, such as those proposed by *Candia and Roulet* [2004], do not agree as well with the aforementioned simulations, possibly due to the different turbulent conditions assumed for the *Minnie et al.* [2007b] simulations, as opposed to those employed in the acquisition of the *Candia and Roulet* [2004] results.

Burger and Visser [2010] use, as a point of departure, the results of *Bieber and Matthaeus* [1997] who find that

$$\kappa_A = \frac{v}{3} R_L \frac{\Omega^2 \tau^2}{1 + \Omega^2 \tau^2}, \tag{4.52}$$

with τ the rate at which helical particle trajectories become less helical due to unspecified interactions, and Ω the angular gyrofrequency. Furthermore, *Bieber and Matthaeus* [1997] find that

$$\Omega\tau = \frac{2}{3}\frac{R_L}{D_\perp}, \tag{4.53}$$

where $D_\perp$ is the perpendicular field line random walk diffusion coefficient [see, *e.g.*, *Matthaeus et al.*, 1995]

$$D_\perp = \frac{1}{2}\left(D_{sl} + \sqrt{D_{sl}^2 + 4D_{2D}^2}\right). \tag{4.54}$$

The subscripts on the coefficients D denote field line diffusion coefficients due to either slab or 2D fluctuations, and can be expressed by [*Matthaeus et al.*, 2007]

$$D_{sl} = \frac{1}{2}\frac{\delta B_s^2}{B_o^2}\lambda_{c,s}, \tag{4.55}$$

and

$$D_{2D} = \frac{\sqrt{\delta B_{2D}^2/2}}{B_o}\lambda_{u,2D}, \tag{4.56}$$

with $\lambda_{c,s}$ the slab correlation scale, δB_s^2 the slab variance, δB_{2D}^2 the 2D variance, and $\lambda_{u,2D}$ the 2D ultrascale (see Subsections 2.2.1 and 2.4.1 for more detail on to this quantity). The bottom panels of Figures 4.31 and 4.32 illustrate the theoretical predictions of the *Bieber and Matthaeus* [1997] approach alongside the simulation results of *Minnie et al.* [2007b], and clearly, the agreement is not good. This being the case, *Burger and Visser* [2010] propose a parametrized form for $\Omega\tau$,

$$\Omega\tau = \frac{11}{3}\frac{\sqrt{R_L/\lambda_{c,s}}}{(D_\perp/\lambda_{c,s})^g}, \tag{4.57}$$

with

$$g = 0.3 \log\left[\frac{R_L}{\lambda_{c,s}}\right] + 1.0. \tag{4.58}$$

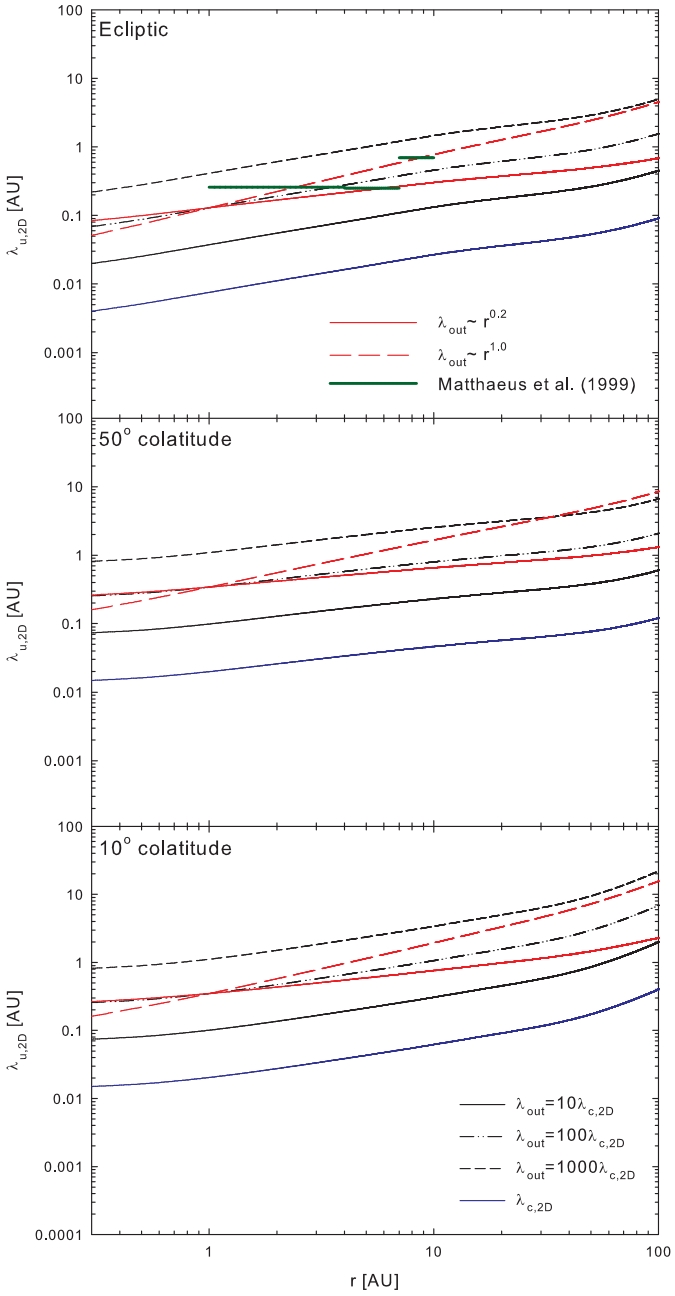

Figure 4.33: The 2D ultrascale, as function of heliocentric radial distance at several colatitudes, for various forms assumed for the 2D outerscale. Note that the ultrascales presented here are calculated using outputs yielded by the two-component turbulence transport model of *Oughton et al.* [2011]. Observations shown are from *Matthaeus et al.* [1999b].

The results yielded by this approach are in good agreement with the simulations for the drift coefficients performed by *Minnie et al.* [2007b], and with the drift velocities at relatively low levels of turbulence, as shown in the top panels of Figures 4.31 and 4.32.

4.8.4 The 2D ultrascale

In the present study, the 2D ultrascale is that for an omnidirectional energy spectrum with a flat energy range introduced in Subsection 2.4.1, repeated here for ease of reference as

$$\lambda_{u,2D} = \sqrt{C_0 \lambda_{2D} \left(\left(\frac{1}{q-1} + 1 \right) \lambda_{out} + \left(\frac{1}{1+\nu} - 1 \right) \lambda_{2D} \right)}. \tag{4.59}$$

This subsection aims to characterize this expression throughout the heliosphere, utilizing as inputs results from the two-component transport model of *Oughton et al.* [2011] discussed in the previous chapter. Here, simple expressions for the 2D outerscale outlined in Section 4.7 and illustrated in Fig. 4.23 will be employed so as to describe the effect of this quantity on the ultrascale. As in the rest of this study, a Kolmogorov value is assumed for the inertial range spectral index ν, while a value of 3 is assumed for the spectral index q of the inner range of the 2D omnidirectional fluctuation spectrum, following *Matthaeus et al.* [2007].

The top panel of Fig. 4.33 shows the radial profiles of the various 2D ultrascales calculated from Eq. 4.59 for the 2D outerscale expressions considered. Given the dependence of the ultrascale on λ_{out}, it comes as no surprise that the radial dependence chosen for this quantity would act so as to dominate the radial dependence of $\lambda_{u,2D}$, with ultrascales resulting from a choice of $\lambda_{out} \propto \lambda_{c,2D}$ obviously scaling the same as $\lambda_{c,2D}$ with radial distance, while ultrascales calculated with $r^{0.2}$ and $r^{1.0}$ dependences for the outerscales showing considerably different radial dependences. The latter two ultrascales, along with that corresponding to a choice of $\lambda_{out} = 100\lambda_{c,2D}$, are compatible with the range suggested by *Matthaeus et al.* [1999b]. This, however, may not be a conclusive criterion to justify the choice of a particular form or value for the 2D outerscale, as correlation lengthscales calculated using single spacecraft data have been reported to be larger than those acquired using analyses based on observations taken by multiple spacecraft [*Matthaeus et al.*, 2005]. The magnitudes assumed by ultrascales at lower colatitudes, shown in the bottom panels of Fig. 4.33, are larger than in the ecliptic due to the increased outerscale values at these colatitudes, with the largest values to be found closest to the poles.

The choice of 2D outerscale, then, has a strong influence, not only on the perpendicular mean free paths throughout the heliosphere, but also on the 2D ultrascales, implying, in turn, a strong effect on the drift coefficient discussed in the previous subsection.

4.8.5 Reduced drift scale

The aim of this subsection is to characterize the turbulence-reduced *Burger and Visser* [2010] drift coefficient discussed in Subsection 4.8.3 in terms of a drift lengthscale λ_A, that can be acquired from the drift coefficient using the relation $\kappa_A = v\lambda_A/3$. These results will be compared to those of the weak scattering drift lengthscale, which is the gyroradius R_L, as well as those

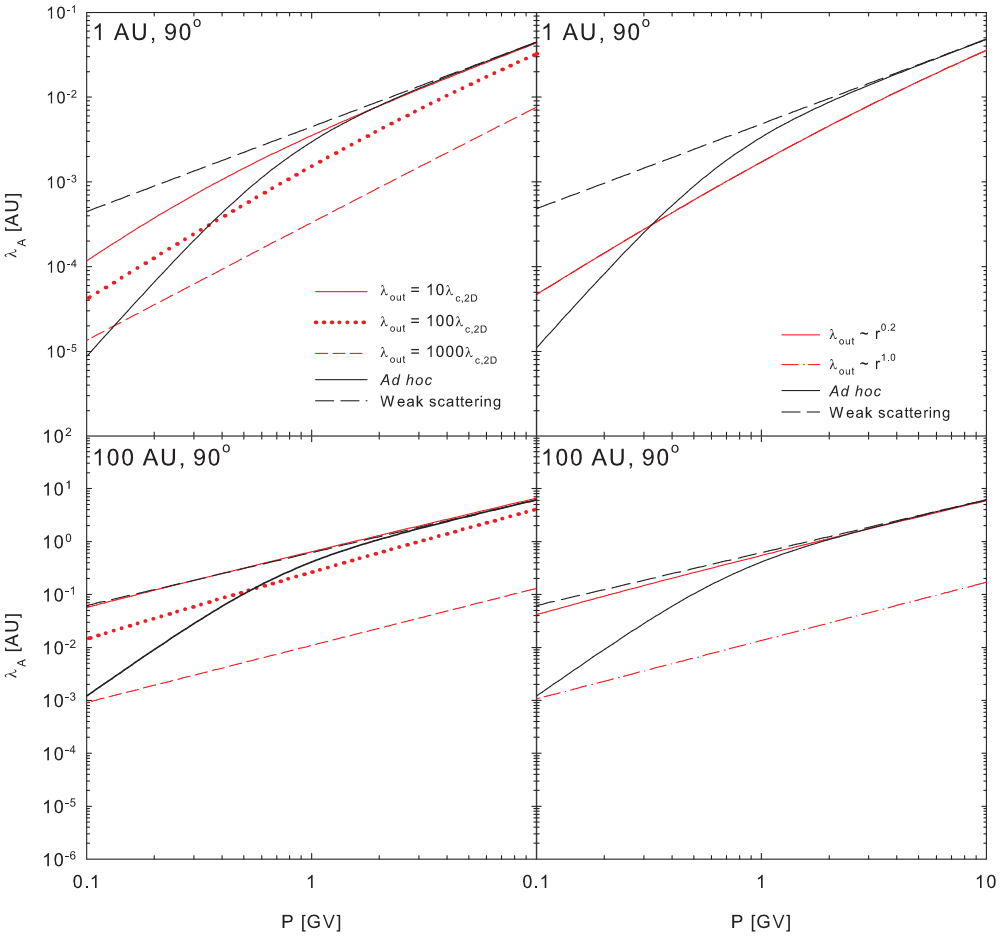

Figure 4.34: Drift scales acquired from the drift coefficients presented by *Burger and Visser* [2010] in the ecliptic plane for the various forms for the 2D outerscale assumed here as functions of rigidity at 1 AU and 100 AU, using as inputs the results of the *Oughton et al.* [2011] turbulence transport model.

of an *ad hoc* reduced drift coefficient employed by previous modulation studies, and given by [*Burger and Hitge*, 2004; *Burger et al.*, 2008]

$$\kappa_A = \frac{\beta P}{3B_o} \frac{(P/P_0)^2}{1+(P/P_0)^2}, \tag{4.60}$$

where $P_0 = 1/\sqrt{2}$ GV. This is to allow for comparisons to be made as to approaches taken in previous modulation studies with those of the present study. The effects of the various forms assumed for the 2D outerscale in Section 4.7 will be discussed, using outputs from the *Oughton et al.* [2011] turbulence transport model.

Figure 4.34 illustrates the rigidity dependences of the various drift lengthscales at 1 AU and 100 AU in the solar ecliptic plane. At 1 AU, as λ_{out} is increased, the drift scales are consistently smaller than the weak scattering limit. Moreover, a faster decrease at low rigidities becomes less prominent for larger values of λ_{out}, while the slopes at high rigidities are steeper than that of the weak-scattering case. For smaller values of the 2D outerscale (and hence smaller values of the 2D ultrascale) the drift scales approach the weak scattering values. The *ad hoc*

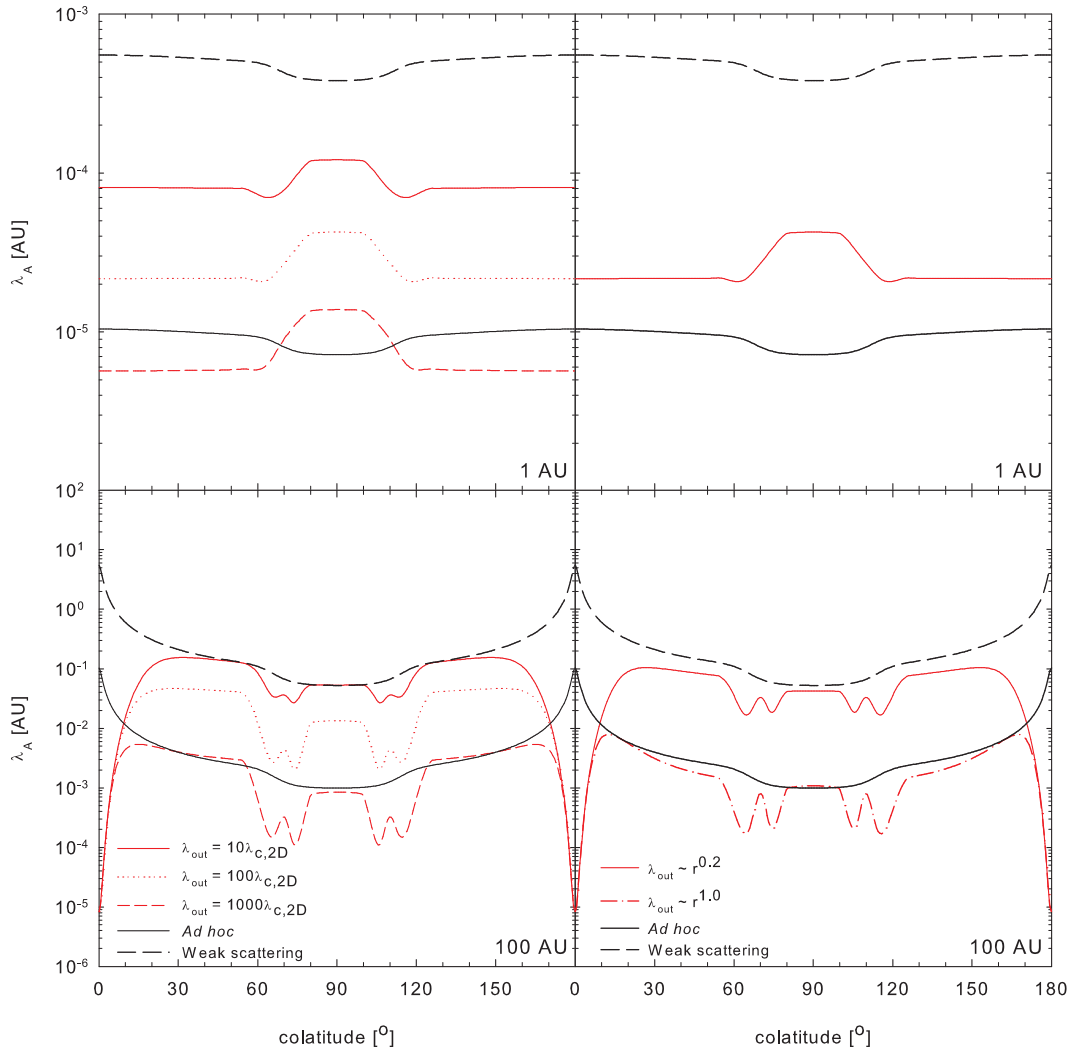

Figure 4.35: Drift scales acquired from the drift coefficients presented by *Burger and Visser* [2010] and taken at 0.1 GV for the various forms for the 2D outerscale as functions of colatitude at 1 AU and 100 AU, using as inputs the results of the *Oughton et al.* [2011] turbulence transport model.

drift scale agrees best with results for the smallest outerscale considered, at high rigidity, but differs from it by an order of magnitude at the lowest rigidity considered. For the cases where $\lambda_{out} \sim r^{\varrho}$, the drift scales at 1 AU are the same, due to these scalings for λ_{out} being normalised to the same value at 1 AU, regardless of colatitude. Note that these results agree very well with those obtained when $\lambda_{out} = 100\lambda_{c,2D}$. This in agreement with the behaviour found for the perpendicular mean free paths (see Section 4.7). All of the 2D outerscale forms show at 100 AU a rigidity dependence very similar to that of the maximal gyroradius, and hence of the weak scattering drift scale, with smaller values of λ_{out} yielding drift scales essentially equal to the weak scattering result. In the outer heliosphere there is clearly little resemblance between these results and the *ad hoc* drift scale. The case of $\lambda_{out} = 1000\lambda_{c,2D}$, yielding the largest values for the 2D outerscale and ultrascale, again produces the smallest drift scale of the five λ_{out} dependences here considered.

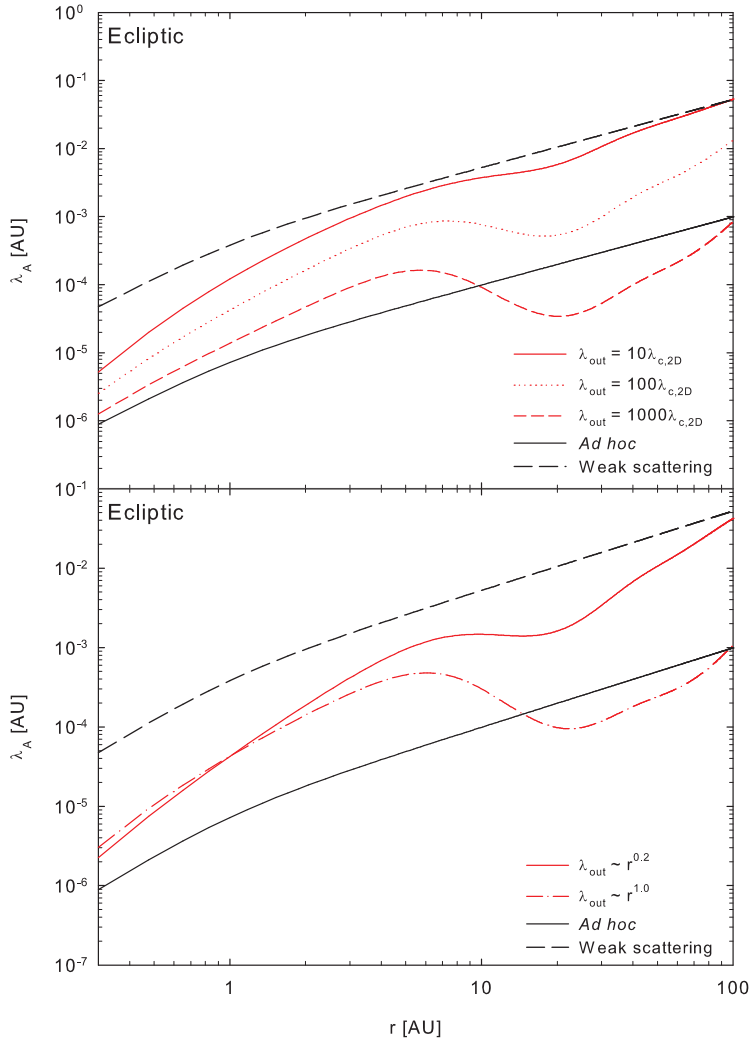

Figure 4.36: Drift scales acquired from the drift coefficients presented by *Burger and Visser* [2010] and taken at 0.1 GV for the various forms for the 2D outerscale as functions of radial distance in the ecliptic plane, using as inputs the results of the *Oughton et al.* [2011] turbulence transport model.

As functions of colatitude, shown at 1 AU and 100 AU in Fig. 4.35, the 0.1 GV drift scales again follow the rule that the smallest drift scales correspond to the largest assumed values for the 2D outerscale, and hence for the 2D ultrascale. Drift scales are also noticeably reduced at latitudes corresponding to regions of enhanced stream-shear effects where turbulence levels are larger. Solutions corresponding to larger values of λ_{out} appear to be more sensitive to these effects than those for smaller values for this quantity. It is of interest to note that at 1 AU, the weak scattering and *ad hoc* drift scales tend to be smaller in the ecliptic than over the poles, following as they do the colatitudinal dependence of the proton gyrofrequency, while for the *Burger and Visser* [2010] drift scales the opposite is true, due to their dependence on the outputs of the *Oughton et al.* [2011] model. The picture becomes considerably more complicated at 100 AU, especially in the polar regions. Both the weak scattering and *ad hoc* drift scales appear to increase towards the poles, again due to their dependence on the proton gyroradius. This is not

the case for the *Burger and Visser* [2010] drift scales, which decrease to very low values, regardless of what assumptions are made as to the 2D outerscale over the solar poles. This behaviour is due to the increased levels of turbulence over the solar poles at large radial distances, as yielded by the *Oughton et al.* [2011] model, and thus represents a significant departure from the assumptions made in previous studies as to the behaviour of the drift coefficient in the heliospheric polar regions.

Fig. 4.36 illustrates the radial dependences of the various 0.1 GV drift scales discussed thus far. Both the *ad hoc* and weak scattering drift scales follow the radial dependence of the proton gyroradius. The *Burger and Visser* [2010] drift scale, for $\lambda_{out} = 10\lambda_{c,2D}$ follows the weak scattering model most closely past ~ 10 AU. Larger values for the 2D outerscale lead to drift scales that no longer increase monotonically as function of radial distance. The radial dependences of the *Burger and Visser* [2010] drift scales becomes less like that of the ultrascales for larger outerscales, appearing to follow more the behaviour of the slab correlation scale. For the cases where $\lambda_{out} \sim r^{\varrho}$ (bottom panel), the radial dependences again differ significantly from that of the weak-scattering result, but are qualitatively similar to those for the outer scale considered in the top panel.

4.9 Summary and conclusion

This chapter commenced with a brief introduction to the general diffusion tensor as found in the *Parker* [1965a] cosmic-ray transport equation. A short overview of spacecraft observations and numerical simulations of the parallel and perpendicular mean free paths was given. On the basis of these results, choices of scattering theories were made and motivated. Parallel mean free path expressions were then introduced, constructed from the piecewise analytical results derived from QLT by *Teufel and Schlickeiser* [2003] for the random sweeping and damping models of dynamical turbulence for both protons/antiprotons and electrons/positrons. These were then characterized as functions of spatial coordinates and particle rigidity throughout the heliosphere, with the required slab turbulence quantities obtained from the two-component *Oughton et al.* [2011] turbulence transport model discussed in the previous chapter. Furthermore, special emphasis was placed upon the characterization of the low-energy electron parallel mean free paths as functions of quantities applicable only to the dissipation range of the slab turbulence power spectrum. Use of a turbulence transport model leads to considerably more complicated spatial and rigidity dependences of the parallel mean free paths introduced in this work, when compared to what has previously been used in cosmic-ray modulation studies [see, *e.g.*, *Müller-Mellin and Wibberenz*, 1995; *Potgieter*, 1996; *Le Roux et al.*, 1999; *Ferreira*, 2002; *Burger et al.*, 2008; *Engelbrecht and Burger*, 2010].

Perpendicular mean free paths derived from the ENLGC theory of *Shalchi* [2006] were also introduced, and characterized in a similar vein to that of the parallel mean free paths. The assumed form of the 2D modal spectrum used in their derivation, however, is set to decrease

at the smallest wavenumbers so as to ensure a non-divergent expression for the 2D ultrascale, and hence requires as input a so-called 2D outerscale at which this decrease commences. Unfortunately, no observations currently exist for this quantity, and thus various simple *ad hoc* expressions for it were employed so as to elucidate its effects on the derived perpendicular mean free paths. Once more, the use of the *Oughton et al.* [2011] turbulence transport model leads to complicated spatial dependences for this quantity.

Furthermore, after a brief consideration of numerical simulation results and discussion on the means whereby wavy current sheet drift is treated in the present study, drift coefficients proposed by *Burger and Visser* [2010] that are reduced in the presence of turbulence, and yield results in line with the aforementioned numerical simulations, were chosen. These are functions of the 2D ultrascale, and therefore also depend upon the 2D outerscale. The ultrascale and drift coefficients were characterized, in line with the results for the parallel and perpendicular mean free paths, as functions of rigidity and spatial coordinates for the previously considered *ad hoc* forms assumed for the 2D outerscale. The 2D outerscale was found to have a significant effect on the drift lengthscales, when compared to the weak scattering limit and previously employed *ad hoc* reduced drift coefficients. The use of the *Oughton et al.* [2011] turbulence transport model once more led to considerably more complicated spatial dependences for the drift coefficients than those displayed by the weak scattering model, with the most notable differences to be found in the heliospheric polar regions.

The following chapter will apply the *ab initio* diffusion tensor presented here to the study of the modulation of various species of cosmic-rays throughout the heliosphere.